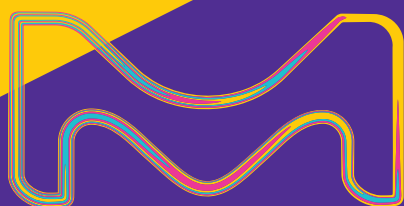


Material Matters™

VOLUME 14 • NUMBER 1



Nanomaterials For Emerging Bioelectronics

Nanotechnology at the Bio-Electronic Interface

ORGANIC BIOELECTRONIC MATERIALS and DEVICES for Bridging Biology and Traditional Electronics

2D Materials Matter: A Perspective on BIOSENSING APPLICATIONS

ORGANIC AND HYBRID ELECTRONICS IN OPTICAL ANALYTICAL APPLICATIONS

Properties and Applications of FUNCTIONALIZED GRAPHENE OXIDE

The life science business of Merck operates as MilliporeSigma in the U.S. and Canada.



Introduction



Na Li, Ph.D.
Product Manager -
Electronic Materials

Welcome to the first issue of *Material Matters*™ for 2019, focused on research advancements in emerging nano-bioelectronics. This issue highlights innovative materials as well as device configurations that address the topics of sensitivity, specificity, or biocompatibility of bioelectronics for the monitoring, stimulating, and controlling of various biological systems.

Biological systems employ complex molecular and cellular mechanisms to propagate signals through ionic charges. Traditional microelectronics rely on metals, inorganic semiconductors, and oxide dielectrics to propagate signals through electronic charges, leading to a fundamental mismatch in signal transmission. In our first article, Professor Rivnay (Northwestern University, USA) discusses using organic mixed conductors as an alternative to efficiently bridge the ionic world of biology with contemporary microelectronics, allowing for a decrease in the mechanical mismatch between electronic devices and the surrounding biological material. Moreover, the authors introduce new strategies through side chain engineering of conjugated polymers to improve the performance of organic mixed conductors for next generation bioelectronics.

Novel 2D materials, such as transition metal dichalcogenides, have drawn increasing interest for use in bioelectronics and healthcare applications due to their enhanced sensitivity, atomically thin nature, and advanced functionalization capabilities. In our second article, Professor Ebrahimi and Professor Robinson (Pennsylvania State University, USA) summarize recent advances in the synthesis of these 2D materials, resulting material properties, and related applications in biosensing of neurotransmitters, metabolites, proteins, nucleic acids, bacterial cells, and heavy metals.

Sensors based on organic semiconductor materials and all-organic components such as light emitting diodes, solar cells, and photodetectors are easily miniaturized and can eliminate issues related to portability and deployability, simplify fabrication, and reduce cost. In our third article, Professor Shinar (Iowa State University, USA) summarizes the developments of a variety of sensor configurations based on organic and hybrid electronics, as low-cost, disposable, non-invasive, wearable bioelectronics for healthcare.

Ever since graphene was first isolated, its combination of biocompatibility with extraordinary electrical, mechanical, and electrochemical properties has drawn significant interest for use in biomedical applications. In the final article, Professor Aran (Claremont University, USA) discusses the engineering of graphene based materials through careful functionalization of graphene oxide, a solution processable form of graphene, to increase its sensitivity, specificity, and stability as implantable and wearable electrochemical sensors in biomedical applications.

Each article in this publication is accompanied by a list of relevant materials available from Aldrich Materials Science. For additional product information, visit us at **SigmaAldrich.com/matsci** Please bother us with your new product suggestions, as well as thoughts and comments for *Material Matters*™ at **SigmaAldrich.com/technicalservice**

About the Cover

Nano-bioelectronics represents an emerging multidisciplinary field that combines nanomaterials with biology and electronics. Innovations in material design and device configurations have significantly improved the sensitivity and biocompatibility of bioelectronics, and thereby opened up new opportunities to overcome existing challenges in fundamental biology and healthcare. The cover art illustrates how the combination of nanomaterials, and electronics with biology has the potential to expand human perceptions beyond our five senses.

Merck KGaA
Frankfurter Strasse 250
64293 Darmstadt, Germany
Phone +49 6151 72 0

To Place Orders / Customer Service

Contact your local office or visit
SigmaAldrich.com/order

Technical Service

Contact your local office or visit
SigmaAldrich.com/techinfo

General Correspondence

Materials Science
materialsscience@sial.com

Subscriptions

Request your FREE subscription to *Material Matters*™ at **SigmaAldrich.com/mm**

The entire *Material Matters*™ archive is available at **SigmaAldrich.com/mm**

Material Matters™(ISSN 1933-9631) is a publication of Merck KGaA.

Copyright (c) 2019 Merck KGaA, Darmstadt, Germany and/or its affiliates. All rights reserved. Merck, the vibrant M, Sigma-Aldrich and Material Matters are trademarks of Merck KGaA, Darmstadt, Germany or its affiliates. All other trademarks are the property of their respective owners. Detailed information on trademarks is available via publicly accessible resources. More information on our branded products and services on **MerckMillipore.com**

Table of Contents

Articles

Organic Bioelectronic Materials and Devices for Bridging Biology and Traditional Electronics	3
2D Materials Matter: A Perspective on Biosensing Applications	11
Organic and Hybrid Electronics in Optical Analytical Applications	19
Properties and Applications of Functionalized Graphene Oxide	37

Featured Products

Poly(3,4-ethylenedioxythiophene)-poly(styrenesulfonate) (PEDOT:PSS) A selection of ready-to-use ink PEDOT:PSS and PEDOT:PSS materials	8
Mixed Conductors A selection of conjugated polymer, co-polymer, and high surface area mixed conductors	8
High Surface Area Conductors A selection of high surface area conductors	9
Polymers A selection of ionic and conjugated polymers for bioelectronics	9
2D Materials for Biosensing Selections of transition metal dichalcogenides, boron nitride, graphene, metal electrode deposition precursors, and metal nanoparticles	16
Electron Transport and Hole Blocking Materials, Hole Transport Materials, Host Materials, and Light Emitters and Dopants A selection of materials for optical electronics	28
Dyes A list of copper(II) phthalocyanine dyes	31
Donor Materials and Acceptor Materials A selection of donor materials, non-fullerene and other acceptor materials for optical electronics	31
High Purity Electronic Grade Electrolytes, Perovskite Precursor Solutions, and Intermediates A selection of electronic grade electrolytes, perovskite precursors, and intermediates	35
Graphene Oxide Materials A selection of GO, functionalized GO, reduced GO, and functionalized reduced GO for optical electronics	44



Bryce P. Nelson

Bryce P. Nelson, Ph.D.
Materials Science Initiative Lead

We welcome fresh product ideas. Do you have a material or compound you wish to see featured in our Materials Science line? If it is needed to accelerate your research, it matters. Send your suggestion to matsci@sial.com for consideration.

Dr. Gregory C. Wech of CRC – Solar Energy Materials and Devices (University of Calgary, Canada) recommended the addition of three dimeric perylene diimides (PDIs): N-annulated PDI building block (**901144**), directly linked PDI dimer (**901146**), and a dye linked PDI dimer (**901143**) for use as non-fullerene acceptors (NFAs) in organic solar cells (OSCs).

PDIs have been identified as one of the top classes of NFAs used in high performance OSCs. PDI chromophores linked via conjugated bridges have been used to fabricate polymer based OSCs with a power conversion efficiency (PCE) of 9.5%.¹ Directly linked PDI dimers at the bay or headland position have enabled the fabrication of OSCs with 6% and 8% PCE, respectively.²⁻⁵ N-annulation at the bay position of the PDI unit destabilizes the lowest unoccupied molecule orbital energy level, leading to a lower electron affinity, and consequently high open-circuit voltages in OSCs comparing to those made using non-annulated (or S/Se) PDIs. N-annulation also increases material's solubility and processability due to an added alkyl side chain. Dimerization of the PDI units prevents strong intermolecular interactions and reduces the tendency to over crystallize.

PDI based active layers could be processed via slot-die coating from eco-friendly "green" solvents, making them attractive for active layer engineering to improve OSC performance.⁶⁻⁸

References

- (1) *Nature Energy* **2016**, 1, 15027
- (2) *Adv. Mater.* **2014**, 26, 5708–5714.
- (3) *Chem. Commun.* **2013**, 50, 1024–1026.
- (4) *J. Mater. Chem. A* **2017**, 5, 22288–22296.
- (5) *J. Mater. Chem. C* **2017**, 5, 8875–8882.
- (6) *Chem. Commun.* **2017**, 53, 1164–1167
- (7) *Sustainable Energy Fuels*, **2017**, 1, 1137–1147
- (8) *Small Methods*, **2018**, 2, 1800081

Name	Cat. No.
Hexyl N-annulated perylene diimide	901144-500MG
TPDI-Hex	901146-250MG
PDI-DPP-PDI	901143-100MG

BRIGHT+ CD-FREE

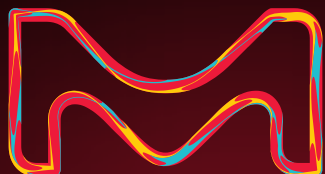
Quantum dots exhibit excellent photoluminescence and electroluminescence properties such as narrow emission bandwidth and high brightness.

Choose cadmium-free quantum dots for applications where toxicity is a concern.

Cd-free Quantum Dots find applications in:

- LEDs
- Displays
- Solid-state lighting
- Photovoltaics
- Transistors

To find out more, visit
SigmaAldrich.com/cd-freeqd

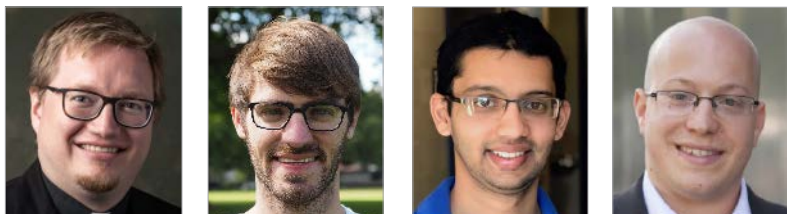


© 2018 Merck KGaA, Darmstadt, Germany and/or its affiliates. All Rights Reserved. MilliporeSigma and the Vibrant M are trademarks of Merck KGaA, Darmstadt, Germany or its affiliates.

2018 - 12263 05/2018

The life science
business of Merck
operates as
MilliporeSigma in
the U.S. and Canada.

Organic Bioelectronic Materials and Devices for Bridging Biology and Traditional Electronics



Bryan D. Paulsen,^{1,2} Alexander Giovannitti,^{3,4} Vishak Venkatraman,^{1,2} Jonathan Rivnay^{1,2*}

¹Department of Biomedical Engineering, Northwestern University, Evanston, IL 60208, USA

²Simpson Querrey Institute for BioNanotechnology, Northwestern University, Chicago, IL 60611 USA

³Department of Chemistry, Imperial College London, London SW7 2AZ, UK

⁴Department of Physics and Center for Plastic Electronics, Imperial College London, London SW7 2AZ, UK

*E-mail: jrivnay@northwestern.edu

Introduction

Bioelectronics, the convergence of biology and electronics, seeks to leverage microelectronics to sense, stimulate, and control biological systems. Biological systems employ complex molecular and cellular mechanisms to propagate signals through the motion and accumulation of ionic charges (anions and cations). Traditional microelectronics rely on metals, inorganic semiconductors, and oxide dielectrics to propagate signals through transport and accumulation of electronic charges (electrons and holes), leading to a fundamental mismatch in signal transmission. Organic bioelectronic materials have significant advantages over traditional semiconductors and metals, making them superior candidates for next generation interfaces with biological systems.^{1,2} Organic materials have proven especially effective at interconverting ionic and electronic signals, thus efficiently bridging the ionic world of biology with contemporary microelectronics. Further, organic materials can be solution processible, can form soft, flexible devices that conform to the complex curvilinear surfaces of living organisms, and can decrease the mechanical mismatch between electronic devices and the surrounding biological material. Herein we review the recent advances in organic bioelectronics, highlighting new materials and applications.

Conjugated Polymeric Mixed Conductors

Within the larger field of organic electronic materials, there exists a subset of mostly polymeric materials that are mixed conductors (both ionic and electronic), making them especially powerful for bioelectronic applications. These conjugated

polymeric mixed conductors can efficiently transport charge through both the transport of holes and/or electrons (electronic conduction) and via mass transport of ionic species (ionic conduction). The transport of electronic charge in these materials occurs via hopping along and between the π -conjugated backbones of the polymer chains. Ionic transport occurs via the intercalation and drift or diffusion of ions in the void spaces between the polymer chains, with solvent swelling of polymers often increasing the ease of ion motion. However, simultaneous ionic and electronic transport is not sufficient for bioelectronic applications. Crucially, there must also exist strong ionic-electronic coupling such that ionic currents can induce electronic currents and vice versa. In conjugated polymeric mixed conductors, this occurs via the redox process of electrochemical doping, where ionic species stabilize mobile electronic charges along the polymer backbone. In bioelectronic devices, this ionic-electronic coupling manifests itself as conversion, or transduction, from biological ionic signals to electronic signals.

Organic mixed conductors are especially efficient ionic-electronic transducers and interact with biological systems in a three-dimensional manner, an improvement over traditional metal or semiconductor materials that only interact with a biological system across a two-dimensional interface (**Figure 1A**). Polymeric mixed conductors can swell with and access ions and water molecules from the biological medium throughout the entire volume of the polymer, thus enabling a 3-dimensional

interfacing surface area (Figure 1B). The permeable polymer presents no ionic barrier at the material-electrolyte interface, massively increasing the effective interfacial area while avoiding the many complications that occur at discrete solid-electrolyte interfaces such as native oxides, dangling bonds, corrosion, and surface reorganization. Given this, an important figure of merit for mixed conducting polymers is the volumetric capacitance, C^* , which is a measure of the magnitude of ionic-electronic coupling per unit volume. This capacitance is critical because the magnitude of the ion-electronic coupling directly determines the strength of ionic to electronic signal transduction.³ Given that mixed conducting polymers have high accessible surface areas and large volumetric capacitances (in contrast to traditional microelectronic materials' limited surface areas and low volumetric capacitances), biological probes fabricated from polymers can have orders of magnitude higher capacitance, lower interfacial impedance, and thus vastly improved signal transduction compared to identical volume metal or semiconductor probes.

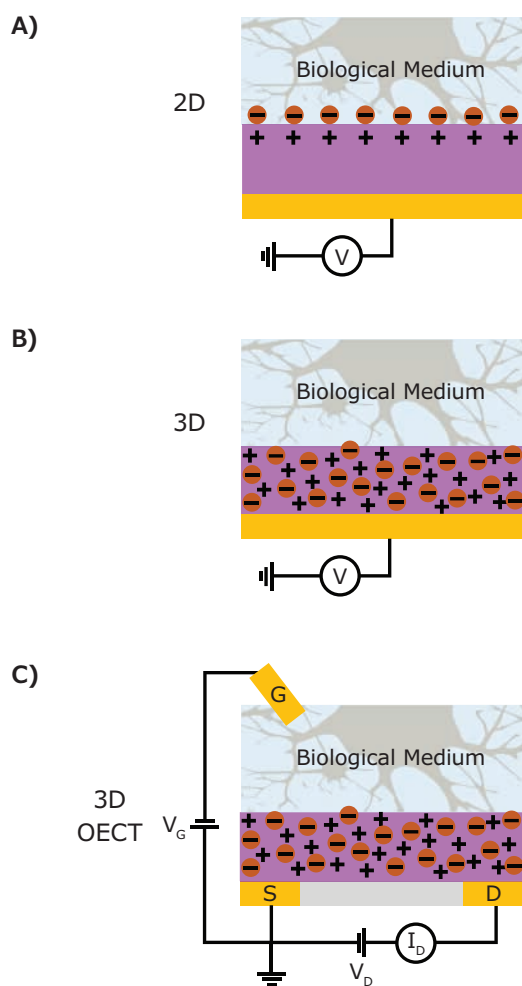


Figure 1. Schematic diagram of the various bioelectronic interfaces. **A)** A two-dimensional high impedance interface at an ion-impermeable electrode. **B)** A low impedance three-dimensional interface in a mixed conductor electrode. **C)** The same mixed conductor incorporated into organic electrochemical transistors (OEET).

Beyond the volumetric effect, conjugated polymer mixed conductors can be employed as the channel material in devices for biological recordings, such as organic electrochemical transistors (OEET). Transistors are electrical switches where a semiconductor is modulated between a conductive (on) state and a resistive (off) state. In OEETs, the electrochemical doping mechanism that allows for efficient ionic to electronic current transduction also modulates the electrical conductivity of the conjugated polymer. The strength of this effect, the change in conductivity with change in volumetric charge density, is represented as a transconductance (g_m). In an OEET architecture interfaced with a biological environment, the electrical conductivity of the mixed conductor film can be monitored rather than the potential by harnessing the transconductance. By appropriately biasing the OEET, the change in conductivity induced by the biological signals can be large as determined by the device transconductance, effectively amplifying the biological signals (Figure 1C). This allows a single mixed conducting material to simultaneously perform efficient transduction and amplification of biological signals directly at the biotic-abiotic interface.

PEDOT:PSS Based Bioelectronics

By far the most widely employed polymeric mixed conductor in organic bioelectronics research has been PEDOT:PSS. Extensively employed in antistatic coatings and organic photovoltaic (OPV) research for over two decades, PEDOT:PSS (Cat. Nos. **900181**, **655201**, **739324**) is a blend of the conjugated polymer poly(3,4-ethylenedioxythiophene) (PEDOT) and the polyelectrolyte poly(styrenesulfonate) (PSS). A fraction of the PSS repeat units are deprotonated, and the resulting negatively charged sulfonate units stabilize holes on the PEDOT, effectively doping it to produce an electrically conductive composite. PEDOT:PSS and other PEDOT-based inks (Cat. Nos. **900442**, **901047**, **675288**) are typically formulated as dispersions; when cast in a film, the materials exhibit conductivities in the range of $10\text{--}1,000\text{ S cm}^{-1}$ depending on formulation and processing additives. In the thin film state, PEDOT:PSS forms a microscale morphology of intermixed PEDOT-rich and PSS-rich phases. PSS readily swells upon exposure to water, thus providing efficient pathways for ion transport within PEDOT:PSS films. Due to the high miscibility of PSS with water, crosslinking agents are often necessary to prevent redispersion and maintain the film stability. While the extensive use of PEDOT:PSS is in part due to its commercial availability, PEDOT-based materials synthesized via electropolymerization and vapor phase polymerization have also been effectively employed in bioelectronic applications.

PEDOT-based materials have been incorporated into a wide variety of devices and applications, of which only a brief selection can be covered here (Figure 2). For measurement and recording of biological signals, PEDOT:PSS incorporated in OEET structures has been employed in both high quality electroencephalography (EEG)⁴ and in conformal arrays in subcranial electrocorticography (EGoG).⁵ Biological growth has been measured by employing PEDOT:PSS cell scaffolds

to measure cell growth, motility, or coverage via impedance changes.⁶ In addition to measuring biological activity, PEDOT-based materials can also control and stimulate biological activity. When used as a cellular substrate, the redox state of PEDOT:Tosylate can be tuned to control adhesion and density of epithelial and neural stem cells.^{7,8} In an OECT configuration, PEDOT:PSS can depolarize local neuronal membranes generating action potentials. Additionally, these PEDOT:PSS OECTs can be fabricated on delaminating flexible parylene probes that can reside *in vivo* for a month without glial scarring, decreasing their stimulating electrode efficacy due to the decreased mechanical mismatch between the probe and surrounding brain tissue.⁹

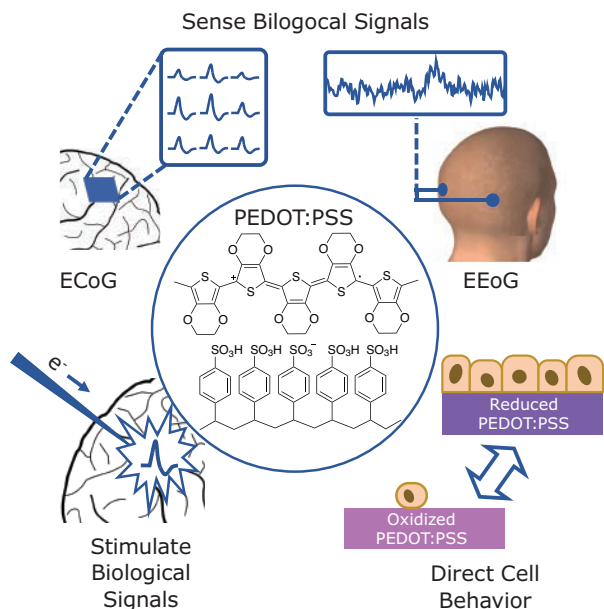


Figure 2. Structure of PEDOT:PSS and examples of applications in electrical recording and stimulation. Sensing biological signals via ECoG and EEG, stimulating local neuron action potentials by depolarization with electrical currents, and directing cell growth with redox switchable substrates.

When stimulating biological material, an electrical signal is transduced into an ionic signal, where the ionic currents are comprised of the ionic species present in the biological environment. In certain applications it is desirable to induce a current of a particular ionic species, especially in neurological applications where neuronal activity is gated by ion- or neurotransmitter-specific channels. With this application in mind, PEDOT:PSS has been used in organic electronic ion pumps.¹⁰ Ion pumps drive cations from a reservoir, through a cation exchange membrane (CEM) such as PSS (**Cat. Nos. 243051, 434574**) or poly(styrene sulfonate-co-maleic acid) (PSSA-co-MA), to a location of interest (**Figure 3A**). The geometry of the ion pump is determined by lithographic patterning, with the cation delivery location specifiable on the micron scale. In order to produce the driving potential, an electrode material is necessary to act as an oxidizable source within the cation reservoir and a reducible sink in the delivery environment, return reservoir, or waste.

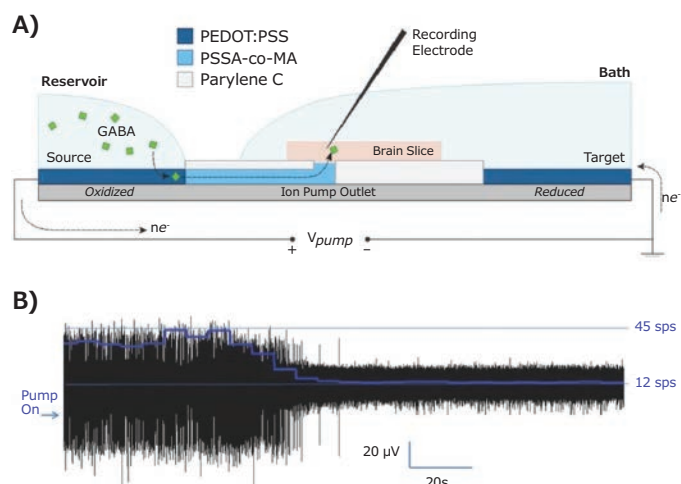


Figure 3. Chemical release with organic electronic ion pumps (OEIP). **A)** Schematic diagram of a PEDOT:PSS based ion pump performing local delivery of GABA inhibitory neurotransmitter and **B)** the typical response showing suppression of hyperexcited brain slice using OEIP GABA delivery.¹¹

The volumetric capacity of PEDOT:PSS makes it an ideal redox electrode material for ion pumps, and has enabled the delivery of suitable ion concentrations to modulate neural activity.¹¹

In particular, the suppression of epileptiform activity has been reported in hippocampal slices *in vitro*.¹¹ PEDOT:PSS was able to deliver sufficient amounts of the inhibitor neurotransmitter λ -aminobutanoic acid (**Cat. No. A2129**), commonly known as GABA, to suppress epileptiform activity induced by a variety of techniques (**Figure 3B**). This showed direct ionic delivery of GABA as an apparent general method of suppressing epileptiform activity without the solvent or osmotic stressors associated with fluidic delivery. Further, ion pump-driven GABA delivery was highly site specific, with no measured GABA inhibition in adjacent hippocampal areas. Ion pump delivery of GABA has been demonstrated *in vivo*, with ion pumps performing localized cortical and spinal cord delivery of GABA in living animal test subjects.^{12,13} Along with these applications, PEDOT-based materials have contributed to advancements in artificial muscles (actuators),¹⁴ switchable surfaces,¹⁵ and biomimetic devices such as artificial synapses for neuromorphic computing devices.¹⁶

The combination of high electrical and ionic conductivity of PEDOT:PSS, along with its commercial availability, has led to wide application of PEDOT:PSS in the field of bioelectronics for organic materials. Despite its success, PEDOT:PSS has inherent properties that limit its application. First, PEDOT:PSS is exclusively a p-type material, meaning electronic charge transport occurs solely through hole conduction. In contrast, n-type materials are electron conductors, or ambipolar materials, that can support both hole and electron conductors. Further, PEDOT:PSS is naturally a depletion mode material, meaning it is in an electrically conductive state by default, and can be electrochemically switched into a non-conductive state. This is in contrast to accumulation or enhancement

mode materials which are in a non-conductive state by default, but can be electrochemically switched into a conductive state. Thus, PEDOT:PSS is not a suitable material for the large number of applications that require n-type and/or accumulation mode materials.

Glycolated Conjugated Polymers: Beyond PEDOT:PSS

Due to the inherent limitations of PEDOT:PSS, sustained progress in the field of organic bioelectronics requires the development of new materials. By moving away from blends of separate ionic and electronic conducting polymers, recent successful approaches have resulted in single-component materials that efficiently perform both the electronic and ion transport functions. In electrically conducting polymers, backbone π -conjugation is required for efficient charge transport. Therefore, synthetic design routes to improve ion transport have recently turned to polymer side chain engineering. In the development of organic electronic materials, alkyl side chains were first added to conjugated polymers to increase their solubility in organic solvents and to improve processability. Eventually, side chain engineering became an effective route to direct polymer microstructure and morphology, thus controlling electronic properties. Due to the power of side chain engineering,¹⁷ work in this area has flourished.

To date, reported side chain engineering efforts to induce ionic conductivity have generally followed one of two routes. The first, more extensively studied route, employs side chains to tether ions to the polymer backbone, to create a conjugated polyelectrolyte.^{18,19} The second, more recently developed route, employs replacing the typically alkyl side chains of conjugated polymers with oligo-ethylene glycol side chains, consisting of repeating $\text{CH}_2\text{-CH}_2\text{-O}$ structures (glycol side chains). These glycol side chains contain polar ether oxygens that readily coordinate to both ions and water, similar to the way solid polymer electrolyte polyethylene glycol behaves. Herein, we focus on the second route, which has produced most promising results of late.

Glycolated conjugated polymers for bioelectronics applications have been using the same synthetic tool box as cutting-edge polymers used in field effect transistor and photovoltaic applications. Monomers have been functionalized with polar glycol side chains prior to polymerization and polymerization was then carried out using C-C coupling reactions commonly used for conjugated polymers, such as Stille or Suzuki couplings. These methods have been used to produce a new family of glycolated conjugated polymers that are true single component mixed conductors, that are solution processible from common organic solvents, stable in aqueous conditions without crosslinking, operate as accumulation mode materials, and (depending on backbone chemistry) display either p- or n-type behavior.

While glycolated conjugated polymers for bioelectronics applications have only recently been reported, their advantageous properties have already enabled improvements

in device performance and enabled new capabilities in bioelectronics. For example, two newly synthesized glycolated polythiophenes have reportedly achieved higher C^* and transconductance g_m than PEDOT:PSS in equivalent devices.^{3,20} In the case of poly(2-(3,3'-bis(2-(2-(2-methoxyethoxy)ethoxy)ethoxy)-[2,2'-bithiophen]-5-yl)thieno [3,2-b]thiophene), p(g2T-TT), the alkyl side chain equivalent polymers were synthesized and tested to show unequivocally the role the side chain plays in determining the advantageous ionic transport into the polymer film.²¹

As with PEDOT:PSS, the high performing p(g2T-TT) was found to be a p-type material, but in contrast to PEDOT:PSS, it operates as an accumulation mode material. This allowed for the first demonstration of an OECT biosensor operated in the subthreshold regime.²² In OECTs that function as true switches, the subthreshold regime is where the initial exponential increase in conductivity occurs when switching, via electrochemical potential, from the OFF (highly resistive) to the ON (highly conductive) state. By operating in this regime, sensing circuits incorporating p(g2T-TT)-based OECTs produced high voltage gain (biological signal transduction) with very low power consumption. This is important as low power consumption is required for implantable sensors and devices. It must be noted that the subthreshold regime is not accessible in PEDOT:PSS based devices, since the electrochemical potential required to switch off the conductivity of PEDOT:PSS exceeds the stability limits (electrochemical window) of water. The efficacy of the subthreshold regime for biological sensing was validated by measuring EEG signals. The OECT EEG sensor demonstrated two orders of magnitude improvement in signal strength as compared to commercial medical electrodes. Because p(g2T-TT) based OECTs operate in accumulation mode, they can truly turn off. Thus, they are suitable for use in multi sensor arrays, where individual sensing OECTs are turned on and "read" in sequence. Combined with their low power subthreshold operation, p(g2T-TT) OECTs present exciting prospects for next generation, low power conformable implantable biosensing arrays.

Using glycol side chains has led to the development of n-type conjugated polymer mixed conductors. In general, stable, efficient n-type electron transporting conjugated materials are less frequently reported than their p-type counterparts. In general, oxygen and moisture are incompatible with stable n-type behavior, thus complete fabrication and testing in inert glove box environments is often required. Because of this, applications requiring n-type materials have often relied on carbon nanotubes (Cat. Nos. **901046, 901056, 901082, 755125, 791490, 791504, 792462**), metal oxides, or more exotic 2-D materials (Cat. Nos. **901940, 763705, 763713**). So, it is very exciting that the design of n-type conjugated polymer mixed conductors produced materials that operate in aqueous electrolytes under ambient conditions with a high degree of stability. A series of n-type polymeric mixed conductors based on naphthalene diimide

(NDI, Cat. No. **766038**), bithiophene (T2, Cat. Nos. **241636**, **577812**, **733725**, **515493**), and alkoxybithiophene (gT2) repeating units has recently been reported.^{23,24} Interestingly, statistical copolymers containing 90% glycolated NDI units and 10% alkylated NDI units (**Figure 4**) have shown improved performance over all-glycolated polymers. As with the p(g2T-TT) discussed above, these n-type polymers behave as accumulation mode materials as well.

To take advantage of n-type and accumulation mode behavior, the 90% glycolated copolymer (P-90) was applied as an electrochemical enzymatic sensor²⁵ to detect charge transfer

from an enzyme to a mixed conductor film as the target substrate was metabolized. For such a charge transfer to occur, the mixed conductor must be redox active in the same range of electrochemical potentials as the enzyme. In the case of lactate oxidase, which undergoes a reduction at positive potentials, this requires a n-type polymeric mixed conductor. When converting lactate to pyruvate, the enzyme lactate oxidase (Cat. No. **L9795**) efficiently transferred charge to the P-90 copolymer. In turn, this charge transfer modulated the conductivity of P-90 in proportion to the concentration of lactate. By operating the sensor as an OECT, the local amplification of the enzyme charge transfer to P-90 allowed for micrometer scale sensors to sense lactate concentrations down to the micromolar level.

Conclusion

Organic materials are powerful tools in the area of bioelectronics, due to their capability for mixed ionic and electronic conduction. Mixed conduction allows for vast improvements in both transduction and amplification of biological signals. Such advantages have been most widely exploited using PEDOT-based materials, especially the commercially available PEDOT:PSS. Recent developments of novel conjugated polymers with polar glycol side chains have produced significant performance gains over PEDOT:PSS, and have opened up new applications in electrochemical enzymatic sensing and low power electrophysiological measurements. Yet the field of conjugated polymer mixed conductors, especially those with glycolated side chains, remains relatively new, with plenty of novel materials and applications to be developed to raise the field of organic bioelectronics to the next level.

References

- (1) Rivnay, J.; Owens, R. M.; Malliaras, G. G. *Chem. Mater.* **2014**, *26*, 679–685.
- (2) Inal, S.; Rivnay, J.; Sui, A.-O.; Malliaras, G. G.; McCulloch, I. Acc. *Chem. Res.* **2018**, *51*, 1368–1376.
- (3) Inal, S.; Malliaras, G. G.; Rivnay, J. *Nat. Commun.* **2017**, *8*, 1767.
- (4) Rivnay, J. et al. *Sci. Adv.* **2015**, *1*, e1400251.
- (5) Khodagholy, D. et al. *Nat. Commun.* **2013**, *4*, 1575.
- (6) Inal, S. et al. *Adv. Biosyst.* **2017**, *1*, 1700052.
- (7) Saltó, C. et al. *Langmuir* **2008**, *24*, 14133–14138.
- (8) Svennersten, K.; Bolin, M. H.; Jager, E. W. H.; Berggren, M.; Richter-Dahlfors, A. *Biomaterials* **2009**, *30*, 6257–6264.
- (9) Williamson, A. et al. *Adv. Mater.* **2015**, *27*, 4405–4410.
- (10) Isaksson, J. et al. *Nat. Mater.* **2007**, *6*, 673–679.
- (11) Williamson, A. et al. *Adv. Mater.* **2015**, *27*, 3138–3144.
- (12) Uguz, I. et al. *Adv. Mater.* **2017**, *29*, 1701217.
- (13) Jonsson, A. et al. *Sci. Adv.* **2015**, *1*, e1500039.
- (14) Smela, E. *Adv. Mater.* **2003**, *15*, 481–494.
- (15) Döbbelin, M. et al. *Adv. Funct. Mater.* **2009**, *19*, 3326–3333.
- (16) Burgt, Y. van de et al. *Nat. Mater.* **2017**, *16*, 414–418.
- (17) Jiang, H.; Taraneke, P.; Reynolds, J. R.; Schanze, K. S. *Angew. Chem. Int. Ed.* **2009**, *48*, 4300–4316.
- (18) Mei, J.; Bao, Z. *Chem. Mater.* **2014**, *26*, 604–615.
- (19) Zeglio, E. et al. *Chem. Mater.* **2017**, *29*, 4293–4300.
- (20) Nielsen, C. B. et al. *J. Am. Chem. Soc.* **2016**, *138*, 10252–10259.
- (21) Giovannitti, A. et al. *Proc. Natl. Acad. Sci.* **2016**, *113*, 12017–12022.
- (22) Venkatraman, V. et al. *Adv. Sci.* **2018**, *5* (8), 1800453.
- (23) Giovannitti, A. et al. *Nat. Commun.* **2016**, *7*, 13066.
- (24) Giovannitti, A. et al. *Adv. Funct. Mater.* **2018**, *28*, 1706325.
- (25) Pappa, A. M. et al. *Sci. Adv.* **2018**, *4*, eaat0911.

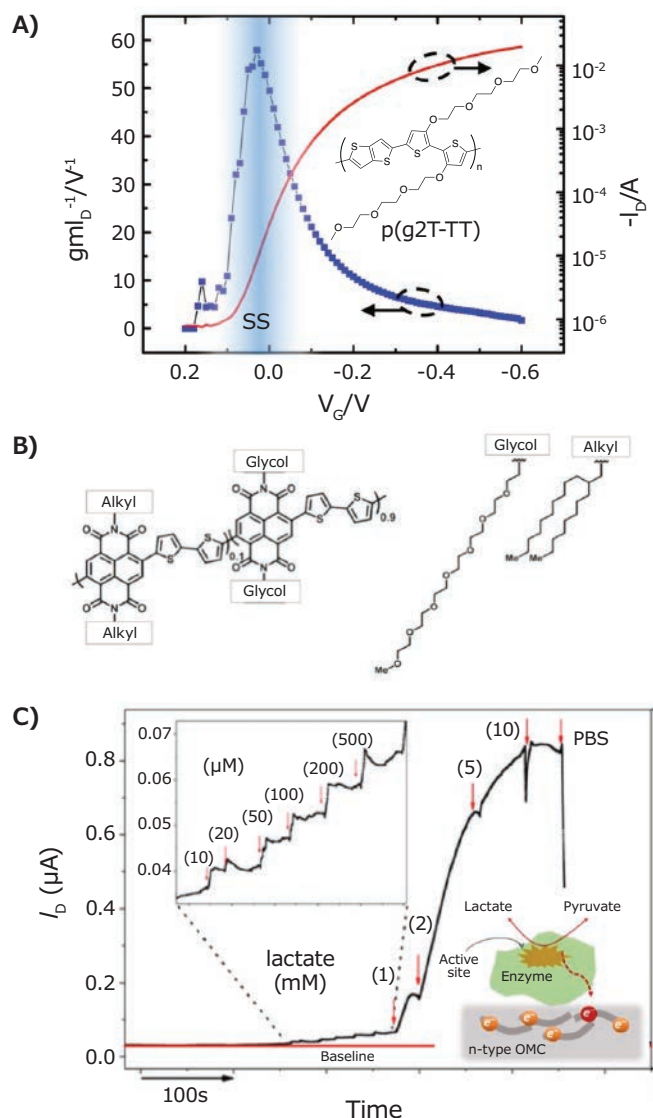


Figure 4. A) Transfer curve and normalized transconductance highlighting the subthreshold slope region of a p(g2T-TT) based p-type accumulation mode OECT,²² with inset p(g2T-TT) chemical structure. B) Chemical structure of n-type NDI 2T based statistical copolymer P-90. C) Lactate concentration dependent drain current (I_D) of a P-90 based n-type accumulation mode transistor. Inset: Micro molar lactate sensitivity and a schematic diagram of electrochemical enzymatic mechanism of lactate concentration dependent drain current (conductivity) modulation.²⁵

Poly(3,4-ethylenedioxythiophene)-poly(styrenesulfonate) (PEDOT:PSS)

Ready-to-Use Ink

Name	Sheet Resistance (Ω/sq)	Viscosity	At 22 °C	pH	Cat. No.
Graphene/PEDOT:PSS hybrid ink, dispersion in DMF	sheet resistance 500 (20 nm film: 80% transmittance)	—	—	—	900442-50ML
Molybdenum trioxide/PEDOT:PSS ink, Solid content: 0.8 wt% crystalline MoO_3 /PEDOT:PSS	—	3 cP	—	—	901047-10ML 901047-50ML
Poly(3,4-ethylenedioxythiophene)-poly(styrenesulfonate), conductive inkjet ink	sheet resistance 110	7–12 cP		1.5–2.5	739316-25G
Poly(3,4-ethylenedioxythiophene)-poly(styrenesulfonate), conductive screen printable ink	resistance 50–150	30,000–90,000 mPa.s		1.5–2.0	768650-25G

PEDOT:PSS

Sheet Resistance	Viscosity	pH	Cat. No.
resistance 500 Ω/sq (4 point probe measurement of dried coating based on initial 18 μm wet thickness.)	10–30 cP at 20 °C	1.5–2.5 at 25 °C (dried coatings)	655201-5G 655201-25G
resistance 1500 Ω/sq (4 point probe measurement of dried coating based on initial 6 μm wet thickness.)			
—	<20 cP at 20 °C	1.2–1.8	560596-25G 560596-100G
resistance <100 Ω/sq (>70% visible light transmission, 40 μm wet)	<100 cP at 22 °C	5–7	739324-100G
resistance <100 Ω/sq (<80% visible light transmission, 40 μm wet)	30–100 cP at 20 °C	<2.5	739332-100G
resistance <200 Ω/sq (>90% visible light transmission, 40 μm wet)	<18 cP at 22 °C	<2.7	739340-25G 739340-100G
resistance 200–450 Ω/sq	—	—	768618-1G 768618-5G
resistance 50–120 Ω/sq	7–12 mPa.s at 22 °C (typical)	1.8–2.2	768642-25G
sheet resistance <200 Ω/sq (by addition of 5% diethylene glycol)	—	—	900208-1G
sheet resistance <200 Ω/sq (coating : 40 μm wet, drying: 6 min 130°C)	≤ 70 mPa.s at 20 °C	—	900181-100G

Conjugated Polymer and Co-Polymer Mixed Conductor

Name	Resistivity / Conductivity	Dopant	Cat. No.
Poly(3,4-ethylenedioxythiophene), bis-poly(ethyleneglycol), lauryl terminated	conductivity 10–60 S/cm	perchlorate as dopant	687316-25G
Poly(3,4-ethylenedioxythiophene)-block-poly(ethylene glycol) solution	conductivity 0.1–5.0 S/cm (bulk)	perchlorate as dopant	649805-25G
Poly(3,4-ethylenedioxythiophene), tetramethacrylate end-capped	conductivity 0.1–0.5 S/cm (bulk)	p-toluenesulfonate as dopant	649813-25G
Poly(thiophene-3-[2-(2-methoxyethoxy)ethoxy]-2,5-diyl), sulfonated	resistivity 500–3,000 $\Omega\text{-cm}$	—	699780-25ML

High Surface Area Mixed Conductor

Name	Carbon Content	Dimensions	Origin Of Nanomaterial	Cat. No.
Carbon nanotube, multi-walled, carboxylic acid functionalized	>80% carbon basis	avg. diam. \times L 9.5 nm \times 1.5 μm	Catalytic Carbon Vapor Deposition (CCVD) Method	755125-1G
Carbon nanotube, single-walled, carboxylic acid functionalized	>90% carbon basis	D \times L 4–5 nm \times 0.5–1.5 μm (bundle dimensions)	Electric Arc Discharge Method	652490-250MG 652490-1G
Carbon nanotube, single-walled, polyaminobenzene sulfonic acid functionalized	75–85% carbon basis	D \times L 1.1 nm \times 0.5–1.0 μm (bundle dimensions)	Electric Arc Discharge Method	639230-100MG
Carbon nanotube, single-walled, poly(ethylene glycol) functionalized	>80% carbon basis	D \times L 4–5 nm \times 0.5–0.6 μm (bundle dimensions)	Electric Arc Discharge Method	652474-100MG
Reduced graphene oxide, stabilized with poly(sodium 4-styrenesulfonate)	—	—	Chemical exfoliation and reduction	900197-100ML

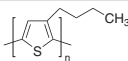
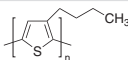
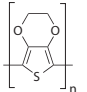
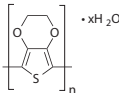
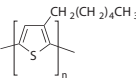
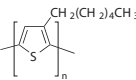
High Surface Area Conductor

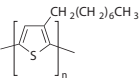
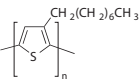
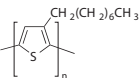
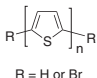
Name	Carbon Content	Dimensions	Origin Of Nanomaterial	Cat. No.
Carbon nanotube array, multi-walled, drawable	98% (carbon as CNT)	diam. × L 10–40 nm × 1.0 mm ±0.5 mm	Chemical Vapor Deposition (CVD) method.	901046-1EA
Carbon nanotube, few-walled	≥94% (carbon as CNT by TGA)	D × L 2.5–3 nm × 2–6 μm	CoMoCAT™ synthesis process	900788-250MG 900788-1G
Carbon nanotube sheet	>95% (carbon)	size × thickness 100 mm × 100 mm × 1–5 μm	Chemical Vapor Deposition (CVD) method.	901082-1EA
	>95% (carbon)	size × thickness 50 mm × 50 mm × 1–5 μm	Chemical Vapor Deposition (CVD) method.	901056-1EA
Graphene ink in water	0.1 wt. % solids in inject ink	80–500 nm	Liquid exfoliated	808288-5ML
	10 wt. % solids in screen printable ink	500–1500 nm	Liquid exfoliated	808261-10ML

Ionic Polymer

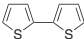
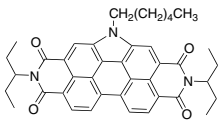
Name	Concentration Or Form	Viscosity / Average M_w	Cat. No.
Nafion® perfluorinated resin	5 wt. % in mixture of lower aliphatic alcohols and water	—	527084-25ML
Poly(acrylamide-co-diallyldimethylammonium chloride)	10 wt. % in H ₂ O	viscosity 9,000–25,000 cP at 25 °C	409081-1L
Poly(diallyldimethylammonium chloride)	20 wt. % in H ₂ O	viscosity 250–500 cP at 25 °C, 200,000–350,000 (medium molecular weight)	409022-25ML 409022-1L 409022-4L
Poly(sodium 4-styrenesulfonate)	powder	viscosity 70–170 cP at 25 °C, ~1,000,000	434574-5G 434574-100G 434574-500G
	25 wt. % in H ₂ O	~1,000,000	527491-100ML
Poly(vinyl sulfate)	—	~170,000	271969-1G 271969-5G

Conjugated Polymer

Name	Structure	Description	Cat. No.
Poly(3-butylthiophene-2,5-diyl)		M_w 54,000 (typical)	495336-1G
		—	511420-1G
Poly(3,4-ethylenedioxythiophene)		dispersion nanoparticles	675288-25ML
Poly(3,4-ethylenedioxythiophene) hydrate		nanotubes	678392-500MG
Poly(3-hexylthiophene-2,5-diyl)		average M_w 50,000–100,000	445703-1G
		—	510823-1G

Name	Structure	Description	Cat. No.
Poly(3-octylthiophene-2,5-diyl)		average $M_n \sim 34,000$	445711-1G
		average M_n 22,000 average M_w 36,600	510831-1G
		99.995% trace metals basis, average $M_n \sim 25,000$, solid	682799-250MG
Poly(thiophene-2,5-diyl), bromine terminated		powder	525936-1G

Monomer for n-type Polymer

Name	Structure	Purity	Cat. No.
2,2'-Bithiophene		99%	241636-10G
Hexyl N-annulated perylene diimide		—	901144-500MG

subscribe today

Don't miss another
topically focused technical review.

It's **free** to sign up for a print or digital
subscription of *Material Matters*™.

- Advances in cutting-edge materials
- Technical reviews on emerging technology from leading scientists
- Peer-recommended materials with application notes
- Product and service recommendations



To view the library of past issues
or to subscribe, visit

SigmaAldrich.com/materialmatters

MERCK

2D Materials Matter: A Perspective on Biosensing Applications



Chengye Dong,^{1,3,5,†} Derrick Butler,^{2,3,4,†} Rui Zhao, Yonghong Cheng,⁵ Joshua A. Robinson,^{1,3,4,*} and Aida Ebrahimi^{2,3,4,*}

¹Department of Materials Science and Engineering, The Pennsylvania State University, University Park, PA 16802, USA

²School of Electrical Engineering and Computer Science, The Pennsylvania State University, University Park, PA 16802, USA

³Materials Research Institute, The Pennsylvania State University, University Park, PA 16802, USA

⁴Center for Atomically Thin Multifunctional Coatings, The Pennsylvania State University, University Park, PA 16802, USA

⁵State Key Lab of Electrical Insulation and Power Equipment, Xi'an Jiaotong University, Xi'an, Shaanxi 710049, People's Republic of China

*E-mail: sue66@engr.psu.edu and jrobinson@psu.edu

†These authors contributed equally.

Introduction

Since its isolation in 2004, graphene's extraordinary electrical conductivity, large surface-to-volume ratio, unique optical/vibrational modes, exceptional mechanical strength, and excellent biocompatibility have drawn increasing interest for use in biochemical sensing applications.^{1–4} Furthermore, the surface of graphene, with specific defects and chemical functionalities are excellent reaction sites for catalysis and electrochemical biosensing.⁵ Successful application of graphene in various biosensing technologies has sparked exploration of other graphene-like materials, including transition metal dichalcogenides (TMDs), transition metal oxides (TMOs), transition metal carbides/nitrides (MXenes), and hexagonal boron nitride (hBN) for biosensing applications.^{6,7} The diversity of composition, structure, and functionality offered by 2D materials makes them highly suitable for developing novel biochemical sensors. Additionally, the recent progress in the engineering of 2D materials via stacking, doping, functionalization, and alloying enables the construction of even more complex structures.

This mini-review highlights recent advances in synthesis and preparation of 2D materials, with emphasis on their relevance for biosensing applications, followed by a summary of the electrochemical and optical biosensors which are the most studied 2D materials-based biosensors (**Figure 1**). In addition, some of the less-explored biosensing technologies of 2D materials will be discussed. The article concludes with a look into the future of 2D materials as biomedical analytical tools, and where research is likely to go.

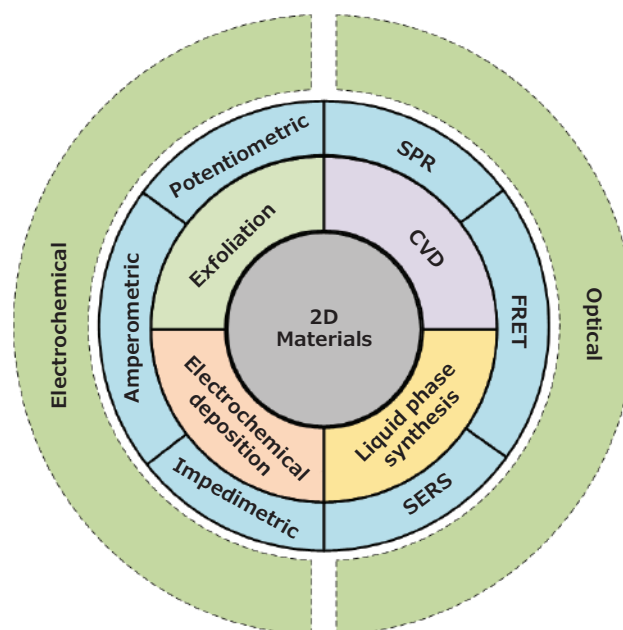


Figure 1. An overview of various synthesis methods (i.e., exfoliation, chemical-vapor deposition (CVD), electrochemical deposition and liquid-phase synthesis) of 2D materials for application in electrochemical biosensors (i.e., amperometric, potentiometric, and impedimetric methods) and optical biosensors (i.e. FRET: Forster resonance energy transfer, SERS: surface-enhanced Raman spectroscopy, and SPR: surface plasmon resonance)

Synthesis of 2D Materials for Biosensing Applications

Generally, preparation methods for 2D materials used in biosensors can be divided into mechanical and chemical exfoliation, electrodeposition, chemical-vapor deposition (CVD), and solution-phase synthesis. In this section, we focus on the synthesis of 2D layers (Figure 2) that produce to 2D flakes, powders, inks, and films.

Exfoliation

Mechanical exfoliation (or micromechanical cleavage (MC), Figure 2A) is the most-reported method for the preparation of 2D materials from bulk layered structures.¹ Although the quality of 2D flakes prepared by MC is superior to those prepared by other techniques, the high dependency on experimental skill and the poor yield limit its practical application for scalable device fabrication. On the other hand, chemical exfoliation (Figure 2B) methods are suitable for the large-scale synthesis of 2D flakes.⁸ The Li-intercalation and exfoliation method was developed to improve control over flake thickness and exfoliation yield when preparing MoS₂ (Cat. Nos. **901187**, **901867**, **808652**), TaS₂, TiS₂ (Cat. No. **808717**), WS₂ (Cat. No. **808806**), ZrS₂, NbSe₂ (Cat. No. **808679**), WSe₂ (Cat. No. **808822**), Sb₂Se₃ (Cat. No. **401196**), Bi₂Te₃ (Cat. No. **733482**), and hBN (Cat. Nos. **901349**, **901410**).⁸ While chemical exfoliation does exhibit

high yields and efficient generation of 2D flakes, modifications of the 2D surface during exfoliation can introduce defects and impurities, and the co-existing single- and multi-layered flakes are difficult to separate.

Chemical Vapor Deposition (CVD)

CVD (Figure 2C) is commonly used to synthesize 2D materials with high quality and large areas. For CVD, carbon-based precursors are introduced into a furnace at high temperature, where they react and/or decompose to deposit carbon onto substrates such as Si/SiO₂, transition metal catalysts (Cu, Ni), or sapphire, to form single- or multi-layer 2D materials. The quality, size, and thickness of the 2D materials can be tuned by experimental parameters including temperature, pressure, and substrate conditions. For example, graphene on conductive substrates with single or few layers and a centimeter-scale area has been prepared by this method, and transferred to insulator substrates for device fabrication.⁹ In addition, catalyst-free CVD graphene has been synthesized on sapphire (a dielectric substrate) eliminating the potential for damage by the transfer process and allowing fabrication of devices on directly-grown graphene.¹⁰

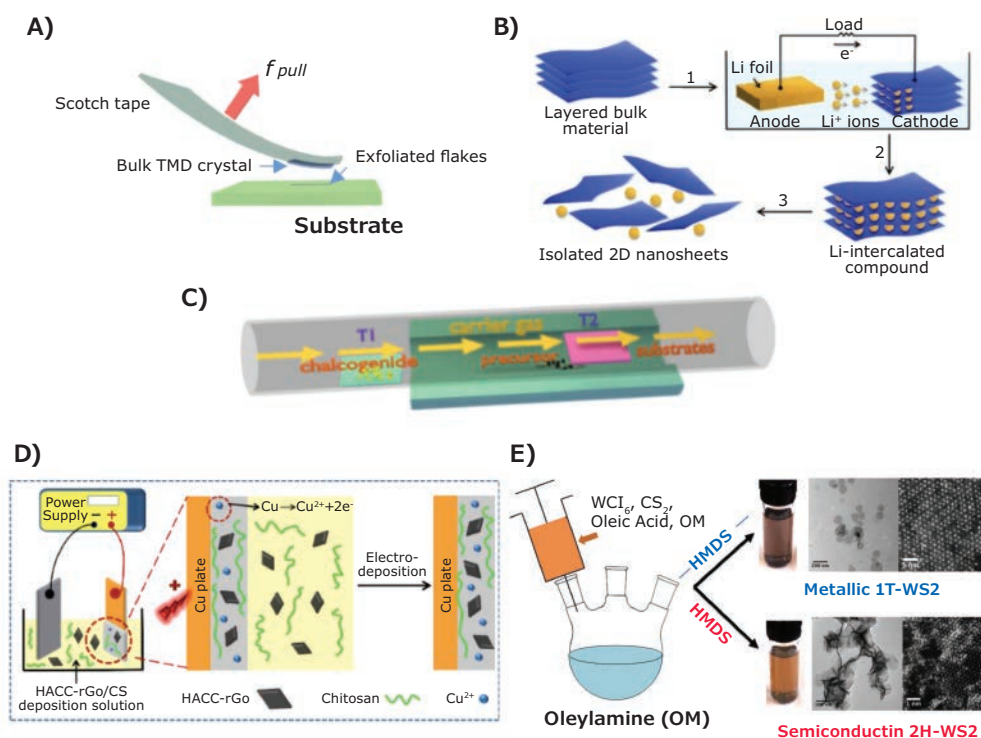


Figure 2. Methods for synthesizing of 2D materials. **A)** Mechanical exfoliation of 2D materials using adhesive tape. **B)** Electrochemical lithiation process for the fabrication of 2D nanosheets from layered bulk material. Reprinted with permission from reference 8, copyright 2011 Wiley-VCH. **C)** Schematic of CVD process for the synthesis of 2D films. **D)** Electrodeposition process of reduced graphene oxide (rGO). Reprinted with permission from reference 12, copyright 2018 Beilstein-Institute. **E)** Solution phase synthesis of 2H- and 1T-WS₂. Reprinted with permission from reference 15, copyright 2014 American Chemical Society.

Electrochemical Deposition

Electrochemical deposition (Figure 2D) is an alternative cost-effective technique for preparing thin films of nanomaterials at low temperatures. The morphology, thickness, and properties of the films can be tuned by adjusting the applied current, voltage, and deposition time. Graphene and rGO films have been electrochemically deposited on various working electrodes for biosensing applications, and some examples are discussed later in this article.^{11,12} Since such films are prepared from 2D nanosheet dispersions, films with abundant edges can be structured by other nanoparticles to enhance the signal and improve the sensitivity of the sensors.¹³ However, due to the aqueous surroundings and uncontrollable deposition process, obtaining high quality and reproducibility remains challenging.

Solution Phase Synthesis

Finally, solution phase synthesis (Figure 2E) enables production of gram-scale quantities of 2D materials with precise thickness under relatively mild conditions and low temperatures. It also allows for the functionalization of 2D materials in either aqueous or nonhydrolytic media. Recently, solution-based methods to synthesize graphene,¹⁴ TMDs (such as MoS₂, MoSe₂, WS₂ and WSe₂)¹⁵, and MXenes¹⁶ have been developed to prepare thickness- and morphology-controlled, 2D materials with high-yield and scalability. Moreover, solution phase synthesis methods allow direct preparation of specific phases of 2D materials such as 1T' MoTe₂,¹⁷ which can be difficult to access via other methods.

2D Materials for Biosensing Applications

There are an exponentially growing number of reports on the use of 2D material-based biosensors for detection of neurotransmitters (dopamine, serotonin, etc.), metabolites (glucose, lactose, ascorbic acid, adenosine, etc.), inflammation markers (reactive oxygen and nitrogen species, such as hydrogen peroxide and nitric oxide), proteins, nucleic acids, bacterial cells, and heavy metals. The following sections summarize some of the recent biosensor reports using 2D materials for electrochemical (amperometric, impedimetric, and potentiometric—which includes field-effect transistors (FETs)),^{18–21} and optical (such as FRET,²² SPR,²³ and SERS²⁴) detection of various biological targets.

Electrochemical Sensors

Compared to other technologies, electrochemical sensors are often preferred for biochemical sensing applications, especially at the point-of-care, because of their high sensitivity, fast response time, cost efficiency, and simple readouts due to compatibility with integrated circuit (IC) technology. In developing electrochemical sensors, 2D materials can serve as the actual sensing element (i.e., the working electrode or channel material) or as a substrate for further modification with metal-, metal-oxide, or carbon-nanostructures, biological enzymes, or other functional 2D materials. While many electrochemical sensors

are based on amperometric detection (i.e., change of current at a particular potential applied to a working electrode), some electrochemical sensors rely on potentiometric detection (i.e., change of a surface potential) or impedance spectroscopy (i.e., modulation of the impedance as a function of applied frequency).

Amperometric (or voltammetric) detection is based on a variety of techniques including cyclic voltammetry (CV), linear sweep voltammetry (LSV), differential pulse voltammetry (DPV), chronoamperometry, among others. Sun et al.¹⁸ used a nanocomposite electrode and DPV for the simultaneous detection of dopamine (DA), ascorbic acid (AA), and uric acid (UA) in phosphate buffered saline (PBS). Their sensor was based on a nanocomposite of MoS₂ nanosheets (Cat. Nos. **901187**, **901867**) synthesized by Li intercalation, combined with electrodeposited AuNPs (Cat. Nos. **741949**, **752568**, **808628**) and deposited on a glassy carbon electrode (GCE). The resulting sensor achieved detection limits of 50 µM, 50 nM, and 50 µM and linear ranges of 0.05–100 mM, 0.05–30 µM, and 0.05–40 mM for AA, DA, and UA, respectively. Our group showed that heterostructure of iron-sulfide with graphene enables highly sensitive and selective voltammetry detection of hydrogen peroxide down to ~0.1 nM, over a six orders of concentration range. It was shown that depending on “flavour” of graphene, the response varies significantly (with FeS/CVD graphene heterostructures outperforming FeS/n-type and /p-type epitaxial graphene layers). We specifically showed that oxidative stress induced by heat shock can be monitored *in situ* in *E. coli* cells.²⁵ For amperometric glucose detection, Rakhi et al.¹⁹ combined MXene Ti₃C₂T_x nanosheets with AuNPs to form a nanocomposite, with immobilized glucose oxidase enzyme (GOx) and coated with Nafion (Cat. No. **70160**). The sensor was able to detect at little as 5.9 µM of glucose in PBS (pH = 7) with a linear range of 0.1–18 mM (Figure 3A). The clinical values for blood glucose concentration (~5 mM) fall within this range, making it a viable sensor for real-world applications. The sensor maintained 93% of its response (at 3 mM) after 2 months of storage, demonstrating robustness and long-term stability.

Potentiometric biosensors are primarily FET-based sensors, which have attracted attention for detection of various analytes. A solution-gated potentiometric sensor for detection of glucose in PBS was developed by Zhang et al.,²⁰ using CVD-grown graphene (Cat. Nos. **900415**, **900443**, **900445**, **773719** and **773700**) for both the gate and channel. The gate electrode was modified with PtNPs (Cat. Nos. **685453**, **771937**) and GOx, which catalyzed glucose oxidation, resulting in the production of H₂O₂. The H₂O₂ was then oxidized, effectively altering the gate voltage. This was indirectly used to determine the glucose concentration (Figure 3B) with a glucose detection limit of 500 nM, which is low enough for non-invasive detection in samples like saliva and sweat. Impedimetric sensors rely on changes to either the Faradaic or non-Faradaic impedance in the presence or absence of a target analyte. For the Faradaic detection of *Salmonella*, Jia et al.²¹ developed a composite of rGO/MWCNTs,

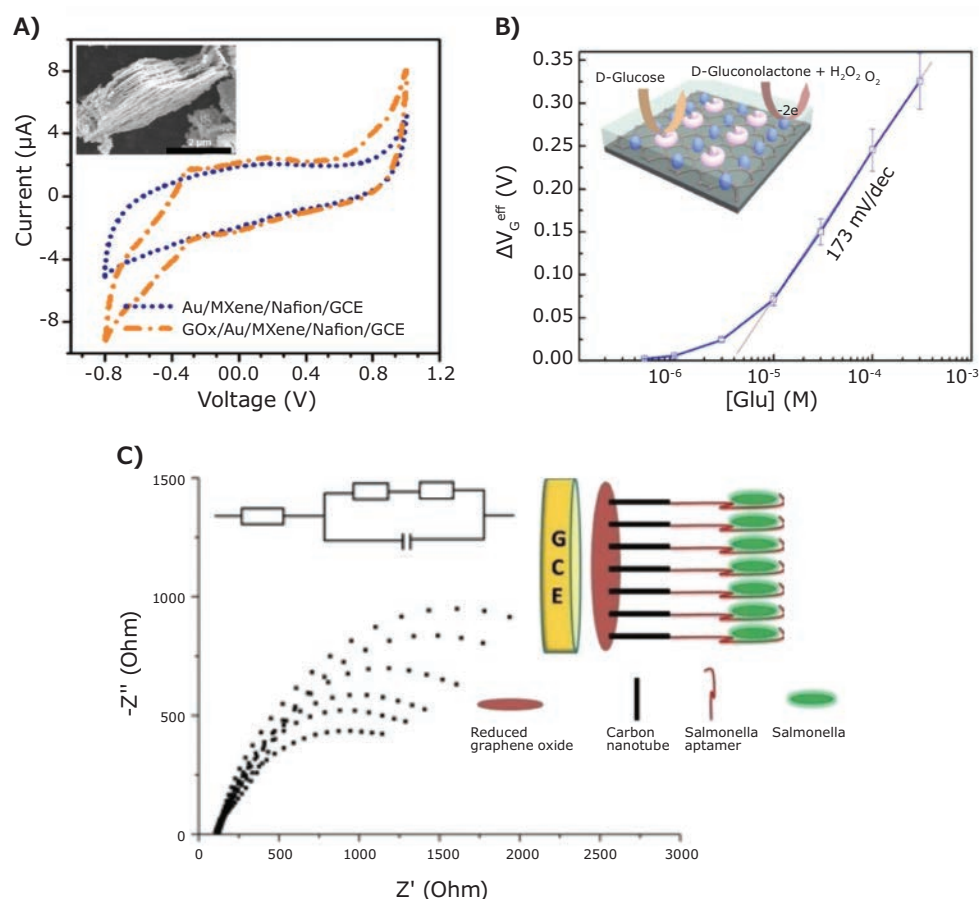


Figure 3. Examples of electrochemical sensors utilizing amperometric, potentiometric, and impedimetric transduction mechanisms. **A)** The addition of glucose oxidase (GOx) enhances the peak current response to glucose for the MXene/AuNP/Nafion/GOx composite developed by Rakhi et al.¹⁹ The inset shows an SEM image of the MXene layers coated with AuNPs (scale bar = 2 μm). **B)** A potentiometric sensor utilizing graphene for both the gate and channel material for the indirect detection of glucose. GOx and PtNPs modify the gate electrode, resulting in generation of H_2O_2 upon reaction with glucose. H_2O_2 is oxidized resulting in an effective change in gate potential, which is used to determine glucose concentration.²⁰ **C)** For the Faradaic impedimetric detection of *Salmonella*, Jia et al. used an aptamer-modified rGO/MWCNT composite on a GCE. The diameter of the semicircle of the Nyquist plot ($-Z''_{\text{m}}$ vs Z'_{e}) qualitatively indicates the charge-transfer resistance, as seen in the equivalent circuit model. Reproduced with permission from references 19 and 20, copyright 2016 and 2015, respectively, Nature Publishing Group.

electrodeposited onto a GCE. Once the electrode was prepared, they drop-cast an amino-modified *Salmonella* aptamer onto the electrode. Based on the change in charge-transfer resistance, they were able to detect as few as 25 colony forming units (cfu) per ml, with a linear range of 75–7.5 105 cfu/ml, in 60 minutes without any pretreatment (Figure 3C). For typhoid fever-causing *Salmonella*, the infective dose can be as low as 1,000 cells, making this sensor potentially applicable in clinical settings.²⁶

Optical Sensors

In addition to tunable electronic and electrochemical properties, 2D materials possess unique optical and vibrational properties, including photoluminescence, fluorescence quenching, second harmonic generation, and enhanced electron-photon interaction, which make them ideal for use in optical sensors.^{22–24} Common optical sensing techniques include Forster resonance energy transfer (FRET),²² surface plasmon resonance (SPR),²³ and surface-enhanced Raman spectroscopy (SERS).²⁴

Sensors based on fluorescence quenching or enhancement, such as FRET, detect changes in fluorescence in the presence/absence of a target analyte. Kong et al. fabricated a sensor for the detection of prostate specific antigen (PSA), an important marker of prostate cancer.²² Their sensor utilized Li-intercalated MoS_2 nanosheets with a fluorescent modified single-stranded (ss) DNA probe adsorbed onto the surface (Figure 4A). In the absence of PSA, the fluorescence was strongly quenched, but upon the addition of PSA, the fluorescence returned. They reported a dynamic response range of 0.5–300 ng/ml, with a linear range from 0.5–60 ng/ml. The limit of detection was 0.2 ng/ml, and the technique was selective in the presence of other common interfering proteins, including carcinoembryonic antigen (CEA). Since PSA values of 4 ng/ml or higher can be indicative of prostate cancer, this has obvious practical implications.

SPR sensors detect changes in the local refractive index in the presence or absence of a target analyte. Surface plasmons are highly sensitive to these changes. 2D materials are used to enhance the sensitivity of SPR sensors, because they integrate very well in these sensors due to their thin film nature.

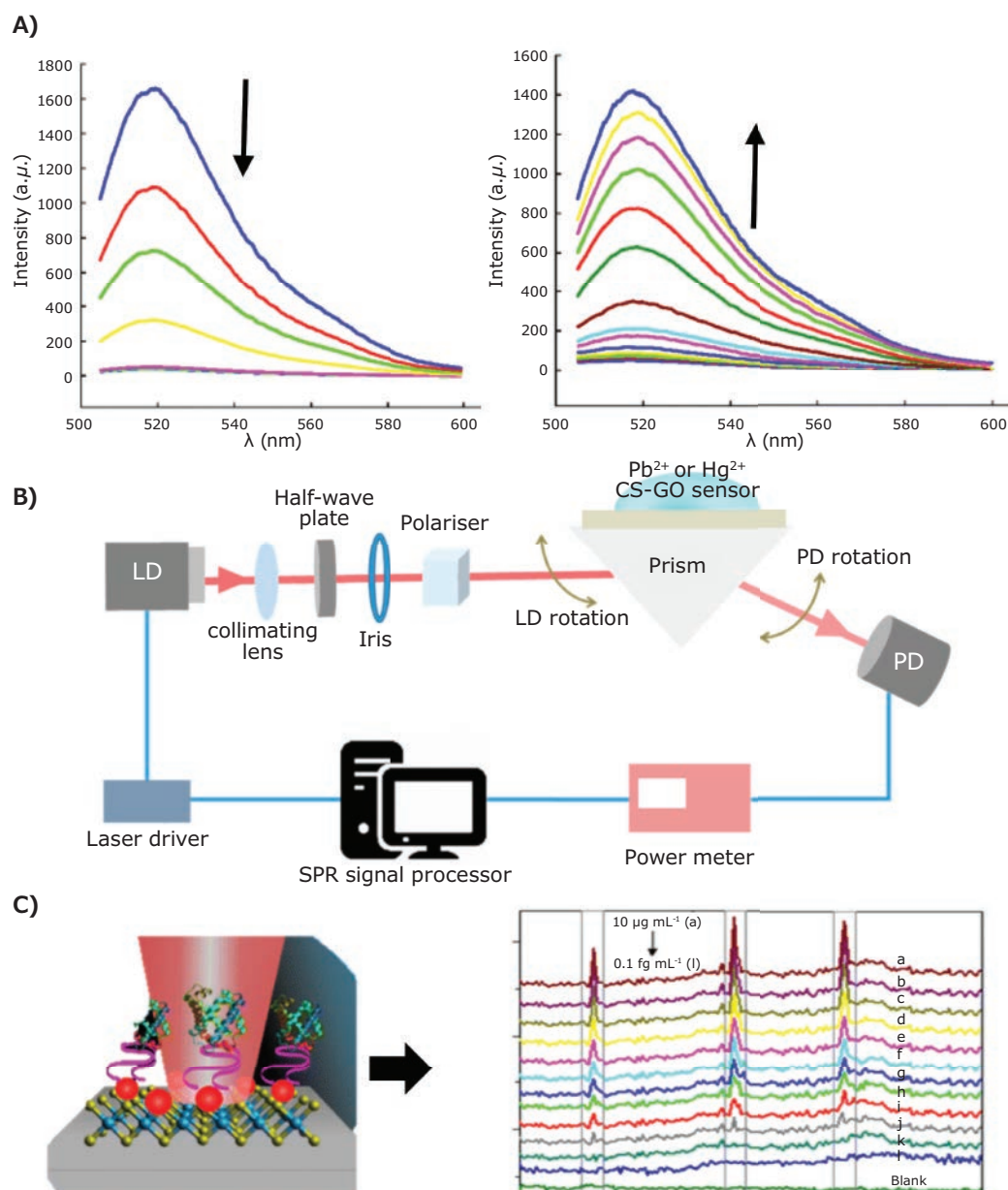


Figure 4. A) The addition of more MoS₂ nanosheets (0–40 $\mu g/ml$) for a given concentration of PSA aptamer (PA) (50 nM) quenches the fluorescence intensity. The fluorescence is restored upon increasing the concentration of PSA (0–300 ng/ml shown here). Reproduced with permission from reference 22, copyright 2015 Springer. B) The experimental setup of an SPR measurement used by Kamaruddin et al. Their chitosan-GO composite was used for the detection of Hg²⁺ and Pb²⁺ ions. Reprinted with permission from reference 23, under MDPI open access policy. C) AuNPs@WS₂ nanosheets serve as the substrate for modification with an aptamer for the SERS-based detection of myoglobin (Mb). Changes in the Raman peak intensity can be used to determine the Mb concentration. Reproduced with permission from reference 24, copyright 2018 Springer.

Kamaruddin et al.²³ combined chitosan with graphene oxide (**Cat. Nos. 763705, 763713 and 777676**) and deposited it on an Au/Ag/Au layered substrate for the detection of the heavy metal ions Pb²⁺ and Hg²⁺. By using the Kretschmann configuration (**Figure 4B**), they were able to detect less than 1 ppm for both ions, showing a slightly higher sensitivity to Pb²⁺ ions than Hg²⁺ in both linear regimes (2.05 and 0.29 $^{\circ}ppm^{-1}$ versus 1.66 and 0.20 $^{\circ}ppm^{-1}$ for Pb²⁺ and Hg²⁺, respectively).

In addition to fluorescence-based and SPR methods, SERS detects minute changes in the Raman scattering due to

adsorption of analytes to the surface. For the detection of myoglobin (Mb, **Cat. Nos. M0630, M5696**), Shorie et al.²⁴ fabricated a SERS-based sensor that combined liquid-exfoliated WS₂ nanosheets with AuNPs (**Figure 4C**). Elevated Mb levels are indicative of muscle damage, and can be used for early detection of heart attacks. In this sensor, an anti-Mb aptamer was deposited onto the surface for selective detection of Mb, and was able to detect as little as 10⁻² pg/ml, well below the blood level values (~85 ng/ml) that can indicate a heart attack or other muscle damage. The enhancement factor due to the WS₂/AuNPs was 6.78 × 10⁶.

Conclusions and Perspectives

This article summarized recent advances in synthesis of 2D materials, with a focus on their application in biosensing technologies. The advantages and disadvantages of various methods used to synthesize 2D materials as biosensing platforms was discussed. Due to the unique properties of 2D materials, novel electrochemical and optical biosensors can detect neurotransmitters, metabolites, proteins, nucleic acids, bacterial cells, and heavy metals.

Considering the enhanced sensitivity offered by 2D materials, their atomically thin nature, and the advanced functionalization capabilities, this class of materials can open new avenues in healthcare, especially in point-of-care diagnostics and flexible and/or transient bioelectronics. However, in order to take advantage of their full capabilities, further technological development and better understanding of their properties are required. First, synthesis methods for developing environmentally stable 2D materials and heterostructures at lower cost and higher material/morphological control will make them more compatible with biosensing applications, especially for flexible platforms. Second, controlling of the layer number, defect chemistry, and material phase needs to be established, because the sensing performance of 2D materials is affected by these parameters. Third, control functionalization of the 2D material surface, which has a significant impact on the optical/electronic/vibrational properties, has not been well-explored, and is an emerging research area for the community. Finally, biocompatibility and/or antibacterial properties of different 2D materials (beyond graphene, GO, rGO, and MoS₂) and how the synthesis process affects them need to be systematically investigated.

References

- (1) Novoselov, K. S.; Geim, A. K.; Morozov, S. V.; Jiang, D.; Zhang, Y.; Dubonos, S. V.; Grigorieva, I. V.; Firsov, A. A. *Science* **2004**, *306*, 666–669.
- (2) Lee, C.; Wei, X.; Kysar, J. W.; Hone, J. *Science* **2008**, *321*, 385–388.
- (3) Liu, K.; Zhang, J.-J.; Cheng, F.-F.; Zheng, T.-T.; Wang, C.; Zhu, J.-J. *J. Mater. Chem.* **2011**, *21* (32), 12034.
- (4) Hendry, E.; Hale, P. J.; Moger, J.; Savchenko, A. K.; Mikhailov, S. A. *Phys. Rev. Lett.* **2010**, *105* (9), 1–4.
- (5) Wang, Y.; Li, Z.; Wang, J.; Li, J.; Lin, Y. *Trends Biotechnol.* **2011**, *29* (5), 205–212.
- (6) Li, Z.; Wong, S. L. *Mater. Sci. Eng. C* **2017**, *70*, 1095–1106.
- (7) Luo, Y.; Li, Z.; Zhu, C.; Cai, X.; Qu, L.; Du, D.; Lin, Y. *Biotechnol.* **2018**, 1–12.
- (8) Zeng, Z.; Yin, Z.; Huang, X.; Li, H.; He, Q.; Lu, G.; Boey, F.; Zhang, H. *Angew. Chemie - Int. Ed.* **2011**, *50* (47), 11093–11097.
- (9) Kim, K. S.; Zhao, Y.; Jang, H.; Lee, S. Y.; Kim, J. M.; Kim, K. S.; Ahn, J. H.; Kim, P.; Choi, J. Y.; Hong, B. H. *Nature* **2009**, *457* (7230), 706–710.
- (10) Fanton, M. A.; Robinson, J. A.; Puls, C.; Liu, Y.; Hollander, M. J.; Weiland, B. E.; LaBella, M.; Trumbull, K.; Kasarda, R.; Howsare, C.; et al. *ACS Nano* **2011**, *5* (10), 8062–8069.
- (11) Chen, L.; Tang, Y.; Wang, K.; Liu, C.; Luo, S. *Electrochem. Commun.* **2011**, *13* (2), 133–137.
- (12) Liu, M.; Chen, Y.; Qin, C.; Zhang, Z.; Ma, S.; Cai, X.; Li, X.; Wang, Y. *Beilstein J. Nanotechnol.* **2018**, *9* (1), 1200–1210.
- (13) Zhang, Y.; Zeng, G. M.; Tang, L.; Chen, J.; Zhu, Y.; He, X. X.; He, Y. *Anal. Chem.* **2015**, *87* (2), 989–996.
- (14) Yan, X.; Cui, X.; Li, L.; V. I. U. *J. Am. Chem. Soc.* **2010**, *132* (17), 5944–5945.
- (15) Mahler, B.; Hoepfner, V.; Liao, K.; Ozin, G. A. *J. Am. Chem. Soc.* **2014**, *136* (40), 14121–14127.
- (16) Naguib, M.; Gogotsi, Y. *Acc. Chem. Res.* **2015**, *48* (1), 128–135.
- (17) Sun, Y.; Wang, Y.; Sun, D.; Carvalho, B. R.; Read, C. G.; Lee, C. H.; Lin, Z.; Fujisawa, K.; Robinson, J. A.; Crespi, V. H.; et al. *Angew. Chemie - Int. Ed.* **2016**, *55* (8), 2830–2834.
- (18) Sun, H.; Chao, J.; Zuo, X.; Su, S.; Liu, X.; Yuwen, L.; Fan, C.; Wang, L. *RSC Adv.* **2014**, *4*, 27625–27629.
- (19) Rakhi, R. B.; Nayuk, P.; Xia, C.; Alshareef, H. N. *Sci. Rep.* **2016**, *10*, 36422.
- (20) Zhang, M.; Liao, C.; Mak, C. H.; You, P.; Mak, C. L.; Yan, F. *Sci. Rep.* **2015**, *5*, 8311.
- (21) Jia, F.; Duan, N.; Wu, S.; Dai, R.; Wang, Z.; Li, X. *Microchim. Acta* **2016**, *183*, 337–344.
- (22) Kong, R. M.; Ding, L.; Wang, Z.; You, J.; Qu, F. *Anal. Bioanal. Chem.* **2015**, *407* (2), 369–377.
- (23) Kamaruddin, N.; Bakar, A. A.; Mobarak, N.; Zan, M. S.; Arsad, N. *Sensors* **2017**, *17* (10), 2277.
- (24) Shorie, M.; Kumar, V.; Kaur, H.; Singh, K.; Tomer, V. K.; Sabherwal, P. *Microchim. Acta* **2018**, *185* (3), 158.
- (25) Ebrahimi, A. A.; Zhang, K.; Dong, C.; Butler, D.; Bolotsky, A.; Cheng, Y.; Robinson, J. A. *Sensors Actuators B. Chem.* **2019**, *285*, 631–638.
- (26) Administration, F. and D. Bad Bug Book, Foodborne Pathogenic Microorganisms and Natural Toxins, 2nd ed.; **2012**.

Transition Metal Dichalcogenide Inks and Powders

Name	Description	Cat. No.
Molybdenum disulfide	dispersion, 0.1–0.5 mg/mL in H ₂ O	900724-10ML
Molybdenum disulfide ink for inkjet printing	Resistivity: 10–100 kΩcm (thermally annealed 400 °C for 3 hours in Ar/H ₂ environment, film thickness >150 nm)	901187-5ML
Molybdenum disulfide ink for spin/spray coating	Resistivity: 75–100 kΩ·cm (Prepared by spin-coating at 1000 rpm/30 s for 1 coat, followed by thermal annealing at 400 °C in Ar/H ₂ for 3 hours)	901867-10ML
Molybdenum selenide	single crystalline monolayer flakes on SiO ₂ /Si	901473-1EA
	single crystalline monolayer flakes on sapphire	901467-1EA
Molybdenum sulfide	single crystalline monolayer flakes on SiO ₂ /Si	901479-1EA
	Single crystalline monolayer flakes on sapphire	901615-1EA
Molybdenum(IV) sulfide	powder, <2 μm, 99%	234842-100G 234842-500G
Tungsten selenide	single crystalline monolayer flakes on sapphire	901483-1EA
	single crystalline monolayer flakes on SiO ₂ /Si	901478-1EA

Name	Description	Cat. No.
Tungsten sulfide	single crystalline monolayer flakes on sapphire	901474-1EA
	single crystalline monolayer flakes on SiO ₂ /Si	901484-1EA

Boron Nitride

Hexagonal Boron Nitride Ink

Name	Form	Particle Size (μm)	Viscosity	Cat. No.
Hexagonal boron nitride ink	dispersion	≤0.3	viscosity 200–400 cP (shear viscosity at 1000 s ⁻¹ , 25 °C)	901349-10ML
	dispersion	≤0.3	viscosity 6–15 cP (shear viscosity at 1000 s ⁻¹ , 25 °C)	901410-5ML

Non-exfoliated Boron Nitride

Name	Form	Particle Size	Purity	Cat. No.
Boron nitride	dispersion	—	—	900417-50ML
	dispersion	particle size ≤500 nm	—	900710-10ML
	powder	—	—	900405-500MG
	powder	~1 μm	98%	255475-50G 255475-250G
	nanopowder	avg. part. size <150 nm (BET)	99% trace metals basis	790532-10G
	powder	—	—	900408-1G

Graphene

Name	Form	Description	Cat. No.
Boron-doped graphene	powder	Oxygen: <7.5%, B: 2.0–4.0%, C: 85–95% thickness: 1–5 layers, size 0.5–5 μm	900526-250MG
Graphene	powder	electrical conductivity >10 ³ S/m	900561-500MG
	powder	alkylamine functionalized thickness: 1–5 layers, size 0.5–5 μm	900551-250MG
	powder	silane modified thickness: 1–5 layers, size 0.5–5 μm	900552-250MG
Graphene dispersion	dispersion, 1 mg/mL (electrochemically exfoliated graphene) 1 mg/mL in DMF	sheet resistance 4.8 kΩ/sq thickness: 1–3 layers 80%, size 10 μm	900450-5ML
	≥ 0.2 mg/mL (electrochemically exfoliated graphene) DMF	thickness: 1–3 layers, size 5–10 μm	900448-50ML
Graphene ink	liquid, 2.4 wt. % (solid (graphene and ethyl cellulose) in cyclohexanone/terpineol)	for inkjet printing thickness: average 5–6 layers, size ≤3 μm	793663-5ML
	2.2–3.4 wt. % (solid (graphene and ethyl cellulose) in cyclohexanone/terpineol)	for inkjet printing photonically annealable thickness: average 5–6 layers, size ≤3 μm	900695-5ML
Graphene ink for spin/spray coating photonically annealable	dispersion (black), solids 1.8–3.0 wt. %	thickness: average 5–6 layers, size ≤3 μm	900960-10ML
Graphene ink in water	liquid, solids ~0.1 wt. % in water	inkjet printable	808288-5ML
	liquid, solids 10 wt. % in water	screen printable	808261-10ML
Graphene nanoribbons	powder	alkyl functionalized 2–15 μm × 40–250 nm	797766-500MG
	powder	2–15 μm × 40–250 nm	797774-500MG
Graphene quantum dots	powder	blue luminescent topographic height: 1–2.0 nm	900726-50MG
	powder	aqua green luminescent topographic height: 1–2.0 nm	900713-50MG
	suspension, 1 mg/mL in H ₂ O	blue luminescent topographic height: 1–2.0 nm	900708-50ML
	suspension, 1 mg/mL in H ₂ O	cyan luminescent topographic height: 1–2.0 nm	900707-50ML
	suspension, 1 mg/mL in H ₂ O	aqua green luminescent topographic height: 1–2.0 nm	900712-50ML

Name	Form	Description	Cat. No.
Monolayer graphene film	film	4 in diameter on copper foil	900415-1EA
	film	1 cm x 1 cm on copper foil, with PMMA coating	900443-4EA
	film	1 in x 1 in on copper foil, with PMMA coating Film Coverage: >98% Monolayer coverage: ≥92% (optical)	900445-1EA
	film	1 cm x 1 cm on quartz	773719-4EA
	film	1 cm x 1 cm on copper foil	773697-4EA
Nitrogen-doped graphene	powder	Electrocatalytic oxygen reduction reaction (ORR) onset potential: >-0.1 V (0.1 M KOH vs Ag/AgCl)	900416-500MG
	powder	thickness: 1–5 layers, size 0.5–5 μm	900527-250MG
Phosphorus-doped graphene	powder	thickness: 1–5 layers, size 0.5–5 μm	900529-250MG

Metal Electrode Deposition Precursor

Name	Composition	Purity	Form,	Cat. No.
Bright electroless gold plating solution	—	—	liquid	901670-250ML
Chloroplatinic acid hydrate	$\text{H}_2\text{PtCl}_6 \cdot x\text{H}_2\text{O}/\text{H}_2\text{Cl}_6\text{Pt} \cdot x\text{H}_2\text{O}$	≥99.9% trace metals basis	—	520896-1G 520896-5G 520896-25G
Electroless silver plating solution	—	—	liquid	901669-500ML
Gold(III) chloride solution	$\text{HAuCl}_4/\text{HAuCl}_4$	99.99% trace metals basis	liquid	484385-10G 484385-50G

Metal Nanoparticles

Name	Description	Absorption	Cat. No.
Gold nanoparticles	5 nm	λ_{max} 515-520 nm	900458-1EA
	5 nm	λ_{max} 515-520 nm	900470-1EA
Platinum, nanoparticle dispersion	particle size 3 nm	—	773875-25ML
Silver, dispersion	particle size 10 nm (TEM)	—	730785-25ML

Organic and Hybrid Electronics in Optical Analytical Applications



Ruth Shinar,^{1*} Joshua Wolanyk,² Rajiv Kaudal,² Joong-Mok Park,³ and Joseph Shinar^{2,3*}

¹Microelectronics Research Center and Department of Electrical & Computer Engineering, Iowa State University, Ames, IA, 50011, USA

²Department of Physics & Astronomy, Iowa State University, Ames, IA, 50011, USA

³Ames Laboratory – USDOE, Iowa State University, Ames, IA, 50011, USA

*Email: rshinar@iastate.edu, jshinar@iastate.edu

Introduction

Organic semiconductor materials and devices, such as organic light emitting diodes (OLEDs), organic solar cells (OSCs), and organic photodetectors (OPDs), continue to attract considerable interest. Their use has expanded into novel applications including photoluminescence (PL)-based (bio)chemical sensors, spectrometers-on-a-chip using OLED pixels as excitation sources and OPDs for signal monitoring, and sensitive medical devices.

Commercial viability of any sensing platform increases when all of its components can be easily integrated into a compact, field-deployable device, and is enhanced even more when the fabrication is simple, scalable, and low-cost. Traditional light sources such as lasers or LEDs cannot be easily integrated with other components due to geometrical, operational, or size constraints. One promising approach, however, is a sensing platform based on an OLED excitation source (or an array of OLED pixels), a luminescent sensing thin film, and a PL-monitoring OPD. The organic components can be easily fabricated on flexible plastic substrates, enabling development of wearable sensors and other devices. Further, while the lack of long-term stability remains a concern for OLED-based devices, many sensors are expected to be deployed in short-term or disposable situations. Traditional photodetectors (PDs) include charge coupled device arrays, photomultiplier tubes (PMTs), and inorganic photodiodes, which also hamper integrability. With their potential for miniaturization, all-organic sensors eliminate issues related to portability and deployability, simplify fabrication, and reduce cost. The ability to fabricate simplified and integrated sensors reduces the need for trained operators, while maintaining high sensitivity, with potential for use in many diverse applications. When fabricated in a small-size array, all-organic sensors can be used for monitoring multiple analytes, either by addressing a single OLED pixel individually or by

simultaneously addressing groups of pixels. Recently, the use of hybrid perovskite-based PDs (PPDs) in sensing applications has gained attention due to their fast response and high responsivity.

In this article, we summarize some of the developments in the area of organic and hybrid electronics in optical analytical applications, including biochemical sensors and the spectrometer-on-a-chip platform.^{2,3} Here, we will discuss sensing examples based on monitoring oxygen. PL-based O₂ sensors have been studied extensively,¹ and gas-phase and dissolved oxygen (DO) monitors based on them are available commercially. The development of reliable, sensitive, and compact field deployable sensors and devices for medical, biological, and water treatment applications continues. PL-based sensors are preferred for their high sensitivity, low maintenance requirements, and infrequent need for calibration. Typically an oxygen-sensitive dye (e.g., Pt or Pd octaethylporphyrin (PtOEP (Cat. No. 673625) or PdOEP), respectively) is embedded in a thin polymeric (e.g., polystyrene (PS)) or sol-gel film that is structurally integrated with the excitation source and the PD. When oxygen molecules collide with photoexcited dye molecules, their PL is quenched with a dose-dependent decrease in the PL intensity I and decay time τ . Calibration lines and thus the oxygen level can be obtained (ideally for a dynamic quenching process) using the Stern-Volmer (SV) equation:

$$I_0/I = \tau_0/\tau = 1 + K_{sv}[O_2] \quad (1)$$

where I_0 and τ_0 are the unquenched values, and K_{sv} is the film and temperature dependent SV constant. The sensitivity S is defined as

$$S \equiv I_0/I(100\% O_2) = \tau_0/\tau(100\% O_2) \quad (2)$$

Pulsing the OLED allows monitoring of the O_2 via the intrinsic attribute t . This approach is valid provided that t is much longer than both the OLED's electroluminescence (EL) decay time and the PD's response time. Monitoring t eliminates the problem of stray or background light stemming from the typically broad EL spectrum, whose long-wavelength tail often extends into the PL band of the sensing element. Additionally, when operating in the t mode, moderate changes in the intensity of the excitation source and changes in the sensing component, such as dye leaching, have minimal effect on the sensor's response. As a result, the need for frequent calibration and optical filters (needed in the I detection mode for EL long wavelength-tail blocking) is eliminated, resulting in a more compact and reliable device.

Sensitive monitoring of other (bio)chemical analytes such as glucose, lactate, cholesterol, and ethanol is often based on oxygen consumption during oxidation of the analytes that is catalyzed by their specific oxidase enzyme. For example, glucose is oxidized in the presence of glucose oxidase (GOx) and O_2 to yield gluconic acid with the oxygen reduced to H_2O_2 . Lactate oxidase (LOx) and alcohol oxidase (AOx) similarly catalyze the oxidation of lactate and ethanol, respectively. In sealed containers, where there is no DO other than the initial concentration, the change in $[DO]$ is equal to the initial analyte concentration ($[analyte]_{initial}$) if the initial DO concentration is more than the initial analyte concentration. As the analyte is completely converted into product, the final DO concentration is given by

$$[DO]_{final} = [DO]_{initial} - [analyte]_{initial} \quad (3)$$

And the SV equation becomes:

$$I_0/I = \tau_0/\tau = 1 + K_{SV} \times \{[DO]_{initial} - [analyte]_{initial}\} \quad (4)$$

Where I is intensity, and t is the lifetime. Thus, a plot of $1/t$ vs. $[analyte]_{initial}$, to generate calibration lines, will ideally be linear up to the point where the initial DO concentration is equal to the initial analyte concentration.

The OLED-based sensing platform was also utilized for monitoring relative humidity, pH, hydrazine, and anthrax lethal factor.^{1,8}

Toward All-organic O_2 Sensors

OLED/Sensing Film Integration

Figure 1A shows the original design of an OLED-based oxygen sensor with an inorganic PD in a back-detection geometry, where the OLED and the PD are on the same side of the sensing film; the OLED and the sensing film are on opposite sides of a common transparent substrate.¹ The disadvantage of this design is that the PL is partially blocked by the nontransparent OLED cathode. Figure 1B shows the use of a microcavity (μC) OLED rather than a standard bottom emitting OLED, where the OLED stack is deposited between a transparent anode such as indium tin oxide (ITO) (Cat. Nos. 703192, 576360 and 578274) and a metal cathode.⁸ In μC OLEDs, the transparent anode is replaced by a very thin semi-transparent metal to form an

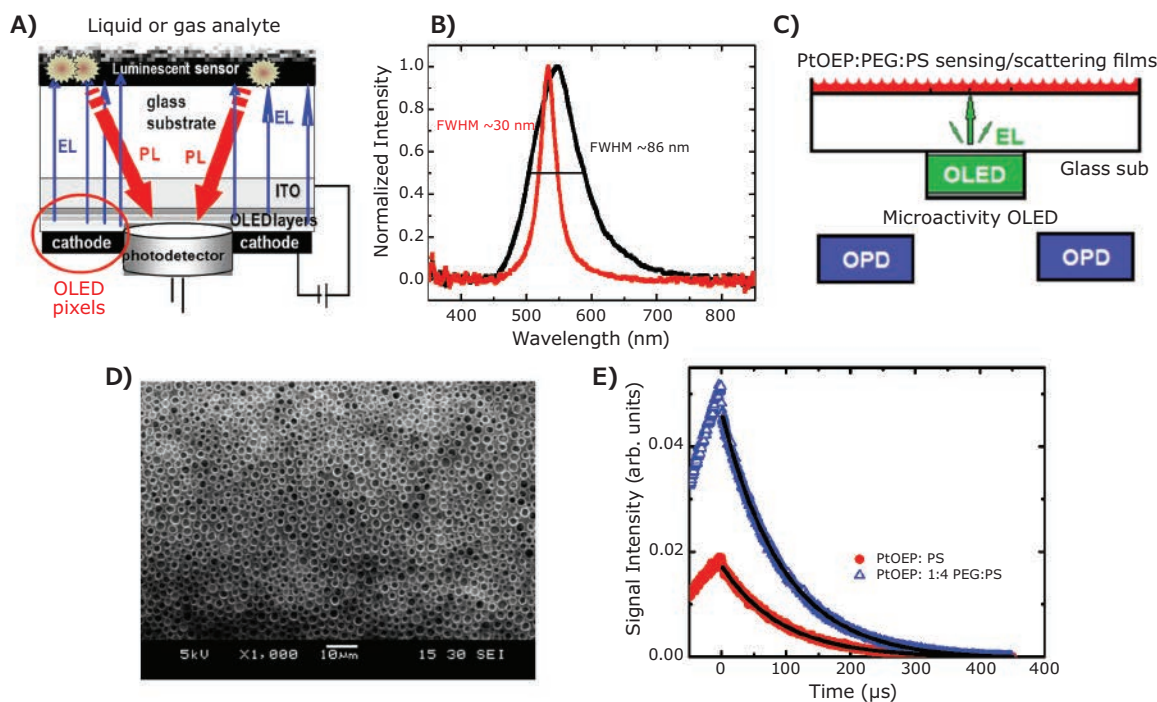


Figure 1. Toward all-organic optical (bio)chemical sensors. **A)** The initial design with two-component integration of OLED/sensing film in back-detection geometry. Reproduced with permission from reference 1, copyright 2008 IOP Publishing Ltd **B)** EL spectrum of standard and μC green OLEDs. **C)** Replacing standard OLEDs with μC OLEDs and the inorganic PD with OPDs + using an enhancing PEG-doped PS sensing film. Reproduced with permission from reference 8, copyright 2013 Elsevier B.V. **D)** SEM image of the microporous PL-enhancing sensing film. Reproduced with permission from reference 9, copyright 2011 OSA. **E)** PL intensity (measured with a PMT) vs time in a N_2 atmosphere using pulsed OLEDs, showing the increased PL signal with the PtOEP:PEG:PS sensing probe; the black lines are the exponential fits for extracting t . Reproduced with permission from reference 8, copyright 2013 Elsevier B.V.

optical cavity, with a proper design and tuned layers' thickness so it can be tailored to emit at a particular wavelength with a significantly narrowed full width at half maximum (FWHM). The sharper μC OLED EL bands minimize overlap and hence minimize interference with the PL of the sensing probe.

In **Figure 1C**, the sensing film is PtOEP:PEG:PS, where PEG is polyethylene glycol (Cat. Nos. **1546580**, **1546445** and **1546569**). The film is prepared by drop-casting a toluene solution of PtOEP:PEG:PS at specific mixing ratios. The high molecular weight PS with glass-matching refractive index $n \sim 1.55$ – 1.59 has a lower solubility in toluene than the low molecular weight PEG. Hence, during the drying process PS precipitates first, while small PEG-rich droplets form on the film's surface and in the bulk film. During evaporation the PEG droplets shrink, leaving behind surface and bulk PEG-coated PS micropores, as shown in the SEM image (**Figure 1D**) of a film with PEG:PS ratio of 1:4.⁹ The film resulting from this process enhanced the PL signals 2.7 fold compared to PtOEP in a PS matrix without PEG, as shown in **Figure 1E**. Using the PtOEP:PEG:PS sensing improved sensitivity from $S \sim 11$ to $S \sim 21$. Results for OPD replacing inorganic more bulky PDs are described later.

Figure 2 illustrates detection of multiple analytes in solution following an OLED excitation pulse using two different designs of integrated sensors.¹⁰ **Figure 2A** shows the sensor array in operation, where analysis is performed consecutively using a single inorganic PD.

Also shown in **Figure 2A** are the PL decay curves and decay times for oxygen, glucose, ethanol, and lactate. Pixel pairs 1 and 6 show the green EL of bare OLEDs. Pixel pairs 2–5 show the pixels' response to the analytes. The orange color results from the mixture of green EL background and red PL of the PtOEP:PS sensing film. In the other design (**Figures 2B and 2C**) the analytes' detection is simultaneous with the solutions in sealed containers. This design is more compact (**Figure 2B**), with the sensing films on glass serving as the bottom of the containers. Each container contains an analyte or a mixed solution of the analyte and a specific enzyme that catalyzes its oxidation. The OLED pixels are individually addressable, and can operate simultaneously as well. The pixels are defined by the overlap between the mutually perpendicular ITO and Al electrode stripes. The pixel size is typically $2 \times 2 \text{ mm}^2$, though $0.3 \times 0.3 \text{ mm}^2$ pixels have also been tested and found similarly adequate for use as the excitation source. There was no crosstalk between

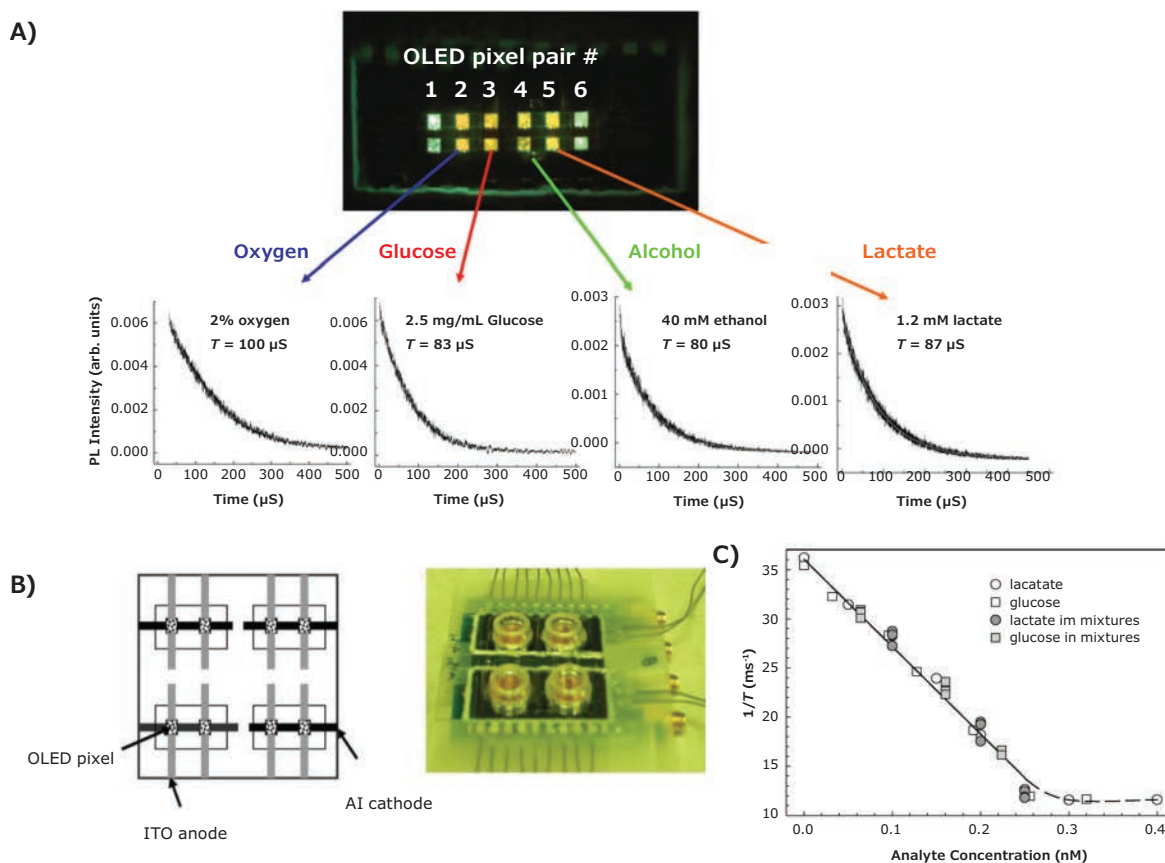


Figure 2. PL-based multianalyte detection of oxygen, glucose, ethanol, and lactate, using a structurally integrated OLED-based platform. **A)** Multipixel excitation platform with a single PD. **B)** Schematic and image of the multianalyte sensor array with 4 Si photodiodes. The four sample holders contain (i) no enzyme, (ii) glucose oxidase, (iii) ethanol oxidase, and (iv) lactate oxidase. **C)** $1/t$ vs the initial glucose or lactate concentrations, separately (open symbols) and in mixtures (grey symbols); the sensing films are at the bottom of sealed containers. Reprinted with permission from reference 10, copyright 2008 Elsevier B.V.

the OLED pixels, and two pixels were used for each of the four analytes. **Figure 2C** shows calibration lines of $1/t$ vs glucose or lactate concentration, and analysis results for solutions with analyte mixtures. As expected, the lines follow **Eq. (4)** perfectly. These latter results point to a lower limit of detection (LOD) of ~ 0.02 mM analyte.

In a similar approach, the viability of an OLED-based sensing platform was demonstrated for a lab-on-CD.¹¹ This platform is promising for commercial applications, due to its simple control of fluid flow via CD rotation, suitability for various samples at a wide range of flow rates, compactness, and versatility of functions.^{12–15} In addition, since the lab-on-CD is fabricated on plastic substrates it is low cost, disposable, recyclable, feasible for high-volume manufacturing, and biocompatible. Furthermore, the thin OLEDs can be easily integrated with the CD, and are also compatible with microfluidic architectures.

Microfluidic features were generated by ultrasonic microembossing on foamed polypropylene (PP) CDs. The embossed features functioned as reservoirs, channels, valves, and reaction chambers (**Figure 3A**). A compatible array of two mm thick surface mounted Si based photodiodes as PDs was designed. The combination of the OLED/PD arrays and the microfluidic structures enabled simultaneous monitoring of glucose, lactate, ethanol, and DO in four separate CD segments using a standard CD player compatible with a PC. The concentration of the analytes was determined following CD rotation for reagent mixing and flow direction. In one monitoring approach, ~ 200 μ L of known analyte concentrations were loaded into the reaction chamber (RC) and ~ 30 μ L of the appropriate enzyme solution was loaded into an enzyme chamber in the bio-CD. Following CD rotation, the appropriate valve (i.e., an enlarged section in the microfluidic channel) “bursts”, and the enzyme solution is directed into the sealed RC (total volume 230 μ L). Calibration curves for each of the analytes were generated and concentrations in mixtures were determined for each segment of the bio-CD. **Figure 3** shows also images of the CD-OLED-PD sensing platform.

OLED/Sensin /Thin-film PD Integration

Following integration of the OLED and the sensing film, a thin film PD was added. Inorganic PDs based on hydrogenated amorphous Si and better, nano-crystalline Si can be used, but only for monitoring intensity.¹⁶ The response time of such PDs is longer than the PL decay times due to charge recombination and trapping in defects, but OPDs and PPDs are more promising.

A bulk-heterojunction (BHJ) OPD based on poly(3-hexylthiophene) (**Cat. Nos. 900549, 900563 and 900550**) and phenyl- C_{61} -butyric acid methyl ester (**Cat. Nos. 684457, 684457 and 684430**) (P3HT:PC₆₁BM) was engineered to optimize sensitivity to the red emission of the sensing film. A fast response time enabled the monitoring of analytes in both I and t detection modes.¹⁷ **Figure 4** shows the PL decay curves and the SV calibration curves using green emitting LEDs or OLEDs. The PtOEP was embedded in a TiO₂ nanoparticle (**Cat. Nos. 791547, 791555 and 798495**) doped PS matrix. TiO₂ nanoparticles improve the EL and hence PtOEP's absorption by photon scattering within the PS matrix, increasing the optical path.¹⁸ When monitoring the analytes via t , the excitation sources were operated in a pulsed mode with 100 μ s pulse width at 50 Hz.

As shown, the dynamic range and sensitivity of these first generation all-organic sensors were limited and the signals were sometimes noisy. Nonetheless, the results demonstrated initial feasibility of the all-organic sensing paradigm. Subsequent developments significantly increased sensitivity and concentration range (shown next).⁸ In particular, the use of a PPD, currently under development, is promising for sensitive detection in the time domain.

In the previous example (**Figure 4**), a polymeric P3HT:PC₆₁BM-based OPD was used. **Figure 5A** shows the external quantum efficiency (EQE) spectrum of such an OPD together with the EQE spectrum of an organic small molecule-based CuPc/C₇₀ OPD (CuPc is copper(II) phthalocyanine, **Cat. Nos. 702854, 546682 and 546674**).⁸ Also shown is the EL spectrum of the

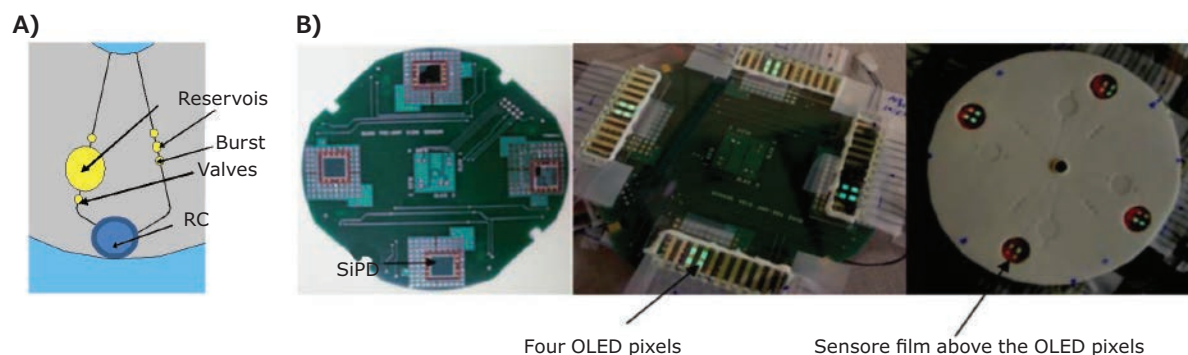


Figure 3. A) General structure of microfluidic features on lab-on-CD and B) Images of the CD-OLED/PD sensing platform: **left**—the preamplifier board with the four Si photodiodes; **middle**—the PD array and the green OLED pixels in operation; and **right**—the complete device with the sensor films (pink) on the polypropylene CD; the lit OLED pixels are also visible. The sensing films form the bottom of the reaction chambers with the OLEDs underneath. Reprinted with permission from reference 11, copyright 2010 The Royal Society of Chemistry.

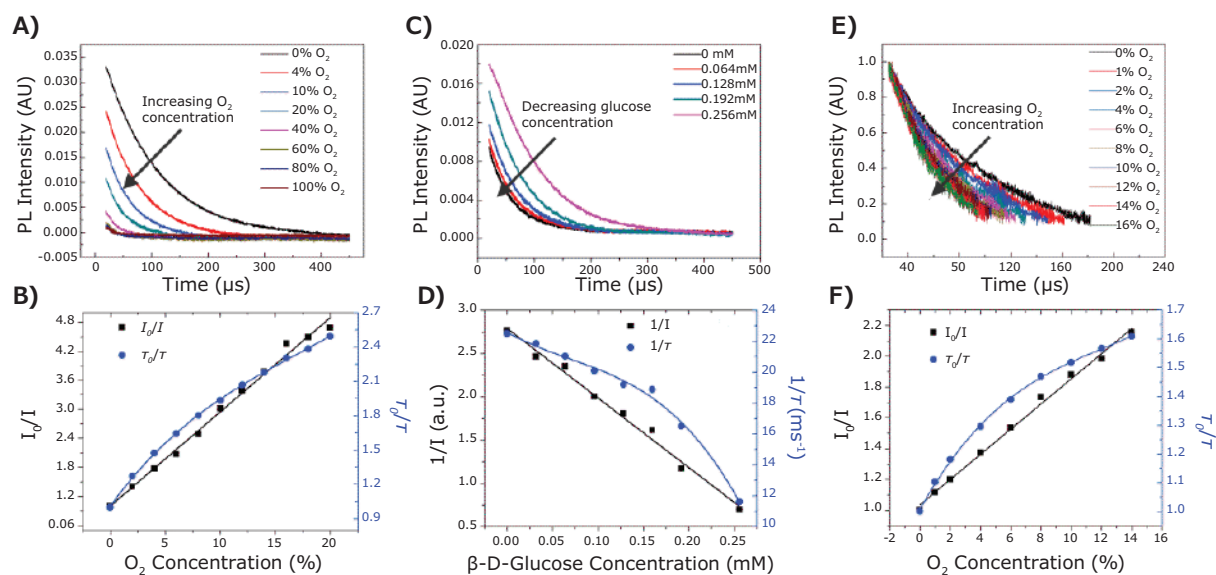


Figure 4. The effect of concentration of gas-phase O_2 A) and glucose C) on the P3HT:PCBM OPD's temporal photocurrent response. Excitation source was an LED. B) and D) are I - and t -based SV calibration curves corresponding to A) and C), respectively. For OLED excited O_2 sensor, E) and F) show the effect of O_2 concentration on the OPD's temporal response and the corresponding SV calibration curves, respectively. Reprinted with permission from reference 17, copyright 2010 WILEY-VCH Verlag GmbH & Co. KGaA, Weinheim.

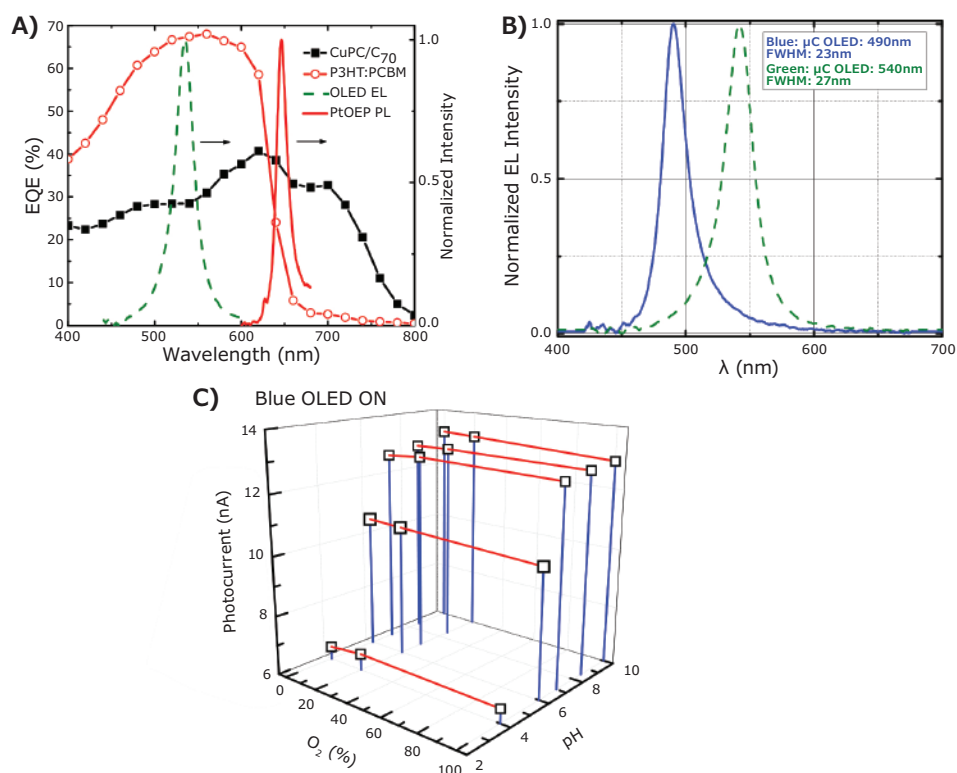


Figure 5. A). EQEs of CuPc/C₇₀ and P3HT:PCBM based OPDs. The device structures are ITO/1 nm LiF/15 nm CuPc/30 nm C₇₀/3.5 nm BPhen/120 nm Al and ITO/PEDOT:PSS/P3HT:PCBM/ Ca/Al. Also shown are the EL of the green μ C OLED (green dashed line) and red PL of the PtOEP:PEG:PS sensing film (red line). B) The EL of the green and blue μ C OLEDs. C) The signal intensity detected by the P3HT:PCBM OPD at different O_2 and pH levels with the blue μ C OLED. Reprinted with permission from reference 8, copyright 2013 Elsevier B.V.

green-emitting OLED and the red PL of PtOEP. As seen, the polymeric OPD is very sensitive to the green EL and less so to the red PL. While the EQE of the CuPc/C₇₀-based OPD is generally lower, it presents better sensitivity to PtOEP's PL and lower sensitivity to the OLED's EL.

Using these two OPDs, an all-organic sensing platform for simultaneously monitoring DO and pH was constructed.⁸ Multiple methods to improve the sensor's performance and the data analysis were utilized. Two μ C OLEDs, green and blue emitting (Figure 5B), were fabricated combinatorially with the normal

direction peak EL wavelengths designed for the O_2 -sensitive PtOEP and pH-sensitive fluorescein, respectively. In this way, 2D data for monitoring these two analytes could be extracted. Furthermore, from the transient decay signals following an OLED pulse, the PL bands related to the DO and pH could be resolved by employing both the t and I detection modes, respectively. Hence, the two analytes could be monitored simultaneously: the DO with the green μC OLED + the CuPc/ C_{70} OPD in the t mode; and the pH with the blue μC OLED + the P3HT:PCBM OPD in the I mode. Another feasible OPD is based on PTB7:PCBM (PTB7 is poly({4,8-bis[(2-ethylhexyloxy)benzo[1,2-b:4,5-b']dithiophene-2,6-diyl}-{3-fluoro-2-[(2-ethylhexyl)carbonyl] thieno[3,4-b]thiophenediyl}), **Cat. No. 772410**).³ This OPD is excellent when used in conjunction with a near UV μC OLED based on CBP (4,4'-bis(*N*-carbazolyl)-1,1'-biphenyl, **Cat. Nos. 699195 and 660124**).³ The EL of the CBP μC OLED peaks at ~ 385 nm, where the PtOEP strongly absorbs. However, it operated successfully only in the I mode.

Another example of an all-organic monolithically integrated OLED/OPD sensor was also demonstrated. Other OPDs, which can be utilized in all-organic optical sensors, are being investigated. One example is the synthesis of solution-processed PIDT-TPD (poly[4,4,9,9-tetrakis(4-hexylphenyl)-4,9-dihydro-s-indaceno[1,2b:5,6-b']dithiophene-2,7-diyl-alt-5-(2-ethylhexyl)-4H-thieno[3,4-c]pyrrole-4,6(5H)-dione-1,3-diyl]), which has several attributes that make a good OPD, including a maximal 52% EQE at 610 nm, 1 nA/cm² dark current, and a high detectivity of 1.44×10^{13} Jones under -5 V bias.

A narrow-band (FWHM <30 nm) photomultiplication-type OPD utilizing P3HT:PC₆₁BM was also described. Improvement was reported in a planar heterojunction structure with the PC₆₁BM layer positioned next to the Al cathode, allowing for a thin film (150 nm) OPD with a high detectivity under a bias of -5 V.

Hybrid Perovskite-Based PDs

While OPDs show promise as flexible devices, further improvement of their performance is hindered by their low charge mobility and long response time. In contrast, PPDs exhibit high charge mobility, EQE, sensitivity, and fast response times. Indeed, the potential of hybrid PPDs has been demonstrated in various applications. For example, a PPD with a sub-ns response time, which is promising for imagers in digital cameras, was used for measuring the PL lifetimes of organic and hybrid materials. These measurements provide insight on the material's quality, since the PL decay time is affected by defects and dopants.

Development of PPDs continues. For example, perovskite photomultipliers with high gain have been fabricated by trap- and interface-engineering using a perovskite rich in PbI₂. Tunable, narrow band (e.g., EQE FWHM ~ 28 nm) PPDs were fabricated using two perovskite layers where the first layer filters light and the second is the active layer. The sensitivity and wavelength of PPDs can be tuned by changing the bromide:iodine ratio in CH₃NH₃PbBr_{3-x}I_x in both layers. Such PPDs do not require a bandpass filter and their lowest reported time constant was ~ 100 ns, with the possibility for improvement. This

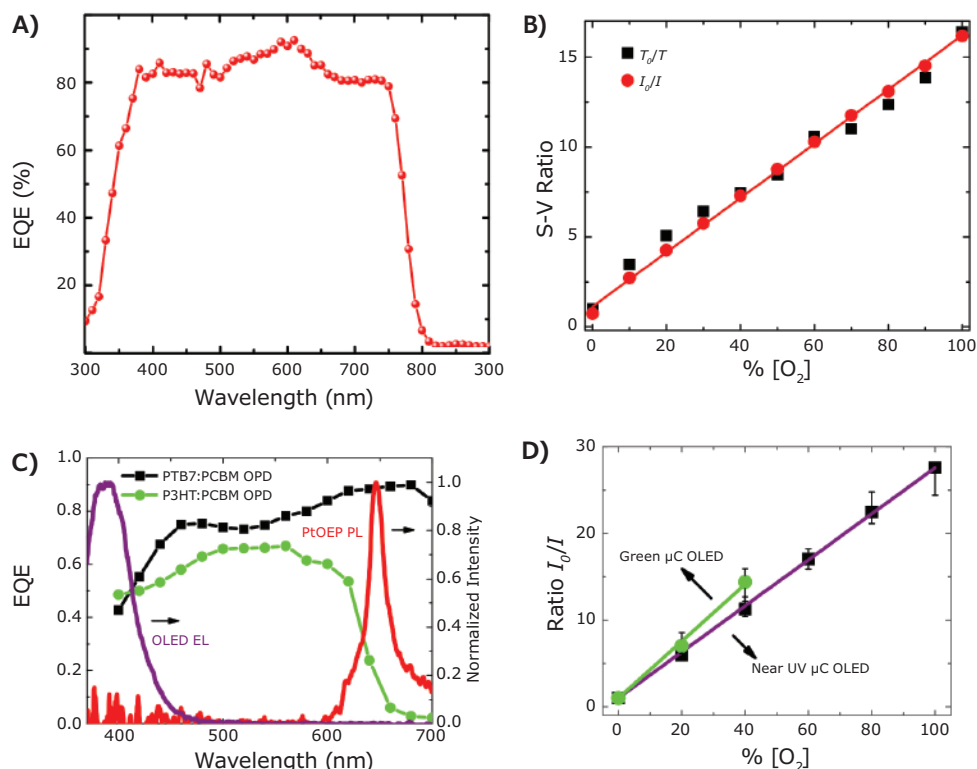


Figure 6. A) The EQE spectrum.²⁹ B) Initial results showing SV plots as measured in both I and t modes, of an ITO/PTAA/perovskite/ C_{60} /BCP/Cu PPD. C) EQE spectra of P3HT:PCBM and PTB7:PCBM-based OPDs, and the normalized EL spectrum of the near-UV μC OLED (purple line) and PL spectrum of PtOEP embedded in 1:9 PEG:PS. D) The SV ratio I_0/I for the green μC OLED/P3HT:PCBM OPD and near UV μC OLED/PTB7:PCBM OPD. Reprinted with permission from reference 8, copyright 2013 Elsevier B.V.

type of PPD is a promising approach for designing an array for monitoring multiple analytes with different, specific wavelength sensing probe emissions.

The high responsivity and fast response time of PPDs has produced promising initial results for O₂ sensing. **Figure 6** shows the EQE spectrum of a PPD with the structure ITO/PTAA/perovskite/C₆₀/BCP/Cu where PTAA is poly(triaryl amine) (**Cat. No. 702471**) and BCP is bathocuproine (**Cat. Nos. 699152 and 140910**).²⁶ As seen in **Figure 6**, the high EQE is maintained across the broad wavelength range from ~375 to ~750 nm. The ~8 mm² response time of PPDs was ~300 ns (increases with the PPD's active area), which is ~10 times faster than the PL decay time of O₂-based (bio)chemical sensors exposed to 100% gas-phase level. As such, the PPD is suitable for monitoring O₂ via the advantageous *t* measurements (**Figure 6B**). Optimization of both the PPD and the optical sensor set up are ongoing, though even at this early stage the performance exceeds that of some OPDs, in particular when measuring *t* (see **Figure 4**), with *S* ~16.

For comparison, **Figure 6** shows another set of results using all-organic O₂ sensors. **Figure 6C** shows the EQE spectrum of the viable PTB7:PCBM-based OPD.³ This OPD is excellent when used in conjunction with a near UV μ C OLED based on CBP.³ The EL of the CBP μ C OLED peaks at ~385 nm, where the PtOEP strongly absorbs and *S* ~27 (**Figure 6D**); however, so far it operates successfully only in the *I* measurement mode.

OLED/OPD Based Spectrometer on a Chip

While OLEDs have been widely studied for applications in displays and solid-state lighting, multicolor (MC) OLEDs are of interest not only for simple fabrication of display or lighting sub-pixels, but also for their use in miniaturized analytical devices. OLEDs with multiple-wavelength emission on simple substrates can operate as a compact spectrometer or form individually addressable, excitation-source pixels for bio(chemical) sensing of different analytes.¹ However, conventional OLEDs generally have broad emission spectra. With the growing industrial requirements for compact, potentially disposable analytical devices, a simpler, more economical method to fabricate narrow-band MC μ C OLEDs is highly desirable.

In this section we provide two examples of such MC μ C OLED arrays, which, when combined, cover the 370–693 nm spectral range. The approach is based on combinatorial fabrication of MC μ C OLEDs, where the precise value of the peak emission wavelength $\lambda_{em,max}$ is controlled by the optical cavity length $l_{\mu C}$, and $l_{\mu C}$ is controlled by the thickness of a “spacer” layer fabricated between the metal electrodes of the OLED, which also serve as the μ C mirrors. The second example (which expanded the spectral range down to 370 nm) demonstrates additional integration of OPDs with the MC μ C OLED array, and provides guidance in designing OPDs for optimal sensitivity and performance.

In the first example,² covering the 493–693 nm band, a layer of MoO_x was used as the spacer. Sub-stoichiometric MoO_x (*x* <3)

(**Cat. No. 900151**) is widely used as a hole injection layer (HIL) due to its ease of processing, high conductivity, and favorable energy alignment. As shown by Liu et al.,² it is also a good injection and spacer material for tuning the optical length of μ C OLEDs, while maintaining favorable current density-voltage (*J-V*) behavior. Additionally, it is found that MC μ C OLEDs with this heat-resistant HIL are more stable at high voltages, with enhanced maximum normal direction EL. This is beneficial for sensitive sensors, which may require intense excitation.

To demonstrate the potential of the OLED-based spectrometer-on-a-chip, Liu et al.² fabricated 2D combinatorial arrays of blue-to-red ~1.5 mm diameter μ C OLED pixels on a 2 in. x 2 in. glass/ITO substrate by thermal evaporation (**Figure 7A**). The 2D MC μ C OLEDs were obtained by simply changing the Alq₃ layer thickness during combinatorial fabrication. The structure of the 12 pixels was:

40 nm Ag/*x* nm MoO₃/49 nm α -NPB/1 nm 8 wt% Ir(MDQ)₂(acac): α -NPB/*y* nm Alq₃/1 nm LiF/~100 nm Al

where α -NPB is *N,N'*-di(1-naphthyl)-*N,N'*-diphenyl-(1,1'-biphenyl)-4,4'-diamine (**Cat. Nos. 556696 and 734594**), Ir(MDQ)₂(acac) is iridium (III) bis(2-methyldibenzo [f,h] quinoxaline) (acetylacetonate) (**Cat. Nos. 901074 and L512206**), Alq₃ is tris(8-hydroxyquinoline) Al III (**Cat. Nos. 444561 and 416282**), *x* = 2, 5, 10, 15, 20, or 35 nm, and *y* = 56 (Devices A) or 64 nm (Devices B).

The Ir(MDQ)₂(acac)-doped layer was responsible for the red emission peaking at ~610 nm and Alq₃ for the green emission peaking at ~525 nm. As *x* varied from 2 to 35 nm, with *y* fixed at 56 nm, the peak emission shifted from 493 nm sky blue (Device A-D1) to 639 nm red (Device A-D6) due to the μ C (Purcell) effect. When *y* was increased to 64 nm, the longest wavelength increased to 650 nm (Device B-D6), and additional wavelengths were added in the 493–650 nm range. Note that the narrowest FWHM was ~22 nm for device A-D1 and it broadened for thicker MoO_x layers. Importantly, at a given voltage all OLEDs' brightness and efficiencies were comparable.

A spin-coated P3HT film was used to demonstrate the spectrometer (**Figure 7B**). For each pixel, a background signal was obtained by shining the OLED directly onto the PMT, while the actual signal was collected after the light passed through the P3HT film. The ratio of the difference of the two signals to the background is related to the P3HT film absorption. As seen from the individual data points in **Figure 7B**, the resultant absorption spectrum agrees with the reference spectrum.

In the second example, combinatorial arrays of efficient, near UV/deep-blue OLEDs were fabricated, and used to demonstrate the feasibility of the spectrometer-on-a-chip down to 370 nm.³ Arrays with pixels emitting at different wavelengths in this range are of strong interest for analytical applications. In addition, these OLED arrays were combined with OPDs based on P3HT:PCBM or the more sensitive PTB7:PCBM, demonstrating an all-organic spectrometer-on-a-chip.

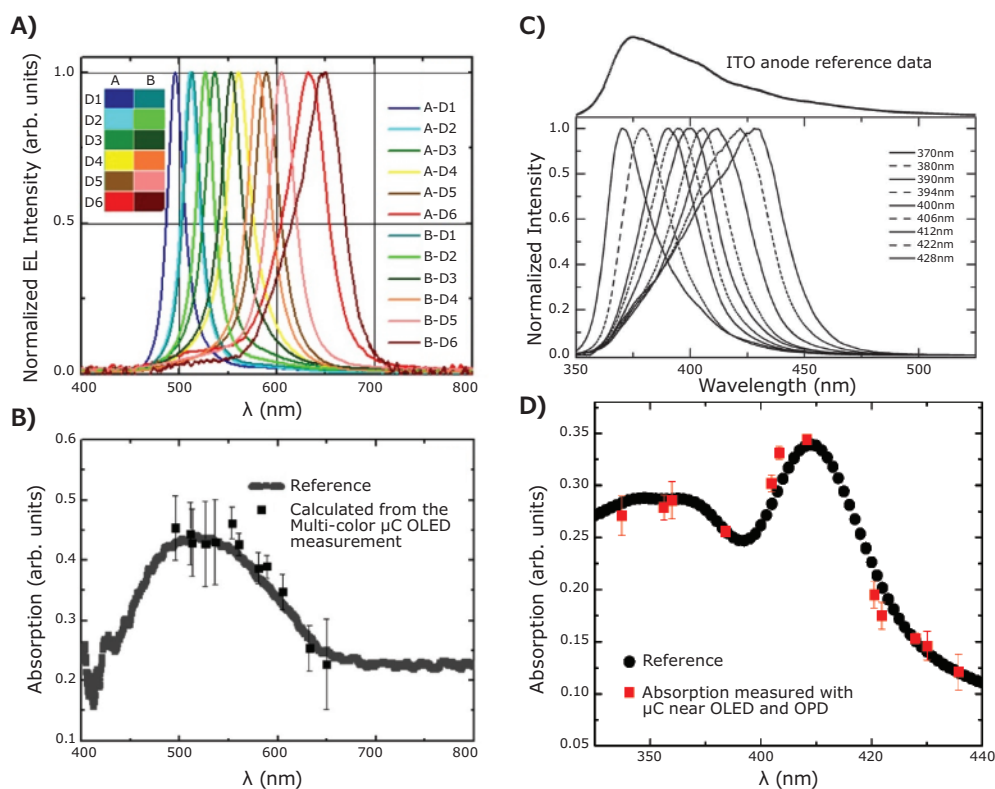


Figure 7. Spectrometer-on-a-chip. **A)** EL spectra of combinatorial array of 40 nm Ag/ x nm MoO₃/49 nm α -NPB/1 nm 8 wt% Ir(MDQ)₂(acac): α -NPB/ y nm Alq₃/1 nm LiF/~100 nm Al OLEDs. **B)** Absorption spectra of P3HT as measured by the array shown in (A) and by a reference spectrophotometer. Reprinted with permission from reference 2, copyright 2011 American Institute of Physics. **C)** EL spectra of near UV-deep blue combinatorial 15 nm Al/5 nm MoO₃/20 nm TAPC/ x nm CBP/ y nm BPhen/1 nm LiF/~100 nm Al OLED array vs. the EL spectrum of a reference device with an ITO electrode and **D)** absorption spectra of an Alexa Fluor 405 film using a reference and the integrated OLED/OPD arrays. Reprinted with permission from reference 3, copyright 2015 WILEY-VCH Verlag GmbH & Co. KGaA, Weinheim.

The structure of the OLED pixels comprising the arrays was

15 nm Al/5 nm MoO₃/20 nm TAPC/ x nm CBP/ y nm BPhen/1 nm LiF/~100 nm Al

where $15 \leq x \leq 30$ nm and $25 \leq y \leq 40$ nm.

Figure 7C shows the EL spectra of the different OLED pixels in the near UV/deep blue array. As clearly seen, $\lambda_{\text{em,max}}$ increases from 370 nm to 430 nm as x and y increase. As in the case of the sky blue-to-red array above, the FWHM increases with $\lambda_{\text{em,max}}$. **Figure 7D** shows the absorption spectrum of an Alexa Fluor 405 film using this OLED array.³ As clearly seen, the data points obtained with the OLED/OPD arrays are in excellent agreement with the reference spectrum.

Medical Applications

Organic optoelectronic sensors have also found use in medical applications.^{4,5} **Figure 8A** shows an example of green and red printed polymer LEDs (PLEDs) that were used as light sources in reflection-mode pulse oximetry, together with a silicon photodiode for measuring blood oxygenation on the wrist.⁵ The device measures arterial oxygen saturation and heart rate.

In another report, a flexible (bending radius of ~100 μ m) ultrathin (3 μ m) reflective pulse oximeter and photo-plethysmograph (PPG) device was fabricated using OPD and PLEDs, including utilization of an on-skin digital display. In

a more recent example, a skin-conformal, near-IR, ultrathin (3 μ m thick) and ultra-flexible (bending radius of 3 μ m) OPD was demonstrated. The device maintained operational stability when flexed over 103 cycles. Additionally, fingerprint-conformal PPG sensing with fast response was demonstrated. These attributes enable its use as a cardiovascular sensor.

A recent report describes a flexible PPG sensor composed of flexible red OLEDs and OPDs that are highly sensitive to red EL.³⁴ The PPGs can be suitable for detection of various biological signals, and as an example of real-world application this flexible PPG was used to detect drowsiness, with performance similar to that of a conventional PPG sensor.

Other results have demonstrated the further potential of organic optoelectronic devices, which combine OLEDs and OPDs on flexible substrates, as low-cost, disposable, non-invasive optical sensors in medicine and sports. **Figures 8B and 8C** show an example of a wearable muscle contraction sensor.⁴ The application of this sensor, with a super yellow-based PLED that has a broad emission spectrum from 520 to 700 nm and a PTB7:PC₇₀BM OPD, was demonstrated by showing that it could be used to control a robotic arm that mimicked the movement of a real arm. In the second example, a wearable flexible organic optoelectronic bandage was used for measuring tissue oxygenation, enabling long-term monitoring.

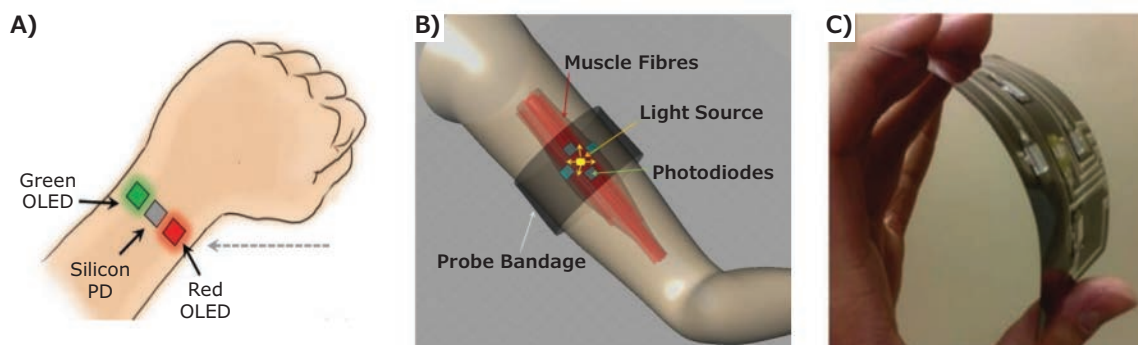


Figure 8. A) Schematics of a reflection-mode wrist pulse oximeter using green and red PLEDs as the light source together with a silicon PD. Reprinted with permission from reference 5, copyright 2017 John Wiley & Sons. B) Schematic principle of muscle contraction sensor showing an arm containing muscle fibers, and a probe bandage consisting of a light source and four photodiodes on top of the arm. C) Photograph of a thin flexible organic optoelectronic sensor. Reprinted with permission, copyright 2014 John Wiley & Sons.

Summary

The advantages of thin film-based devices, such as all-organic and hybrid optical, biological, and chemical sensors, are their small size (potential miniaturization), portability, and thus field-deployability. Moreover, flexible all-organic devices can be adapted as wearable/badge-size monitors for diagnostic and therapeutic medical applications.

Further, organic and hybrid perovskite electronic devices hold promise for optical, analytical, and medical applications due to their ease of fabrication, unique simplicity of integration of various thin-film components, and potential low cost. OLEDs, which are promising as efficient light sources in luminescent sensor (micro) arrays for multiple analyte detection, can be easily integrated with thin-film sensing probes, and with thin-film PDs, e.g., OPDs and potentially PPDs. Moreover, they are compatible with microfluidic architectures, and are often used in analytical applications.

OLEDs can be operated in a pulsed mode, which enables their use not only in the PL intensity I mode, but also in the PL decay-time t mode. This mode of operation eliminates the need for frequent sensor calibration and for optical filters. In improving the OLED sensing platform, standard bottom-emitting OLEDs were replaced by narrow-band μC OLED pixels, which are bright and efficient. Their narrower EL spectrum can be tailored to the absorption spectrum of sensing elements, significantly improving the sensor's performance. Importantly, a MC μC OLED array, in conjunction with suitable OPDs, can serve as a spectrometer on a chip. As shown, PPDs, though not yet fully tested in conjunction with OLEDs, hold much promise because of their strong sensitivity and fast response time.

The utilization of compact, light-weight, and low cost thin-film organic and hybrid optical platforms for analytical applications is expected to increase dramatically as devices improve and these technologies are adopted in other applications. This platform technology is expected to help address ongoing security and safety issues, detect explosives, and monitor food-borne pathogens.

Acknowledgements

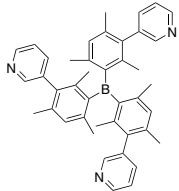
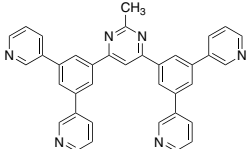
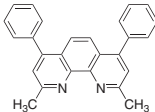
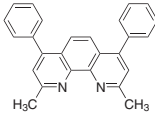
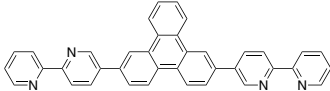
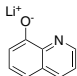
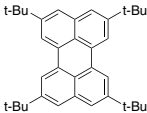
This work was supported in part by NSF grant ECCS 1608496. Ames Laboratory is operated by Iowa State University for the US Department of Energy (USDOE) under Contract No. DE-AC 02-07CH11358. The research was partially supported by Basic Energy Sciences, Division of Materials Science and Engineering, USDOE.

References

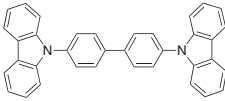
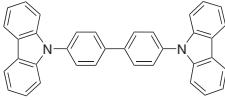
- (1) (a) Shinar, J.; Shinar, R. *J. Phys. D: Appl. Phys.* **2008**, *41*, 133001; (b) *Organic Electronics in Sensors and Biotechnology*, edited by R. Shinar and J. Shinar (McGraw Hill, NY) **2009**.
- (2) Liu, R.; Xu, C.; Biswas, R.; Shinar, J.; Shinar, R. *Appl. Phys. Lett.* **2011**, *99*, 093305.
- (3) Manna, E.; Fungura, F.; Biswas, R.; Shinar, J.; Shinar, R. *Adv. Funct. Mater.* **2015**, *25*, 1226–1232.
- (4) Bansal, A. K.; Hou, S.; Kulyk, O.; Bowman, E. M.; Samuel, I. D. W. *Adv. Mater.* **2015**, *27*, 7638–7644.
- (5) Han, D.; Khan, Y.; Ting, J.; King, S. M.; Yaacobi-Gross, N.; Humphries, M. J.; Newsome, C. J.; Arias, A. C. *Adv. Mater.* **2017**, *29*, 1606206.
- (6) Li, L.; Deng, Y.; Bao, C.; Fang, Y.; Wei, H.; Tang, S.; Zhang, F.; Huang, J. *Adv. Optical Mater.* **2017**, *5*, 1700672.
- (7) Xiao, X.; Bao, C.; Fang, Y.; Dai, J.; Ecker, B. R.; Wang, C.; Lin, Y.; Tang, S.; Liu, Y.; Deng, Y.; Zheng, X.; Gao, Y.; Zeng, X.C.; Huang, J. *Adv. Mater.* **2018**, *30*, 1705176.
- (8) Liu, R.; Xiao, T.; Cui, W.; Shinar, J.; Shinar, R. *Anal. Chim. Acta* **2013**, *778*, 70.
- (9) Liu, R.; Ye, Z.; Park, J.-M.; Cai, M.; Chen, Y.; Ho, K.-M.; Shinar, R.; Shinar, J. *Opt. Exp.* **2011**, *19* (S6), A1272.
- (10) Cai, Y.; Shinar, R.; Zhou, Z.; Qian, C.; Shinar, J. *Sensors & Actuators B* **2008**, *134*, 727.
- (11) Vengasandra, S.; Cai, Y.; Grewell, D.; Shinar, J.; Shinar, R. *Lab on a Chip* **2010**, *10*, 1051.
- (12) Duffy, D. C.; Gillis, H. L.; Lin, J.; Sheppard, N. F.; Kellog, G. J. *Anal. Chem.* **1999**, *71*, 4669.
- (13) Zhang, J.; Guo, Q.; Liu, M.; Yang, J. J. *Micromech. Microeng.* **2008**, *18*, 125025.
- (14) Watts, A. S.; Urbas, A. A.; Moschou, E.; Gavalas, V. G.; Zoval, J. V.; Madou, M.; Bachas, L. G. *Anal. Chem.* **2007**, *79*, 8046.
- (15) Nolte, D. D. *Rev. Sci. Instrum.* **2009**, *80*, 101101.
- (16) Ghosh, D.; Shinar, R.; Dalal, V.; Zhou, Z.; Shinar, J. *J. Non-Crystalline Sol.* **2008**, *354*, 2606.
- (17) Nalwa, K. S.; Cai, Y.; Thoeming, A. L.; Shinar, J.; Shinar, R.; Chaudhary, S. *Adv. Mater.* **2010**, *22*, 4157.
- (18) Zhou, Z.; Shinar, R.; Allison, A.J.; Shinar, J. *Adv. Funct. Mat.* **2007**, *17*, 3530.
- (19) Carraway, E. R.; Demas, J. N.; DeGraff, B. A.; Bacon, J. R. *Anal. Chem.* **1991**, *63*, 337–342.
- (20) Cui, W.; Liu, R.; Manna, E.; Park, J.-M.; Fungura, F.; Shinar, J.; Shinar, R. *Anal. Chim. Acta* **2014**, *853*, 563–571.
- (21) Tam, H. L.; Choi, W. H.; Zhu, F. *Electronics* **2015**, *4*, 623–632.
- (22) Benavides, C. M.; Murto, P.; Chochos, C. L.; Gregoriou, V. G.; Avgeropoulos, A.; Xu, X.; Bini, K.; Sharma, A.; Andersson, M. R.; Schmidt, O.; Brabec, C. J.; Wang, E.; Tedde, S. F. *ACS Appl. Mater. & Interfaces* **2018**, *10*, 12937–12946.

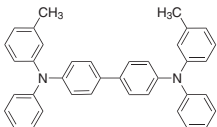
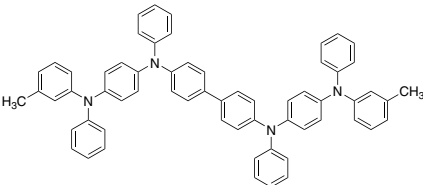
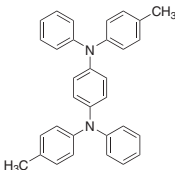
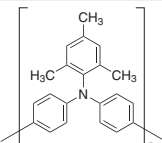
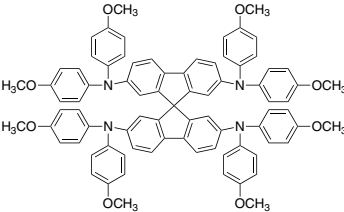
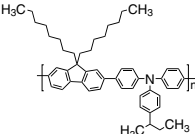
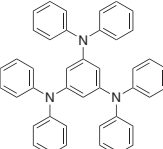
- (23) Wang, W.; Zhang, F.; Du, M.; Li, L.; Zhang, M.; Wang, K.; Wang, Y.; Hu, B.; Fang, Y.; Huang, J. *Nano Lett.* **2017**, *17*, 1995–2002.
- (24) Jang, M. S.; Yoon, S.; Sim, K. M.; Cho, J.; Chung, D. S. *J. Phys. Chem. Lett.* **2018**, *9*, 8–12.
- (25) Manna, E.; Xiao, T.; Shinar, J.; Shinar, R. *Electronics* **2015**, *4*, 688.
- (26) Shen, L.; Fang, Y.; Wang, D.; Bai, Y.; Deng, Y.; Wang, M.; Lu, Y.; Huang, J. *Adv. Mater.* **2016**, *28*, 10794.
- (27) Ahmadi, M.; Wu, T.; Hu, B. *Adv. Mater.* **2017**, *29*, 1605242.
- (28) Li, L.; Deng, Y.; Bao, C.; Fang, Y.; Wei, H.; Tang, S.; Zhang, F.; Huang, J. *Adv. Opt. Mater.* **2017**, *5*, 1700672.
- (29) Xun Xiao and Jinsong Huang, unpublished results.
- (30) Li, Y. Q.; Tang, J. X.; Xie, Z. Y.; Hung, L. S.; Lau, S. S. *Chem. Phys. Lett.* **2004**, *386*, 128.
- (31) Burrows, P. E.; Khalfin, V.; Gu, G.; Forrest, S. R. *Appl. Phys. Lett.* **1998**, *73*, 435.
- (32) Greiner, M. T.; Helander, M. G.; Wang, Z. B. *Appl. Phys. Lett.* **2010**, *96*, 213302.
- (33) Irfan, H. D.; Gao, Y. *Appl. Phys. Lett.* **2010**, *96*, 243307.
- (34) Ryu, G.-S.; You, J.; Kostianovskii, V.; Lee, E.-B.; Kim, Y.; Park, C.; Noh, Y.-Y. *IEEE Trans. Electr. Dev.* **2018**, *65*, 2997–3004.
- (35) Yokota, T.; Zalar, P.; Kaltenbrunner, M.; Jinno, H.; Matsuhisa, N.; Kitanosako, H.; Tachibana, Y.; Yukita, W.; Koizumi, M.; Someya, T. *Sci. Adv.* **2016**, *2*, e1501856.
- (36) Park, S.; Fukuda, K.; Wang, M.; Lee, C.; Yokota, T.; Jin, H.; Jinno, H.; Kimura, H.; Zalar, P.; Matsuhisa, N.; Umez, S.; Bazan, G. C.; Someya, T. *Adv. Mater.* **2018**, 1802359.

Electron Transport and Hole Blocking Material

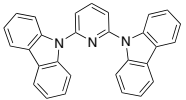
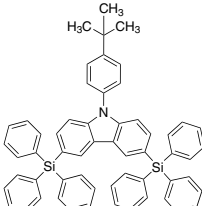
Name	Structure	Purity/Molecular Weight	Cat. No.
3TPYMB		≥98	900953-500MG 900953-100MG
B3PYMPM		≥99% (sublimed)	900958-100MG 900958-500MG
Bathocuproine		96%	140910-500MG 140910-1G
Bathocuproine		99.99% trace metals basis	699152-500MG 699152-5G
BPy-TP2		≥99% (sublimed)	900939-100MG 900939-500MG
Liq		>99.5%, HPLC (sublimed)	900928-1G
TBPe		99%, HPLC (sublimed)	900937-250MG

Hole Transport Material

Name	Structure	Purity/Molecular Weight	Cat. No.
4,4'-Bis(N-carbazolyl)-1,1'-biphenyl		97%	660124-1G 660124-5G
4,4'-Bis(N-carbazolyl)-1,1'-biphenyl		99.9% trace metals basis	699195-1G 699195-5G

Name	Structure	Purity/Molecular Weight	Cat. No.
N,N'-Bis(3-methylphenyl)-N,N'-diphenylbenzidine		99%	443263-1G 443263-5G
N,N'-Diphenyl-N,N'-bis-[4-(phenyl-m-tolylamino)phenyl]biphenyl-4,4'-diamine		95%	900968-250MG
N,N'-Diphenyl-N,N'-di-p-tolylbenzene-1,4-diamine		—	663263-1G 663263-5G
PTAA		average M_n 7,000–10,000 (GPC)	702471-100MG 702471-1G
Spiro-MeOTAD		99%, HPLC	792071-1G 792071-5G
TFB		average M_w >30,000 by GPC	901101-1G 901101-250MG
1,3,5-Tris(diphenylamino)benzene		97%	663247-5G 663247-10G

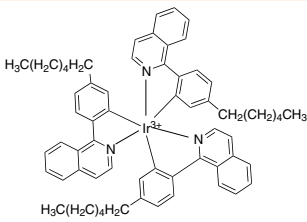
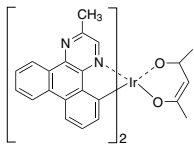
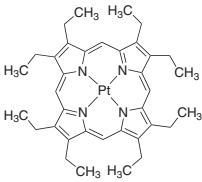
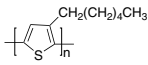
Host Material

Name	Structure	Purity/Molecular Weight	Cat. No.
2,6-Bis(9H-carbazol-9-yl)pyridine		≥98%	900922-500MG
CzSi		≥97%	900965-500MG

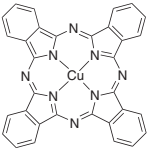
Name	Structure	Purity/Molecular Weight	Cat. No.
DPTPCz		≥97%	900964-500MG
PFN-DOF		M_w 5,000–10,000	900954-250MG 900954-1G
PFN-DOF		M_w >10,000	900966-250MG 900966-1G
9-Phenyl-9'-(triphenylsilyl)-3,3'-bicarbazole		≥97%	900963-250MG
PPT		—	901102-250MG 901102-1G
SPPO13		≥99%, HPLC	900977-500MG 900977-100MG
TCPZ		—	900969-500MG

Light Emitters and Dopants

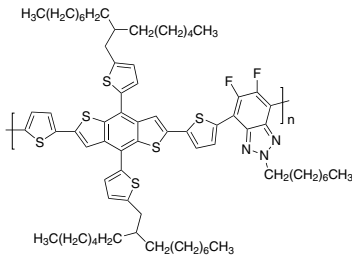
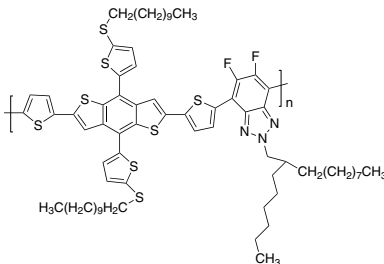
Name	Structure	Purity/Molecular Weight	Cat. No.
Bepp2		99% (sublimed)	900959-500MG 900959-100MG
DMAC-DPS		≥99%, HPLC (Sublimed)	900940-1G 900940-250MG
F8BT		average M_w >20,000	900979-250MG
FIr6		98%	901106-100MG

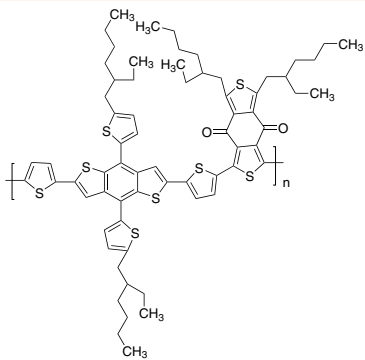
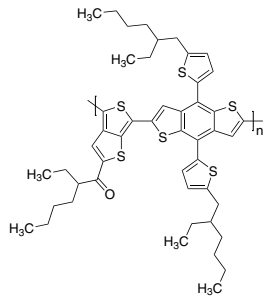
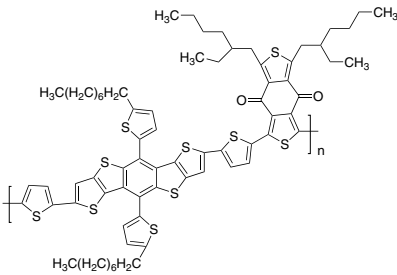
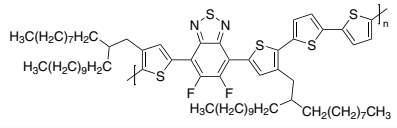
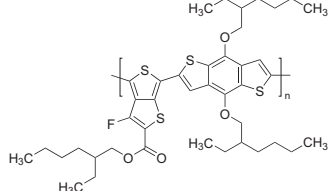
Name	Structure	Purity/Molecular Weight	Cat. No.
Hex-Ir(piq)3		≥99%	901104-100MG
Ir(MDQ) ₂ (acac)		—	901074-100MG 901074-500MG
Platinum octaethylporphyrin		95%	673625-100MG
Poly(3-hexylthiophene-2,5-diyl)		average M _w 85,000–100,000	900549-1G
Red light-emitting spiro-copolymer		average M _w 720,000	900446-250MG

Dye

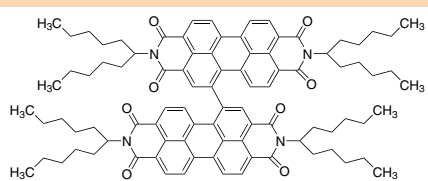
Structure	Name	Purity / Dye Content	Absorption	Cat. No.
	Copper(II) phthalocyanine	Dye content 99%, sublimed grade	λ _{max} 678 nm	546674-1G 546674-5G
	Copper(II) phthalocyanine	Dye content >99%	λ _{max} 678 nm	546682-200MG 546682-2G
	Copper(II) phthalocyanine	Dye content 90%	λ _{max} 678 nm	252980-5G 252980-25G 252980-100G
	Copper(II) phthalocyanine	>99.95% trace metals basis, triple-sublimed grade	λ _{max} 678 nm	702854-500MG

Donor Material

Name	Structure	Molecular Weight	Cat. No.
J51		M _w 40,000–80,000 by GPC (PS standard)	901058-100MG
J61		M _w 50,000–100,000 by GPC (PS standard)	901045-100MG

Name	Structure	Molecular Weight	Cat. No.
PBDB-T		$M_w > 50,000$ by GPC (GPC standard: PS)	901099-100MG
PBDTTT-C-T		M_w 80,000–150,000 (GPC, PS standard)	901067-100MG
PDBT-T1		M_w 20,000–50,000 (GPC, PS standard)	901097-100MG
PfFBT4T-C9C13		M_w 35,000–100,000	900980-100MG
PTB7		average M_w 80,000–200,000	772410-100MG

Non-Fullerene Acceptor Material

Name	Structure	Purity/Molecular Weight	Cat. No.
Di-PDI		$\geq 97\%$	900774-100MG

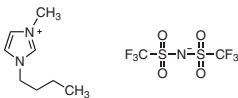
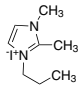
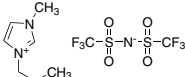
Name	Structure	Purity/Molecular Weight	Cat. No.
EH-IDTBR		97%	900853-100MG 900853-50MG
FBR		≥97%	900854-100MG 900854-50MG
Hexyl N-annulated perylene diimide		—	901144-500MG
O-IDTBR		99%	900810-50MG 900810-100MG
ITIC		99%	900799-50MG 900799-100MG
ITIC-F		97%	901423-100MG
ITIC-DM		99%	900803-100MG 900803-50MG
ITIC-Th		99%	900800-50MG 900800-100MG

Name	Structure	Purity/Molecular Weight	Cat. No.
N2300		average M_n 25–50 kDa	900962-500MG 900962-100MG
P(NDI2OD-T2)		average M_n 50–100 kDa	900961-100MG 900961-500MG
SF-PDI		99%	900782-100MG
TPDI-Hex		—	901146-250MG

Acceptor Material

Structure	Name	Purity (%)	Cat. No.
	4-(1',5'-Dihydro-1'-methyl-2'H-[5,6]fullereno-C ₆₀ -I _h -[1,9-c]pyrrol-2'-yl)benzoic acid	>99, NMR	802832-100MG
	ICBA	99, HPLC	753955-250MG
	[6,6]-Phenyl C ₆₁ butyric acid methyl ester	>99.9	684457-100MG
	[6,6]-Phenyl C ₆₁ butyric acid methyl ester	>99.5	684449-100MG 684449-500MG
	[6,6]-Phenyl C ₆₁ butyric acid methyl ester	>99	684430-1G
	Small gap fullerene-ethyl nipecotate	≥95, fullerenes 50%	707473-250MG

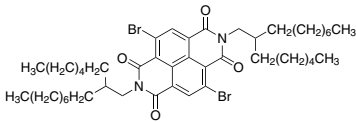
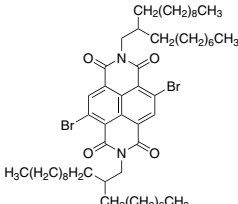
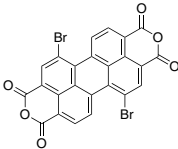
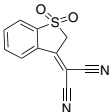
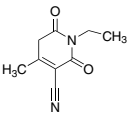
High Purity Electronic Grade Electrolyte

Name	Structure	Purity	Cat. No.
1-Butyl-3-methylimidazolium bis(trifluoromethylsulfonyl)imide Solarpur®		≥99.5%, HPLC	901041-25G
1-Propyl-2,3-dimethyl-imidazolium iodide Solarpur®		≥99.0%, HPLC	901016-25G
1-Propyl-3-methyl-imidazolium bis(trifluoromethylsulfonyl)imide Solarpur®		≥99.0%, HPLC	901024-25G

Perovskite Precursor Solution

Name	Composition	Form/Concentration	Cat. No.
Methylammonium bromide solution	—	0.18 M in 2-propanol	808407-50ML
Methylammonium iodide	CH ₃ NH ₂ • HI; CH ₃ IN	powder	793493-5G
	—	0.42 M in 2-propanol	808431-50ML
Methylammonium triiodoplumbate(II) precursor solution	[CH ₃ NH ₃] ⁺ [PbI ₃] ⁻ ; CH ₃ I ₃ Npb	solution, 40 wt. % in DMF	793833-5ML

Intermediate

Name	Structure	Purity	Cat. No.
4,9-Dibromo-2,7-bis(2-hexyldecyl)benzo[Imn][3,8]phenanthroline-1,3,6,8(2H,7H)-tetrone		97%	901040-500MG
4,9-Dibromo-2,7-bis(2-octyldodecyl)benzo[Imn][3,8]phenanthroline-1,3,6,8(2H,7H)-tetrone		>99%, HPLC	901013-500MG
1,7-Dibromo-3,4,9,10-tetracarboxylic acid dianhydride		98%	900186-1G
2-(1,1-Dioxidobenzo[b]thien-3(2H)-ylidene)propanedinitrile		95%	900805-500MG
1-Ethyl-1,2,5,6-tetrahydro-4-methyl-2,6-dioxo-3-pyridinecarbonitrile		>98%	900752-1G

Make it Bright.



livilux® Organic Light Emitting Diode (OLED) materials are a unique portfolio of premium materials for OLEDs, from well-established materials to cutting-edge innovations.

Key Features:

- Solution processibility
- Excellent reproducibility
- High efficiency
- Low operation voltage
- Long lifetime

The following livilux® OLED materials are now available at **SigmaAldrich.com**

Name	Description	Cat. No.
PDY-132	Super yellow light-emitting PPV copolymer	900438
PDO-123	Orange light-emitting PPV copolymer	900440
SPG-01T	Green light-emitting spiro-copolymer	900441
SPR-001	Red light-emitting spiro-copolymer, average M_w 180,000	900444
	Red light-emitting spiro-copolymer, average M_w 470,000	900447
	Red light-emitting spiro-copolymer, average M_w 720,000	900446

To find out more about these products and our other OLED materials, visit SigmaAldrich.com/oled

The life science business of Merck operates as MilliporeSigma in the U.S. and Canada.

Properties and Applications of Functionalized Graphene Oxide



Reza Hajian,¹ Kandace Fung,^{1,2} Peichi Peggy Chou,^{1,3} Sike Wang,^{1,2} Sarah Balderston,¹ Kiana Aran^{1*}

¹Claremont University, Keck Graduate Institute, School of Applied Life Sciences Claremont, CA 91711, USA

²Keck Science Department, Claremont McKenna College, Claremont, CA, 91711, USA

³Keck Science Department, Pitzer College, Claremont, CA, 91711, USA

*E-mail: Kiana_Aran@kgi.edu

Introduction

The growing interest in the development of new types of implantable and wearable electrochemical sensors for use in medical applications has helped to drive the development of graphene and other new materials. Graphene, discovered in 2004, is a carbon-based nanomaterial that takes the form of an sp² carbon sheet, with the atoms arranged in a honeycomb lattice.^{1,2} It has high intrinsic mobility, unrivaled malleability and impermeability, high theoretical specific surface area (2630 m²/g for a single layer), and remarkable electron transport capabilities. Because of the properties imparted by its 2D structure, graphene becomes highly sensitive and selective when functionalized with a linker molecule, making it a promising candidate for a multitude of biosensing applications.³⁻⁵

Graphene can take many forms, each with its own characteristics: few-layer graphene (FLG),⁶ multi-layer graphene (MLG),⁷ graphene nanoplatelets (GNP),⁸ graphene oxide (GO),¹⁰⁻¹² and reduced graphene oxide (rGO).⁹ FLG is used in sensors, batteries, and nanoelectronics devices, while both MLG and GNP are known for their applications as conductive inks, plastics additives, and lubricants. rGO is similar to GO, but it possesses a reduced oxygen-carbon ratio making it especially suitable for various chemical and biosensing applications.

Graphene oxide is usually produced by the Hummers method,¹⁰ which is easy and inexpensive. GO continues to generate high levels of interest among nanomaterials researchers because of its high conductivity after reduction, selectivity after functionalization, and sensitivity. This review focuses on GO, its functionalization methods, and its many applications.

Graphene oxide is comprised of a single layer graphene sheet, covalently bonded to oxygen functional groups on the basal planes and edges of the sheet. On the basal planes, there are both hydroxyl and epoxy groups; the edges can include carboxyl, carbonyl, phenol, lactone, and quinone groups.¹¹⁻¹⁴ These oxygenated functional groups bind covalently with the carbon atoms in GO, creating oxidized regions of sp³-hybridized carbon atoms that disrupt the non-oxidized regions of the original sp² honeycomb network. Graphene sheets alone have limited solubility in water due to the strong π - π bonds between layers, so GO or rGO are usually used for biosensing applications.¹⁵ The functional groups present on GO are polar, making it very hydrophilic and water-soluble, which is important for processing and chemical derivatization. On the other hand, these oxygen-based functional groups can degrade the electronic, mechanical, and electrochemical properties of GO by creating significant structural defects, reducing electrical conductivity, and potentially limiting its direct application in electrically active materials and devices. However, GO can instead be functionalized by partially reducing it to rGO with various chemical or thermal treatments,¹⁵ in order to facilitate the transport of carriers.¹⁶ This chemical modification decreases its resistance by several orders of magnitude¹⁷ and transforms the material into a graphene-like, semiconducting material.

Chemical functionalization is an easy way to modify GO, and has proven extremely useful for creating sensors for biomedical, electrochemical, and diagnostic applications. The reactive and modifiable oxygenated functional groups of GO can be functionalized with different electroactive species.¹⁸ This covalent functionalization of specific molecules can mitigate the non-specific binding that typically occurs with plain graphene

sensors. Many methods have been developed to minimize the disadvantages of GO while enhancing the advantages of graphene qualities.¹ For example, covalently bonding different chemical linkers to GO can modify the surface of the graphene and fine-tune its properties. Careful functionalization of GO increases its conductivity, stability, and selectivity for electrochemical sensing applications,^{1,2,18} as well as enhancing its sensitivity by increasing the surface area.

Applications of Functionalized Graphene Oxide

Graphene Oxide Applications Using Hydroxyl (OH) Functionalization

Hydroxyl groups attached to the basal planes of GO sheets can be effective attachment sites for different chemical agents. For example, the surface can be modified by silanization, a process that coats a surface with organofunctional alkoxy silane molecules. This modification technique has been shown to produce carbon nanomaterials with optimal chemical and physical properties for fabricating conducting films.^{19–21}

Designing nanomaterials that have strong metal adsorption and antimicrobial capabilities for environmental,^{23,24} catalytic,^{25–27} and biomedical applications²⁸ has posed a challenge. In 2014, Carpio et al. conducted experiments on GO functionalization using ethylenediamine triacetic acid (EDTA), a strong chelating agent, to enhance the multi-functionality of GO, thus increasing its metal adsorption and antimicrobial properties.²² In this study, GO was functionalized with *N*-(trimethoxysilylpropyl) ethylenediamine triacetic acid (EDTA-silane). In a dehydration-condensation reaction, the hydrolysis of the trialkoxy groups in Si-EDTA creates -Si-OH groups that interact with the hydroxyl groups (OH-C) to form Si-O-C bonds. When compared to GO, GO-EDTA demonstrates improved antimicrobial characteristics

with a 10.1% and 7.1% increase in cell inactivation of *B. subtilis* (Gram-positive) and *C. metallidurans* (Gram-negative), respectively. GO-EDTA also demonstrates maximum adsorption capacities for Cu²⁺ and Pb²⁺ that exceeds the capacities of traditional adsorbent materials. In addition, after 24-hour exposure to human corneal epithelial cell lines, GO-EDTA shows minimal toxicity on human cells, as 99% of the cell culture remained viable. This makes GO-EDTA a promising carbon nanomaterial for future clinical applications.

Another study used EDTA to functionalize rGO, by creating a rGO-EDTA composite suspended in Nafion-ethanol solution.²⁹ The rGO-EDTA/Nafion film was then deposited onto a glassy carbon (GC) electrode, and this rGO-EDTA device could detect dopamine (DA) via oxidation.

Hu et al. investigated silanization, reduction, silanization combined with reduction, and *in situ* co-polymerization as methods for functionalizing GO, in order to improve tensile strength and solubility.³⁰ The hydroxyl groups on graphene oxide and rGO sheets were silanized with 3-methacryloxypropyltrimethoxysilane (MPS, **Cat. No. 440159**)³⁴ (Figure 1). Water suspension tests for GO, rGO, MPS-GO, and MPS-rGO revealed that MPS-GO and MPS-rGO had enhanced water solubility. Hu et al. then functionalized GO and rGO derivatives with poly(methyl methacrylate) (Cat. Nos. **182230**, **200336**, **445746**, and **182265**, PMMA) via *in situ* co-polymerization in order to increase the mechanical properties of the polymer. The MPS-rGO/PMMA composites had 30% more tensile strength when compared to pristine PMMA due to the stable dispersion of the nanosheets in the polymer matrix that increased the interfacial strength indicating potential for future industrial applications.³⁰

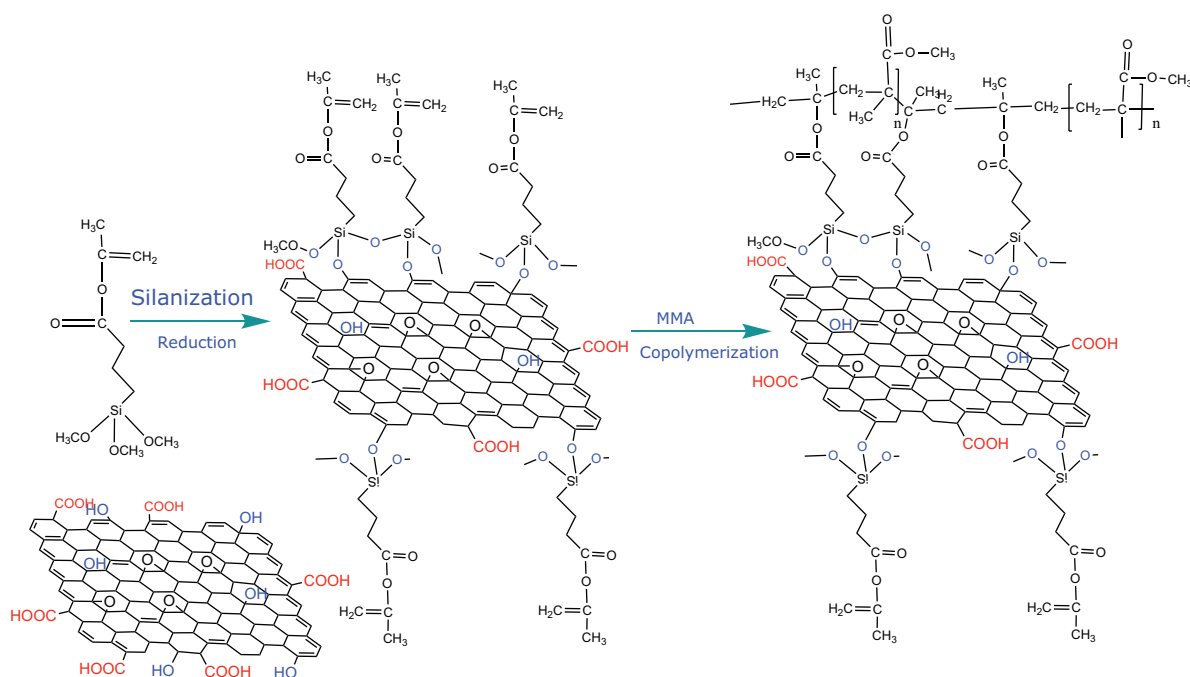


Figure 1. Silanization of GO using MPS, following co-polymerization of functionalized, silanized-GO with PMMA. Reproduced with permission from reference 30, copyright 2014 Elsevier.

Instead of silanization, hydroxyl groups on GO can also be functionalized by esterification. In one study, this functionalization occurred through a reaction with nitriles and then separation of the products through filtration and/or centrifugation.³¹ Yuan et al. demonstrated that GO functionalized with poly(L-lactic) acid (Cat. Nos. **764590**, **764698**, **765112**, **900295**, etc., PLLA) improved its properties including tensile strength, tensile fracture strength, and dispersibility.³²

In 2010, GO was functionalized via esterification to synthesize a GO framework for gas adsorption.³³ The researchers combined GO with benzene-1,4-diboronic acid (B14DBA, Cat. No. **417130**) to form boronic esters (Figure 2). In this case, single layer GO sheets were crosslinked together, building a 3D porous network connected by benzenediboronic acid pillars. The framework structures had modifiable pore widths, volumes, and binding sites, making them extremely useful for gas storage.

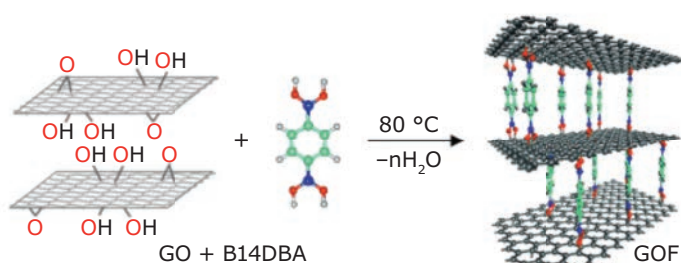


Figure 2. GO sheets functionalized with B14DBA via covalent bonding of -OH groups to create GOF. Reproduced with permission from reference 33, copyright 2010 John Wiley and Sons.

Graphene Oxide Applications Using Epoxy Group Functionalization

Covalent functionalization of graphene oxide through modification of epoxy groups on the basal planes usually involves a nucleophilic attack at the α -carbon of the epoxide, and using an amine group to catalyze the ring-opening reaction. For example, in 2008 Wang et al. used octadecylamine (ODA, Cat. No. **74750**) as the nucleophile, thus opening the rings and creating polydispersed, chemically converted graphene oxide sheets (p-CCG).³⁴ This method produced GO as colloidal suspensions in organic solvents that could then be spin-coated, printed onto various substrates, or fully reduced into high quality chemically modified graphene (CMG) films. These new properties make p-CCGs highly promising starting material for electrochemical sensors.

A similar study was conducted by Yang et al. using 1-(3-aminopropyl)-3-methylimidazolium bromide (R-NH₂), an ionic liquid, to functionalize GO by the same ring-opening mechanism (Figure 3).³⁵ The p-CCGs produced had excellent

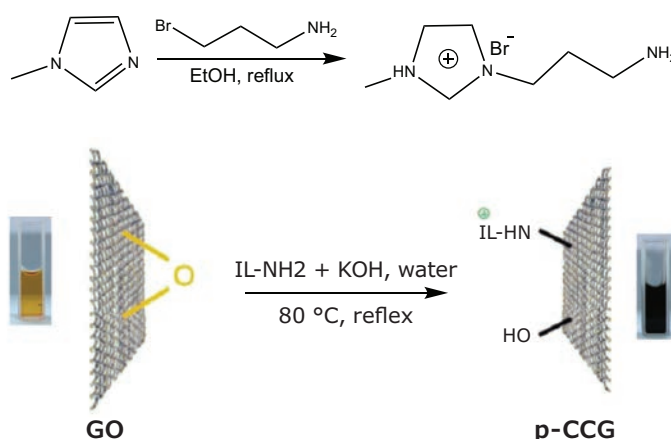


Figure 3. GO functionalized to prepare p-CCG. Reproduced with permission from reference 35, copyright 2009 Royal Society of Chemistry.

solution-stability in polar solvents.³⁵ Likewise, these p-CCGs demonstrate potential for electrochemical applications, for example for chemically-modified electrodes.

In 2015, Bandyopadhyaya et al. synthesized hexylamine-functionalized rGO (rGO-HA)³⁶ by a nucleophilic addition of the HA amine groups onto the GO epoxy groups. Hydrazine hydrate (Cat. Nos. **18412**, **225819**) was then added to reduce the composite to the final rGO-HA product. This alkylamine functionalization resulted in the enhanced hydrophobicity of the rGO-HA sheets and allowed them to be well-dispersed in various organic solvents. The permeability of hydrogen gas into a synthesized rGO-HA film after coating on the surface of polyurethane (PU) decreased, suggesting a potential use in industrial hydrogen gas separation and purification.³⁶

Another group used 3-aminopropyltriethoxysilane (APTS, Cat. No. **440140**) to functionalize graphene oxide platelets via an S_N2 reaction between the epoxide and APTS amine groups.³⁷ The researchers were able to synthesize polydispersed, functionalized, and chemically converted graphene (f-CCG) that was soluble in many polar media. Due to its increased strength, the functionalized-GO product has applications as both bio-encapsulation and sensors, among other uses.

Shams et al. synthesized a nanocomposite of GO and ethylenediamine (EDA, Cat. No. **E26266**) under reflux at 50 °C for use as an electrochemical sensor to detect fenitrothion in natural water.³⁸ In addition, EDA was used to crosslink GO and gold nanoparticles (AuNPs) in order to increase the hydrophilicity and dispersibility of GO in polar solvents with a decreased tendency to aggregate.¹

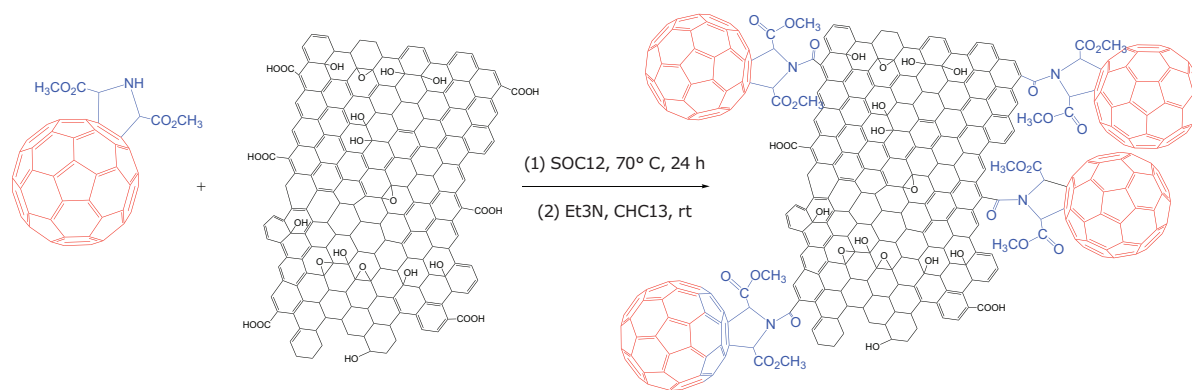


Figure 4. Scheme of fullerene functionalizing GO via ester linkages. Reproduced with permission from the corresponding author.³⁹

Applications of Graphene Oxide Using Carboxylic Group Functionalization

Similar to hydroxyl and epoxy groups, carboxyl groups can be functionalized through activation and amidation or esterification with small molecules or polymer chemical linkers.^{40–43} In one study, graphene oxide was activated with *N,N'*-Dicyclohexylcarbodiimide (DCC, **Cat. No. D80002**) and coupled with an esterification reaction using an allotropic carbon nanomaterial, fullerene (C_{60} , **Cat. No. 379646**).⁵⁸ Like other allotropic carbon nanomaterials, C_{60} possesses superconductivity, photoconductivity, and nonlinear optical (NLO) properties. In another study, Zhang et al. synthesized a graphene- C_{60} hybrid and investigated the NLO properties of this hybrid.³⁹ They found that the hydroxyl groups of fullerene formed covalent ester bonds with the carboxylic groups on GO (**Figure 4**). Liu et al. also reported GO functionalization with another allotropic carbon material, porphyrin (TPP- NH_2). In this case, the carboxylic groups of GO bonded to the amine group on TPP- NH_2 via activation coupled with amidation instead of esterification.⁴⁴ The GO-hybrids exhibited great potential for application as optical limiting and optical switching materials for optoelectronic and photonic devices.

Su et al. described a method of fabricating diamine-functionalized GO films through covalent bonding with the -COOH groups on the GO sheets.⁴⁵ Using a well-established procedure, *N*-(3-dimethylaminopropyl)-*N'*-ethylcarbodiimide hydrochloride (EDC, **Cat. No. 03449**) and *N*-hydroxysuccinimide (NHS, **Cat. No. 130672**) served as coupling reagents.⁴⁵ Novel impedance-type humidity sensors were made by coating diamine-functionalized GO films onto alumina or plastic substrates. These sensors, comprised from the diamine-functionalized GO film, worked across a wide humidity range, and exhibited a high sensitivity, high flexibility, high long-term stability, satisfactory linearity, a small hysteresis, a short response/recovery time, and only a weak dependence on temperature.

Other studies of esterification include grafting epoxy chains onto graphene oxide sheets via ester linkages with the carboxyl groups on GO, which can enhance the mechanical and thermal properties of graphene oxide while also increasing interfacial interactions.⁶³ This type of functionalized GO also can be used to create polymer solar cells (PSCs).

Cesium-neutralized GO (GO-Cs) has been used to transform GO into an electron extraction layer (EEL) in polymer solar cells (PSC).⁴⁶ Cesium carbonate (Cs_2CO_3 , **Cat. Nos. 202126, 441902, 554855, 255645**) was introduced to GO, resulting in neutralization of the -COOH groups to -COOCs groups. This product demonstrated promise as an excellent electron-extraction layer in solar cell devices.

Graphene oxide has also been functionalized with biomolecules. For example, in 2010, Shen et al. functionalized GO with bovine serum albumin (BSA) via diimide-activated amidation, a popular method for connecting proteins to other materials.⁴⁷ This process resulted in a GO-BSA conjugate, with no evidence of protein denaturation. Cyclic voltammogram (CV) measurements indicated that the conjugate maintained bioactivity and exhibited excellent water solubility, making it suitable for interaction with biological substrates.

The application of GO as a biosensor for clinical diagnosis was investigated by functionalizing carboxylic groups of GO with glucose oxidase (GOx), thus producing a biocompatible GO-GOx biosensor.⁵³ In this study, a cell line derived from human retinal pigment epithelium (RPE), a neuroectodermal derivative that is vital for photoreceptor survival, was introduced onto GO-GOx. The complex demonstrated excellent biocompatibility. The GO-based glucose biosensors exhibited a broad linear range, good stability, high sensitivity, excellent reproducibility, and great biocompatibility to human RPE cells, suggesting that these biosensors have tremendous potential for use in *in vivo* clinical diagnostics, such as diabetic retinopathy. The functionalization of GO's carboxyl groups also demonstrated GO's promise in creating enzyme electrodes that can be used in biomedicine and clinical diagnostics.

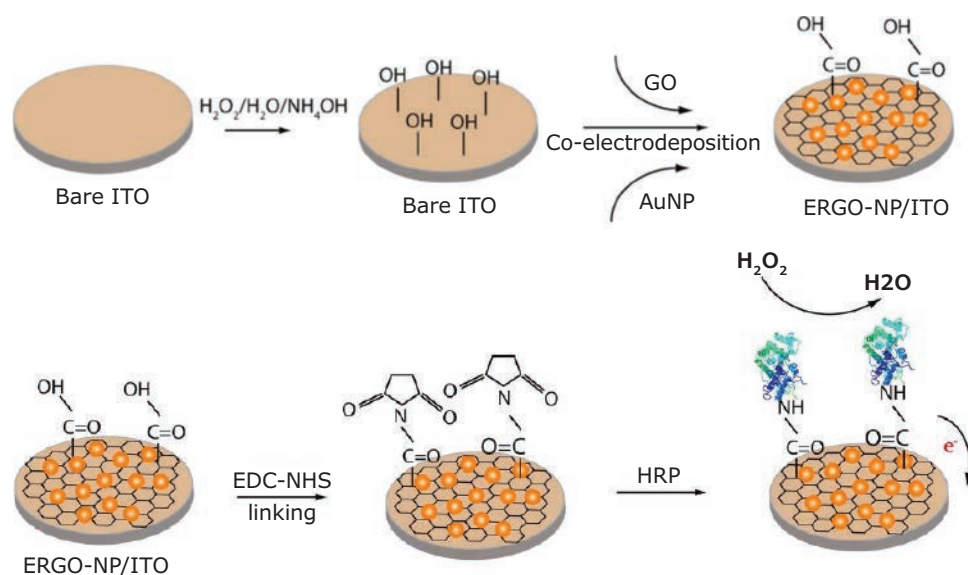


Figure 5. Schematic diagram depicting the surface functionalization of the formation of the HRP/ERGO-NP/ITO modified electrode applied for detection of H_2O_2 . Reproduced with permission from reference 48, copyright 2014 Electrochemical Society.

Yagati et al. reported an electrochemical sensor based on electrochemical co-reduction of graphene oxide/nanoparticle (ERGO-NP) composite films by the chronoamperometry method on indium tin oxide (ITO) electrodes, which was then utilized to sense H_2O_2 by direct electron transfer by horseradish peroxidase (HRP).⁴⁸ Covalent bonding between the amine groups of the enzyme and the carboxylate terminal of rGO and nanoparticles activated with 3-mercaptopropionic acid (**Cat. No. M5801**) was achieved through EDC/NHS coupling, leading to the formation of strong amide bonds (**Figure 5**).

In another study, graphene oxide was functionalized by the coupled reactions of EDC activation and polyethylene glycol (PEG) amidation.⁴⁹ The PEG-GO nanosheet products had excellent aqueous solubility and stability in biological solutions, including serum. Liu et al. then used the functionalized GO derivative to create a complex with various insoluble, aromatic camptothecin analogues, showing the potential of functionalized GO to deliver water-insoluble cancer drugs.

In 2008, Mohante and Berry investigated two approaches for covalent functionalization of GO via activation coupled with amidation. The resulting chemically modified graphene (CMG) demonstrated potential application in improving the nano/bio interface for biodetection, bioactuation, and diagnostics.⁵⁰ Electrical characterization of the GO-derivatives showed that the graphene-DNA (G-DNA) hybrid had a 128% increase in conductivity due to DNA's negative charge on the p-type GO, while the hybridization of G-DNA with cDNA generated approximately a single quantum of conducting hole, increasing conductivity by 71%.⁵¹

In another study, Liu et al. investigated the possibilities of functionalized GO as a selective and sensitive hybridized DNA biosensor.⁴³ GO was activated with EDC/sulfo-NHS, using similar chemistry to EDC/NHS described above, which converts the

carboxylic groups of GO into their amine-reactive NHS-ester forms. The functionalized carboxylic groups bound to amino-modified ssDNA, which allowed a complementary ssDNA labeled with gold nanoparticles (AuNPs) to attach to the GO-DNA probe in a hybridization reaction.

Applications of Graphene Oxide Using π - π Stacking Functionalization

The excellent adsorption of organic aromatic molecules on GO nanosheets can be attributed to both π - π stacking and hydrophobic interactions between GO and other aromatic molecules. In the past, studies have shown that the incorporation of sulfonic acid onto the surface of GO sheets can significantly increase its proton conductivity.⁵²⁻⁵⁴ Su et al. used 3,4,9,10-perylenetetracarboxylic diimide bis-benzene sulfonic acid (PDI), a large planar aromatic electron acceptor, and pyrene-1-sulfonic acid (PyS), a larger, planar aromatic electronic donor, to non-covalently functionalize rGO.⁵⁵ PyS and PDI molecules with negative charges were able to strongly affix onto the hydrophobic surface of graphene sheets via π - π interactions, without disrupting its electronic conjugation. This produced rGO-based composites with modifiable electronic properties that could be utilized to produce electronic devices.

In order to prepare water soluble CMG sheets for excellent stable-dispersion in polar solvents with enhanced conductivity, GO was reduced and at the same time non-covalently functionalized with 1-pyrenebutyrate (PB^-), also using π - π interactions.¹⁹ Here, PB^- acted as a stabilizer during the transformation of GO to rGO, as the aromatic pyrene undergoes π - π stacking with the basal plane of rGO. The resulted rGO- PB^- was able to form homogenous dispersion in water, and films cast from this dispersion were seven times more conductive than that from non-functionalized GO dispersions.

In order to take advantage of the selectivity and sensitivity of GO-based biosensors, Lu et al. non-covalently functionalized GO with aromatic compounds and nucleobases, resulting in a GO platform that could detect both DNA and proteins.⁵⁶ Immobilizing the dye-labeled ssDNA with great affinity to GO via π - π interactions,^{49,57} caused quenching of the dye fluorescence.⁸⁰ Subsequent binding of the dye-labeled ssDNA and the target molecule resulted in a conformational change of the dye-labeled DNA, interfering with its interactions with and releasing it from GO, which led to the reappearance of the fluorescence signal. This proof of concept study confirmed the possibility of developing a fluorescence-enhanced GO-based device with sensitive and selective detection for a target molecule.

A similar study used the same quenching effect of GO with hairpin-structured DNA to produce a GO-based molecular beacon (MB) — a single-stranded oligonucleotide hybridization probe to recognize a target analyte with a complimentary probe sequence. This approach demonstrated stronger affinity of DNA for GO and sensitive and selective detection of specific DNA sequences.⁵⁸ Dong et al. fabricated a GO-based platform to detect biomolecules using fluorescence resonance energy transfer (FRET) from quantum dots (QDs) (with a MB) to GO.⁵⁹ The QDs, modified with a MB (MB-QDs), were able to act as probes on GO, thus allowing the recognition of specific DNA sequences. The strong π - π stacking interactions between MB-QDs and GO resulted in quenching of the QDs fluorescence. In the presence of the DNA target, the distance between QDs and GO increased, weakening the GO MB-target interactions and thus significantly decreasing the FRET and increasing the QDs fluorescence intensity, indicating a facile method for target recognition.

Wang et al. described a method for functionalization of GO with polyaniline (PANI) via electrostatic interactions, hydrogen bonding, and π - π stacking interactions.^{60,61} The GO-PANI composites were further optimized via *in situ* polymerization of monomer in the presence of GO, using a mild oxidant, thus

improving the electrochemical performance of the composite as a supercapacitor electrode. The composites had increased initial specific capacitances, improved capacitance retention, and decreased internal resistance, when compared to a PANI electrode alone.

Graphene oxide has also been functionalized with TPE-SO₃Na via π - π stacking to improve the selectivity of biosensors based on aggregation-induced emission (AIE) for detection of bovine serum albumin (BSA).⁶² In AIE biosensors, non-luminescent molecules are induced to emit efficiently by aggregate formation.^{63–65} TPE-SO₃Na is an AIE molecule that can detect bio-macromolecules such as BSA.⁶⁶ The binding of BSA prevents the free rotation of the AIE molecule, making TPE-SO₃Na highly emissive in its presence.⁶⁷ While TPE-SO₃Na is highly sensitive for BSA, it displays no selectivity for BSA, as it responds similarly to many other bio-macromolecules.^{66,67} However, with the addition of GO, the detection of BSA with good sensitivity and selectivity can be achieved.⁷¹ This is because the π - π interactions between the AIE molecule and GO quench fluorescence, but only when the binding effect of AIE molecules and the protein is stronger than the π - π interaction. Since the binding effect of TPE-SO₃Na for BSA is slightly higher than other proteins, selectivity was achieved.

Due to the resulting strength of the π - π interactions, functionalization of graphene surfaces with pyrene (PY) derivatives has also been studied. In 2018, Wang et al. investigated functionalization of thermally reduced GO (trGO) with pyrene derivatives, terminated by the hydrogen bonding unit ureidopyrimidinone (UP) to form (trGO)-UPPY.⁶⁸ The graphene surface was modified with pyrene groups which formed π - π bonds with UPPY (Figure 6). This Layer-by-Layer (LBL) self-assembly technique was repeated to form films of trGO-UPPY that compose both hydrogen bonds and π - π bonds. The resulted multilayer films demonstrated potential as excellent electron conductors to improve electron transfer.

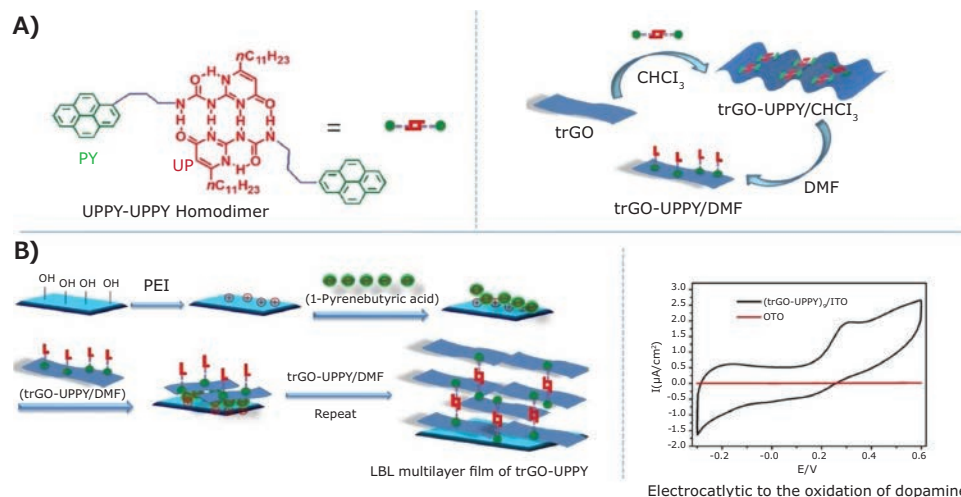


Figure 6. A) Formation of UPPY-UPPY homodimer B) Grafting of UPPY onto trGO through π - π bonding and formation of multilayer trGO-UPPY through LBL assembly technique. Reproduced with permission from the corresponding author.⁶⁸

In another biomedical study, Wahid et al. examined GO as a potential drug carrier through non-covalent functionalization.⁷⁴ Aromatic organic molecules (drugs) that were non-covalently attached to graphene surfaces were more easily released than those bonded covalently. Wahid et al. also reported the successful functionalization of graphene sheets with Ramizol, an antibiotic with antioxidant properties.⁶⁹ Due to its planar geometry, Ramizol can form π - π bonds with graphene surfaces; this interaction has been previously shown to facilitate the exfoliation of graphite into graphene sheets, while stabilizing the sheets in aqueous environments.

Another method for noncovalent functionalization of GO was demonstrated by Liu et al. using a redox reaction.⁷⁰ This spontaneous redox reaction occurs in an aqueous mixture containing GO, FeCl_3 , and $\text{K}_3[\text{Fe}(\text{CN})_6]$, resulting in the formation of Prussian blue (PB) nanocubes on the surface of GO. This GO-PB nanocomposite was cast onto a GC electrode surface, demonstrating great stability, good reproducibility, excellent electrochemical activity, and high sensitivity for electrocatalytic reduction of H_2O_2 . In addition, GO increased the effective surface area of the GC electrode, thus enhancing sensitivity. This GO-PB nanocomposite showed great promise as a potential biofuel cell electrode, as well as a novel electrochemical sensor.

Conclusion

Graphene oxide sheets are carbon-based nanomaterials with hydroxyl, epoxy, carboxyl, and other functional groups attached to their basal planes and edges. Various functionalization methods have been used to enhance their mechanical, electrical, and chemical properties. For functionalization of hydroxyl groups, silanization on GO and rGO with molecules such as MPS can improve both tensile strength and solubility. In addition, esterification with benzene-1,4-diboronic acid can link multiple single layer GO sheets into a 3D porous network. For covalent functionalization of epoxy groups on GO, many methods involve attack on the α -carbon of the epoxide, thus creating nanosheets with high dispersibility in polar solvents and films with enhanced gas barrier properties. For the functionalization of carboxylic groups, some common methods include activation coupled with esterification, which solubilizes GO; other methods include activation coupled with amidation, which facilitates attachment of common biomolecules to GO. The ability to enhance its properties demonstrates the wide range of GO's potential applications, especially in the field of biomedicine, water-insoluble drug delivery, clinical diagnostics, and specific DNA sequence detection. For non-covalent functionalization, π - π stacking and electrostatic interactions enhance the electrical properties of GO, improving the electron transfer process, increasing the specific capacitance, and decreasing the internal resistance. Non-covalent functionalization of GO has improved as an effective and tunable approach for fabricating electrochemical sensors and selective biomolecule detectors. In summary, modified graphene oxide sheets are now being widely applied in the development of devices for use in fields of industrial, environmental, and biomedical research, and their full potential is only beginning to be developed.

References

- (1) Shams, N.; Lim, H. N.; Hajian, R.; Yusof, N. A.; Abdullah, J.; Sulaiman, Y.; Ibrahim, I.; Huang, N. M. *RSC Adv.* **2016**, 6 (92), 89430–89439.
- (2) Singh, R. K.; Kumar, R.; Singh, D. P. *RSC Adv.* **2016**, 6 (69), 64993–65011.
- (3) Geim, A. K.; Novoselov, K. S. *The rise of graphene, Nanoscience and Technology: A Collection of Reviews from Nature Journals*, World Scientific, **2010**, 11–19.
- (4) Park, S.; Ruoff, R. S. *Nat. Nanotechnol.* **2019**, 4 (4), 217.
- (5) Stoller, M. D.; Park, S.; Zhu, Y.; An, J.; Ruoff, R. S. *Nano Lett.* **2008**, 8 (10), 3498–3502.
- (6) Park, H. J.; Meyer, J.; Roth, S.; Skákalová, V. *Carbon* **2010**, 48 (4), 1088–1094.
- (7) Krajewska, A.; Pasternak, I.; Sobon, G.; Sotor, J.; Przewłoka, A.; Ciuk, T.; Sobieski, J.; Grzonka, J.; Abramski, K. M.; Strupinski, W. *Appl. Phys. Lett.* **2017**, 110 (4), 041901.
- (8) Nieto, A.; Lahiri, D.; Agarwal, A. *Carbon* **2012**, 50 (11), 4068–4077.
- (9) Pei, S.; Cheng, H.-M. *Carbon* **2012**, 50 (9), 3210–3228.
- (10) Alam, S. N.; Sharma, N.; Kumar, L. *Graphene* **2017**, 6 (01), 1.
- (11) Compton, O. C.; Nguyen, S. T. *Small* **2010**, 6 (6), 711–723.
- (12) Eda, G.; Chhowalla, M. *Adv. Mater.* **2010**, 22 (22), 2392–2415.
- (13) Kim, F.; Cote, L. J.; Huang, J. *Adv. Mater.* **2010**, 22 (17), 1954–1958.
- (14) Li, X.; Zhang, G.; Bai, X.; Sun, X.; Wang, X.; Wang, E.; Dai, H. *Nat. Nanotechnol.* **2008**, 3 (9), 538.
- (15) Du, X.; Skachko, I.; Barker, A.; Andrei, E. Y. *Nat. Nanotechnol.* **2008**, 3 (8), 491.
- (16) Eda, G.; Mattevi, C.; Yamaguchi, H.; Kim, H.; Chhowalla, M. *J. Phys. Chem. C* **2009**, 113 (35), 15768–15771.
- (17) Gómez-Navarro, C.; Weitz, R. T.; Bittner, A. M.; Scolari, M.; Mews, A.; Burghard, M.; Kern, K. *Nano Lett.* **2007**, 7 (11), 3499–3503.
- (18) Chen, D.; Feng, H.; Li, J. *Chem. Rev.* **2012**, 112 (11), 6027–6053.
- (19) Xu, Y.; Bai, H.; Lu, G.; Li, C.; Shi, G. *J. Am. Chem. Soc.* **2008**, 130 (18), 5856–5857.
- (20) Bekyarova, E.; Itkis, M. E.; Ramesh, P.; Berger, C.; Sprinkle, M.; de Heer, W. A.; Haddon, R. C. *J. Am. Chem. Soc.* **2009**, 131 (4), 1336–1337.
- (21) Matsuo, Y.; Nishino, Y.; Fukutsuka, T.; Sugie, Y. *Carbon* **2007**, 45 (7), 1384–1390.
- (22) Carpio, I. E. M.; Mangadiao, J. D.; Nguyen, H. N.; Advincula, R. C.; Rodrigues, D. F. *Carbon* **2014**, 77, 289–301.
- (23) Mauter, M. S.; Elimelech, M. *Environ. Sci. Technol.* **2008**, 42 (16), 5843–5859.
- (24) Wiesner, M.; Bottero, J. -Y. *Environmental Nanotechnology*, McGraw-Hill Professional Publishing **2007**.
- (25) Akhavan, O.; Ghaderi, E. *Surf. Coat. Technol.* **2010**, 205 (1), 219–223.
- (26) Akhavan, O. *ACS Nano* **2010**, 4 (7), 4174–4180.
- (27) Su, D. S.; Perathoner, S.; Centi, G. *Chem. Rev.* **2012**, 113 (8), 5782–5816.
- (28) Knetsch, M. L.; Koole, L. H. *Polymers* **2011**, 3 (1), 340–366.
- (29) Hou, S.; Kasner, M. L.; Su, S.; Patel, K.; Cuellari, R. *J. Phys. Chem. C* **2010**, 114 (35), 14915–14921.
- (30) Hu, X.; Su, E.; Zhu, B.; Jia, J.; Yao, P.; Bai, Y. *Compos. Sci. Technol.* **2014**, 97, 6–11.
- (31) Gao, W. *Graphene oxide: Reduction recipes, spectroscopy, and applications*, Springer **2015**.
- (32) Yuan, M.; Chen, Y.; Yuan, M.; Li, H.; Xia, X.; Xiong, C. *Polymers* **2018**, 10 (2), 177.
- (33) Burruss, J. W.; Gadipelli, S.; Ford, J.; Simmons, J. M.; Zhou, W.; Yildirim, T. *Angew. Chem. Int. Ed.* **2010**, 49 (47), 8902–8904.
- (34) Wang, S.; Chia, P. J.; Chua, L. L.; Zhao, L. H.; Png, R. Q.; Sivaramakrishnan, S.; Zhou, M.; Goh, R. G. S.; Friend, R. H.; Wee, A. T. S. *Advanced Materials* **2008**, 20 (18), 3440–3446.
- (35) Yang, H.; Shan, C.; Li, F.; Han, D.; Zhang, Q.; Niu, L. *Chem. Commun.* **2009**, 26, 3880–3882.
- (36) Bandyopadhyay, P.; Park, W. B.; Layek, R. K.; Uddin, M. E.; Kim, N. H.; Kim, H. -G.; Lee, J. H. *J. Membrane Sci.* **2016**, 500, 106–114.
- (37) Yang, H.; Li, F.; Shan, C.; Han, D.; Zhang, Q.; Niu, L.; Ivaska, A. *J. Mater. Chem.* **2009**, 19 (26), 4632–4638.
- (38) Niyogi, S.; Hamon, M.; Hu, H.; Zhao, B.; Bhowmik, P.; Sen, R.; Itkis, M.; Haddon, R. *Acc. Chem. Res.* **2002**, 35 (12), 1105–1113.
- (39) Zhang, X.; Huang, Y.; Wang, Y.; Ma, Y.; Liu, Z.; Chen, Y. *Carbon* **2009**, 47 (1), 334–337.
- (40) Liu, J.; Xue, Y.; Dai, L. *J. Phys. Chem. Lett.* **2012**, 3 (14), 1928–1933.
- (41) Liu, Z. -B.; Xu, Y. -F.; Zhang, X. -Y.; Zhang, X. -L.; Chen, Y. -S.; Tian, J. -G. *J. Phys. Chem. B* **2009**, 113 (29), 9681–9686.
- (42) Niyogi, S.; Bekyarova, E.; Itkis, M. E.; McWilliams, J. L.; Hamon, M. A.; Haddon, R. C. *J. Am. Chem. Soc.* **2006**, 128 (24), 7720–7721.
- (43) Liu, F.; Choi, J. Y.; Seo, T. S. *Biosens. Bioelectron.* **2010**, 25 (10), 2361–2365.
- (44) Xu, Y.; Liu, Z.; Zhang, X.; Wang, Y.; Tian, J.; Huang, Y.; Ma, Y.; Zhang, X.; Chen, Y. *Adv. Mater.* **2009**, 21 (12), 1275–1279.
- (45) Su, P. -G.; Lu, Z. -M. *Sens. Actuators B Chem.* **2015**, 211, 157–163.
- (46) Liu, J.; Durstock, M.; Dai, L. *Energy Environ. Sci.* **2014**, 7 (4), 1297–1306.
- (47) Shen, J.; Shi, M.; Yan, B.; Ma, H.; Li, N.; Hu, Y.; Ye, M. *Colloids Surf. B* **2010**, 81 (2), 434–438.

- (48) Yagati, A.K.; Min, J.; Cho, S. *J. Electrochem. Soc.* **2014**, *161* (14), G133–G140.
- (49) Liu, Z.; Robinson, J. T.; Sun, X.; Dai, H. *J. Am. Chem. Soc.* **2008**, *130* (33), 10876–10877.
- (50) Mohanty, N.; Berry, V. *Nano Lett.* **2008**, *8* (12), 4469–4476.
- (51) Zhang, X.; Liu, Z.; Huang, Y.; Wan, X.; Tian, J.; Ma, Y.; Chen, Y. *J. Nanosci. Nanotechnol.* **2009**, *9* (10), 5752–5756.
- (52) Wakata, K.; Karim, M. R.; Islam, M.S.; Ohtani, R.; Nakamura, M.; Koinuma, M.; Hayami, S. *Chem. Asian J.* **2017**, *12* (2), 194–197.
- (53) Liu, Y.; Yu, D.; Zeng, C.; Miao, Z.; Dai, L. *Langmuir* **2010**, *26* (9), 6158–6160.
- (54) Hatakeyama, K.; Karim, M. R.; Ogata, C.; Tateishi, H.; Taniguchi, T.; Koinuma, M.; Hayami, S.; Matsumoto, Y. *Chem. Commun.* **2014**, *50* (93), 14527–14530.
- (55) Su, Q.; Pang, S.; Alijani, V.; Li, C.; Feng, X.; Müllen, K. *Adv. Mater.* **2009**, *21* (31), 3191–3195.
- (56) Lu, C. H.; Yang, H. H.; Zhu, C. L.; Chen, X.; Chen, G. N. *Angew. Chem. Int. Ed.* **2009**, *121* (26), 4879–4881.
- (57) Varghese, N.; Mogera, U.; Govindaraj, A.; Das, A.; Maiti, P. K.; Sood, A. K.; Rao, C. *Chem. Phys. Chem.* **2009**, *10* (1), 206–210.
- (58) Li, F.; Huang, Y.; Yang, Q.; Zhong, Z.; Li, D.; Wang, L.; Song, S.; Fan, C. *Nanoscale* **2010**, *2* (6), 1021–1026.
- (59) Dong, H.; Gao, W.; Yan, F.; Ji, H.; Ju, H. *Anal. Chem.* **2010**, *82* (13), 5511–5517.
- (60) Wang, H.; Hao, Q.; Yang, X.; Lu, L.; Wang, X. *ACS Appl. Mater. Interfaces* **2010**, *2* (3), 821–828.
- (61) Wang, H.; Hao, Q.; Yang, X.; Lu, L.; Wang, X. *Electrochem. Commun.* **2009**, *11* (6), 1158–1161.
- (62) Xu, X.; Huang, J.; Li, J.; Yan, J.; Qin, J.; Li, Z. *Chem. Commun.* **2001**, *47* (45), 12385–12387.
- (63) Liu, Y.; Tang, Y.; Barashkov, N. N.; Irgibaeva, I. S.; Lam, J. W.; Hu, R.; Birimzhanova, D.; Yu, Y.; Tang, B. Z. *J. Am. Chem. Soc.* **2010**, *132* (40), 13951–13953.
- (64) Hong, Y.; Lam, J. W.; Tang, B. Z. *Chem. Commun.* **2009**, *29*, 4332–4353.
- (65) Li, Z.; Dong, Y.; Mi, B.; Tang, Y.; Häussler, M.; Tong, H.; Dong, Y.; Lam, J. W.; Ren, Y.; Sung, H. H. *J. Phys. Chem. B* **2005**, *109* (20), 10061–10066.
- (66) Li, Z.; Dong, Y.Q.; Lam, J. W.; Sun, J.; Qin, A.; Häußler, M.; Dong, Y. P.; Sung, H. H.; Williams, I. D.; Kwok, H. S. *Adv. Funct. Mater.* **2009**, *19* (6), 905–917.
- (67) Tong, H.; Hong, Y.; Dong, Y.; Häussler, M.; Li, Z.; Lam, J. W.; Dong, Y.; Sung, H. H. -Y.; Williams, I. D.; Tang, B. Z. *J. Phys. Chem. B* **2007**, *111* (40), 11817–11823.
- (68) Wang, S.; Yang, L.; Wang, Q.; Fan, Y.; Shang, J.; Qiu, S.; Li, J.; Zhang, W.; Wu, X. *J. Photochem. Photobiol. A* **2018**, *355*, 249–255.
- (69) Wahid, M. H.; Stroehrer, U. H.; Eroglu, E.; Chen, X.; Vimalanathan, K.; Raston, C. L.; Boulos, R. A. *J. Colloid Interface Sci.* **2015**, *443*, 88–96.
- (70) Liu, X. -W.; Yao, Z. -J.; Wang, Y. -F.; Wei, X. -W. *Colloids Surf. B* **2010**, *81* (2), 508–512.
- (71) Xu, X.; Huang, J.; Li, J.; Yan, J.; Qin, J.; Li, Z. *Chem. Commun.* **2011**, *47*, 12385–12387.

Graphene Oxide

Name	Form	Description	Cat. No.
Graphene oxide	dispersion in H ₂ O	2 mg/mL	763705-25ML 763705-100ML
	dispersion in H ₂ O	4 mg/mL, dispersibility: Polar solvents monolayer content (measured in 0.5mg/mL): >95%	777676-50ML 777676-200ML
	paste	non-exfoliated	900704-100G 900704-25G
	dispersion in 0.05 M HEPES buffer	1 mg/mL, pH stabilized	901940-25ML 901940-100ML
	powder or flakes	sheets	763713-250MG 763713-1G
	dispersion in H ₂ O	1 mg/mL, 15–20 sheets, 4–10% edge-oxidized	794341-50ML 794341-200ML
Graphene oxide nanocolloids	dispersion in H ₂ O	2 mg/mL	795534-50ML 795534-200ML

Functionalized Graphene Oxide

Name	Form	Description	Cat. No.
Graphene oxide, alkylamine functionalized	dispersion in toluene	<0.5 % (w/w) 2.0 mg/mL	809055-50ML
Graphene oxide, ammonia functionalized	dispersion in H ₂ O	1 mg/mL	791520-25ML 791520-100ML

Reduced Graphene Oxide

Description	Composition	Conductivity	Cat. No.
Chemically reduced	Carbon >75 wt. % Oxygen <22% Nitrogen >5 wt. %	>600 S/m	777684-250MG 777684-500MG
Chemically reduced by hydrazine	Carbon >75% Nitrogen <5%	7111 S/m (pressed pellet)	805424-500MG 805424-1G
Stabilized with poly(sodium 4-styrenesulfonate)	—	—	900197-100ML

Functionalized Reduced Graphene Oxide

Name	Description	Composition	Cat. No.
Fe ₃ O ₄ /reduced graphene oxide nanocomposite	Loading Density: 30%–70% (Fe ₃ O ₄ nanocrystal) by TEM Resistance: <10 ³ Ω/sq (reduced graphene oxide) dispersion in acetone	reduced graphene oxide 10–17% Fe ₃ O ₄ nanocrystal 3–8% acetone ~80%	803804-5ML
Mn ₃ O ₄ /reduced graphene oxide nanocomposite	10 mg/mL Loading Density: 30%–70% (Mn ₃ O ₄ nanocrystal) by TEM Resistance: <10 ³ Ω/sq (reduced graphene oxide) dispersion in acetone	acetone ~80% reduced graphene oxide 10–17% Mn ₃ O ₄ nanocrystal 3–8%	803812-5ML
Pd/reduced graphene oxide nanocomposite	Loading Density: 10%–50% (Pd nanocrystal) by TEM Resistance: <10 ³ Ω/sq (graphene) dispersion in acetone	Pd nanocrystal <5% acetone ~80% reduced graphene oxide 5–20%	803790-5ML
PtCo/reduced graphene oxide nanocomposite	Loading Density: 10%–50% (PtCo nanocrystal) by TEM Resistance: <10 ³ Ω/sq (graphene) dispersion in acetone	acetone ~80% reduced graphene oxide 10–18% PtCo nanocrystal 2–10%	803901-5ML
PtPd/reduced graphene oxide nanocomposite	10 mg/mL Loading Density: 10–50% (PtPd nanocrystal) by TEM Resistance: <10 ³ Ω/sq (reduced graphene oxide) dispersion in acetone	acetone ~80% PtPd nanocrystal 2–10% reduced graphene oxide 10–18%	803820-5ML
Pt/reduced graphene oxide nanocomposite	10 mg/mL Loading Density: 5%–30% (Pt nanocrystal) by TEM Resistance: <10 ³ Ω/sq (graphene) dispersion in acetone	acetone ~80 wt. % reduced graphene oxide 5–20% Pt nanocrystal <5%	803782-5ML
Reduced graphene oxide	amine functionalized	Carbon >65 wt. % Nitrogen >5 wt. %	805432-500MG
	octadecylamine functionalized	Carbon >78 wt. % Nitrogen >3 wt. %	805084-500MG
TiO ₂ /reduced graphene oxide nanocomposite	Loading Density: 30%–70% (TiO ₂ nanocrystal) by TEM	—	805343-5ML

GRAPHENE SYNTHESIS MADE GREENER WITH CYRENE™

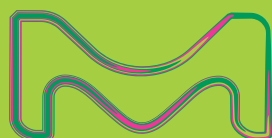
Cyrene™, our new Greener Solvent Alternative offers the following advantages over NMP for Graphene Synthesis:

Superior Performance: Graphene dispersions in Cyrene™ are 10x more concentrated; resulting flakes are larger & less defective

More Sustainable: Dipolar aprotic Cyrene™ is produced in only two steps from renewable cellulose

Safer: An Ames miniscreen of Cyrene™ revealed no mutagenic activity – Cyrene is not restricted for use

DOI 10.1039/C7GC00112F



The life science business of Merck operates as MilliporeSigma in the U.S. and Canada.

© 2019 Merck KGaA, Darmstadt, Germany and/or its affiliates. All Rights Reserved. Merck and the Vitamin M are trademarks of Merck KGaA, Darmstadt, Germany or its affiliates. All other trademarks are the property of their respective owners. Detailed information on trademarks is available via publicly accessible resources.

MERCK

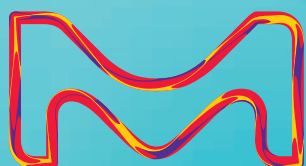


Merck KGaA
Frankfurter Strasse 250
64293 Darmstadt, Germany

MERCK

THE MASTERS OF MATERIALS

Expertise at the nanoscale
SigmaAldrich.com/nanomaterials



© 2019 Merck KGaA, Darmstadt, Germany and/or its affiliates. All Rights Reserved. Merck and the vibrant M are trademarks of Merck KGaA, Darmstadt, Germany or its affiliates. All other trademarks are the property of their respective owners. Detailed information on trademarks is available via publicly accessible resources.

Lit. No. MK_BR2991EN 2019-19316 04/2019

The life science
business of Merck
operates as
MilliporeSigma in the
U.S. and Canada.

Sigma-Aldrich®
Lab & Production Materials